Additive Manufacturing of Polymer-based Microfluidic Devices

Vahid Karamzadeh

A Thesis
in
The Department
of
Mechanical and Industrial Engineering

Presented in Partial Fulfillment of the Requirements
for the Degree of Masters of Applied Science (Mechanical Engineering) at
Concordia University
Montreal, Quebec, Canada

July 2018

CONCORDIA UNIVERSITY
School of Graduate Studies

This is to certify that the thesis prepared,

By: **Vahid Karamzadeh**

Entitled: **“Additive Manufacturing of Polymer-based Microfluidic Devices”**

and submitted in partial fulfillment of the requirements for the degree of

Masters of Applied Science (Mechanical Engineering)

complies with the regulations of the University and meets the accepted standards with respect to originality and quality.

Signed by the final examining committee:

Dr. Alex DeVisscher Chair

Dr. Rama Bhat Examiner

Dr. Lucia Tirca Examiner

Dr. Muthukumaran Packirisamy Supervisor

Approved by ____
Dr. Mamoum Medraj, MASc Program Director
Chair of Department or Graduate Program Director

____
Dr. Amir Asif, Dean
Faculty of Engineering & Computer Science

Date: ______________

ABSTRACT

Vahid Karamzadeh

Additive Manufacturing of Polymer-based Microfluidic devices

Microfluidics is a multidisciplinary area comprising several disciplines such as biology, chemistry and tissue engineering, which leads to manipulation and analysis of liquid through micro channels. Microfluidic devices provide numerous advantages for economical point-of-care diagnosis compared to conventional testing devices. In addition, more recently organ-on-a-chip which is a 3D microfluidic network for cell culturing has offered a microfluidic chip that stimulates the response of an organ system which can significantly reduce the costs of developing new pharmaceutical drugs. In spite of multiple advantages of microfluidic devices, barriers exist in current microfabrication methods. Fabrication of microfluidic molds requires cleanroom facilities and is a costly and tedious process which hindered the commercialization of microfluidic chips. Although, using 3D printed molds has been suggested to simplify fabrication of chips, their resolution is limited to 100 μm. In addition to these factors, molding process is challenging to fully automate which means that it is in contrast to the vision of cost-effective and mass production of these devices. Therefore, a fully automated, rapid process is required to guide microfluidics towards the development of low-cost more commercially devices.

In this thesis, different additive manufacturing methods for fabrication of polymeric microfluidic devices are presented. First, a commercial stereolithography (SLA) 3D printer was used to fabricate 3D printed molds. Limitations and accuracy of using 3D printed templates for microfluidic applications were investigated. Then, the thesis presents a promising additive manufacturing method toward printing a polymer-based device by using an acoustic assisted printing method. This method can significantly simplify and improve fabrication of microfluidic devices. Simulation of the acoustic wave and the heat induced by that were obtained in order to optimize the printing process prior to the experiment. The model provided a good understanding and estimation of acoustic field, temperature rise and focal region size. Time and cost required for fabricating a part by this method is considerably low and no additional post processing is required to turn the printed part to a functional part. The proposed method was finally applied to fabricate

a fluidic channel. A fluidic channel can be printed in less than 10 minutes without adding additional components.

Acknowledgements

First of all, I would like to convey my sincere gratitude to my advisor Professor Muthukumaran Packirisamy for the continuous support for my master study and research, for his wisdom, motivation, patience and immense guidance. I am greatly thankful to Prof. Packirisamy for accepting me in Optical-Bio Microsystems group as well as supporting and mentoring me how to apply my theoretical knowledge to practical solving throughout the completion of this thesis.

This thesis would not have been possible without the outstanding support of Dr. Mohsen Habibi. My very sincere thanks for his guidance and contributions in all aspects of the research. I must also express my appreciation to Shervin Foroughi for his great collaboration in fabrication and developing ideas and for his tremendous discussion and supports.

It has been a pleasure to be a member of the Optical-Bio Microsystems laboratory, and I am very thankful to the members of the lab for their help and assistance in handling the lab affairs during my master program. Many thanks to Simona Badilescu, Ahmad Sohrabi Kashani, Mahdi Derayatifar and Durai Chelvan for helping me at different stages of the thesis. I am also thankful to all the support staff at Concordia University.

I am indebted to my great mentor and friend Dr. Nima Khadem Mohtaram who has been always supportive in dedicating and guiding my graduate studies.

Above all, my deepest heartfelt appreciation goes out to my love, Ghazaaleh, my mother, Maryam, my father, Mr. Saeed Karamzadeh and my sister and brother. Words simply cannot express my gratitude for their love and encouragement. They have been with me every single step from the beginning to the end and definitely, I could not have achieved it without them. They provided the best possible network of love and support and help and kindness.

Contents

List of Figures ix

List of Tables xii

Nomenclature xii

Chapter 1: Introduction and literature review **1**
- 1.1. Problem statement 1
  - 1.1.1. Microfluidics 1
  - 1.1.2. Traditional fabrication methods for Microfluidics 2
  - 1.1.3. Additive manufacturing 3
  - 1.1.4. Additive manufacturing and microfluidics 5
- 1.2. Objective of the thesis 11
  - 1.2.1. Ultrasound transducers 12
  - 1.2.2. HIFU transducers 13
- 1.3. Contributions 13

Chapter 2: Types of additive manufacturing methods **15**
- 2.1. Additive manufacturing methods classification 15
- 2.2. Additive manufacturing technologies 16
  - 2.2.1. Stereolithography (SLA) 16
  - 2.2.2. Fused Deposition Modeling (FDM) 17
  - 2.2.3. Photopolymer jetting 17
  - 2.2.4. Material jetting 17
  - 2.2.5. Binder jetting 17
  - 2.2.6. Laser melting 18
  - 2.2.7. Laser sintering 18
  - 2.2.8. Electron beam melting 19
- 2.3. 3D-printed microfluidic fabrication methods 19
  - 2.3.1. Fabrication of mold for Polymer-based microfluidic devices 19
  - 2.3.2. Single step fabrication of a microfluidic device 20

Chapter 3: Simulation **23**
- 3.1. Introduction 23

3.2. Geometry 24
3.2.1. Channel geometry 24
3.2.2. Model geometry 24
3.3. Acoustic field theory 25
3.3.1. Ultrasound Equation 25
3.4. Heat transfer field 27
3.5. Ultrasound and heat transfer mesh 29
3.6. Results 30
3.6.1. Acoustic and thermal fields at the frequency of 2.15 MHz and the power of 218 W 30
3.6.2. Effect of frequency on pressure and thermal fields 32
3.6.3. Effect of power on pressure and thermal fields 36
3.6.4. Effect of the divider material on the pressure field 37
3.6.5. Effect of resin material on acoustic and thermal fields 39
3.7. Conclusions 42
Chapter 4: 3D printed molds for non-planar PDMS microfluidic channels 44
4.1. Introduction 44
4.2. Experiment and measurement 44
4.2.1. 3D printing of the mold 44
4.2.2. Post-processing of 3D printed molds 45
4.2.3. Fabrication of microfluidic devices 45
4.2.4. Characterization of surface topography 45
4.3. Results and discussion 45
4.3.1. 3D microfluidic channel 48
4.3.2. Droplet generation device 50
4.3.3. Suspended polymeric microfluidic device 53
4.4. Conclusions 55
Chapter 5: Experimental setup and methodology 57
5.1. Experimental setup 57
5.1.1. HIFU system 58
5.1.2. Positioning device 59
5.1.3. Data Acquisition System 60
5.1.4. Water container 60
5.1.5. Resin container 60

5.1.6. Thermochromic liquid crystal sheet 62
5.2. Methodology 62
5.2.1. CNC post processor 62
5.2.2. HIFU thermal field characterization 65
Chapter 6: Material selection 66
6.1. Thermosetting polymers 66
6.2. Influence of time, temperature, and mass on the curing process 67
6.3. High and low exothermic resins 68
6.4. Experiment materials 68
Chapter 7: Results and discussion 71
7.1. Acoustic Streaming 71
7.2. Simulation verification 73
7.2.1. Acoustic field 73
7.2.2. Temperature rise 74
7.3. Characterization of focal shape using a thermochromic liquid crystal sheet 75
7.4. Fabricated channels by acoustic-assisted printing 75
7.5. Mold fabrication on acrylic plates by a high intensity focused transducer 78
7.6. Conclusions 81
Chapter 8: Conclusions and future work 82
8.1. Summary and conclusion 82
8.2. Future works 83
References 85

List of Figures

Figure 1-1 Publication trends. Blue bar-graph provides number of publications in the field of microfluidics in 2011-2015; orange bar-graph presents number of publications with keywords of “3D-printing” and “microfluidic” [1] 6
Figure 1-2 Comparison of conventional and 3D printing methods for microfluidic chip fabrication; process selection and design criteria are also illustrated for the 3D printing method 7
Figure 1-3 Automation and resolution trade-off in transition from conventional microfabrication methods to 3D printing [27] 8
Figure 1-4 3D printed parts with PDMS; (a) by adding a photoinitiator to PDMS [43]; (b) by adding a SE 1700 elastomer to PDMS [44]; (c) by using a support bath to 3D print PDMS [42]; (d) transparent part by adding a photoinitiator [45] 10
Figure 2-1 Additive manufacturing process classification based on the state of the material 16
Figure 2-2 Various 3D printing methods for microfluidics. (a) Fused deposition modeling; (b) Selective laser sintering; (c) Photopolymer jetting; (d) Material jetting. Images courtesy of custompartnet.com..... 18
Figure 2-3 PDMS-based microfluidic devices fabricated by 3D printed molds. (a) 100 µm deep chaotic mixer [41]; (b) a 3D printed mold for autonomous microfluidic capillaric circuit [78] 20
Figure 2-4 Direct printed microfluidic devices; (a) and (b) 45 microfluidic valves fabricated in a single step [87]; (c) and (d) a transparent microfluidic device fabricated with a PDMS-based resin [45] 22
Figure 3-1 Leading parameters in the printing process 23
Figure 3-2 Model geometry 24
Figure 3-3 Focal zone is depicted 26
Figure 3-4 Acoustic field in presence of water. (a) pressure field; (b) intensity field 30
Figure 3-5 (a) acoustic pressure amplitude profile along the z-axis; (b) acoustic pressure amplitude profile along the radial direction in the focal point; 31
Figure 3-6 Thermal field in presence of water. (a) Contour plot of the temperature rise after 1 second of insonation; (b) heating and cooling curves at acoustic focus and 0.5 mm off-axis in the focal plane; 32
Figure 3-7 Normalized temperature and intensity profile 32
Figure 3-8 (a) intensity profile along the z-axis for different frequencies; (b) intensity as a function of frequency 33
Figure 3-9 Focal length (a) and focal width (b) as a function of frequency 34
Figure 3-10 Temperature rise at the focus as a function of frequency 35
Figure 3-11 Surface plot of the temperature rise in presence of water after 1 second of insonation for frequencies of: (a) 0.4 MHz; (b) 1 MHz; (c) 2 MHz; (d) 3 MHz. 35
Figure 3-12 Maximum intensity at the focus point for various powers 36
Figure 3-13 Temperature rise after 1s of sonication for different input powers 37
Figure 3-14 Acoustic field in presence of water and the divider. Intensity profile: (a) different divider materials; (b) polystyrene dividers with various thicknesses 38
Figure 3-15 Acoustic field in presence of water and the divider. (a) different acoustic impedances; (b) maximum intensity versus acoustic impedance. 39
Figure 3-16 Acoustic intensity profile along the z-axis for different attenuations 40
Figure 3-17 Temperature rise in the focus point as a function of absorption coefficient 41

Figure 3-18 Surface plot of temperature rise in the petri dish for various attenuations in the petri dish...42
Figure 4-1 Printing on the build platform; printing layer are illustrated by black and white strips;..........46
Figure 4-2 Surface comparison of two models; model printed vertically; (a) flexible resin (b) clear resin; model printed directly on the platform; (c) flexible resin (d) clear resin. 47
Figure 4-3 Rapid prototyping PDMS-based microfluidic device by 3D printed mold. (a) Design of a microfluidic channel (b) The reusable mold for fabrication of PDMS-based microfluidic device fabricated by clear resin. 3D printed molds by clear resin (c), flexible resin (d) and FDM filament (e). (f) Picture of the fabricated microfluidic device is depicted. 48
Figure 4-4 Laser scanning microscopic images of 3D printed molds in flexible resin (left) and clear resin (right) .3D scanning of the 3D printed mold by flexible resin (a) and clear resin (b). (c&e) The height profile of the channel by line scanning microscopy. The blue line shows the height of the channel in the 2D scanned image and the red line shows the height of the channel in presence of a rod in the red line in the 2D scanned image. (d) and (f) present the surface of the mold. (g) and (h) show the height and the profile of the rod. 49
Figure 4-5 Comparison of the designed model and the printed mold with different resins. The yellow bar represents the design dimensions. 50
Figure 4-6 Droplet generation device. (a) laser scanning microscopic image; the 3D printer was not able to construct the bat-wing (b) generated droplet in the T junction; (c) Experiment setup consists of two syringe pumps and an optical microscope; (d) microfluidic chip design..51
Figure 4-7 Obstacle; considerable error compared to the design..51
Figure 4-8 Comparison of models printed on the build platform and with supports with the design........52
Figure 4-9 Suspended polymeric microfluidic device. (a) Laser scanning microscopic image and profile of channels; (b) microfluidic chip design; (c) molds and the fabricated mold 54
Figure 4-10 Comparison between the model and the design 55
Figure 5-1 Block diagram of the experimental setup..57
Figure 5-2 Assembled CNC machine 59
Figure 5-3 3D printing setup; the CAD model was designed using SolidWorks.......................................61
Figure 5-4 Refraction of the acoustic beam in the resin container..63
Figure 5-5 Machine’s reference position 64
Figure 5-6 Temperature measurement setup...65
Figure 6-1 Schematic diagram of the cross-linking steps; (a) unreacted monomers; (b) linear branching and growth; (c) the gel point; (d) the cured, crosslinked polymer with some unreacted groups [119].......66
Figure 6-2 (a) Viscosity versus time at constant temperature. (b) Effect of ambient temperature on the gel time [118]..67
Figure 6-3 Deformation of the EPON 828 container 69
Figure 7-1 Setup for observing the acoustic streaming...71
Figure 7-2 Acoustic streaming in the focal region, the transducer is placed on the left; (a) power is off and flow is not injected; (b) power is on; (c) turning off the power; (d) power is off 72
Figure 7-3 Acoustic pressure field obtained by the simulation at a power of 400W and a frequency of 2 MHz 73
Figure 7-4 Measured temperature profile with a thermocouple and the simulated profile in water..........74
Figure 7-5 Visible light spot at the focus; Transducer is radiating from the left 75
Figure 7-6 First model; (a) design of the model (b) printing paths generated by a CAM software...........76
Figure 7-7 First model with a channel; (a) printed model; (b) fabricated chip covered with a layer of PDMS during testing with dyed water...76

Figure 7-8 Second model; (a) design of the model; (b) printing path generated by considering a spot size of 1 mm. 77

Figure 7-9 Second printed model with a smaller channel; (a) printed model; (b) fabricated chip bonded with a glass slide during testing with dyed water 78

Figure 7-10 Mold fabrication by a HIFU transducer. (a) designed model (b) Fabricated acrylic molds at a duty cycle of 60 % and with various feed rates; the second model from the left was chosen for mold fabrication. 79

Figure 7-11 Surface topography of the sample printed at DC of 60 % and feed rate of 150 mm/min obtained by confocal microscopy. 80

Figure 7-12 fabrication of a microfluidic device by an acrylic mold. (a) the PDMS chip; holes were punched to connect tubes; (b) the fabricated chip was tested with dyed water. 80

List of Tables

Table 3-1 Material properties 29
Table 4-1 Comparison of printing cost and time for different resins 46
Table 5-1 HIFU transducer parameters 58
Table 5-2 Comparison between different parameters for dividers 61
Table 6-1 Selected polymers 68
Table 6-2 Properties of thermoset polymers 70

Nomenclature

3D	3 dimensional
PDMS	Polydimethylsiloxane
SLA	Stereolithography
FDM	Fused Deposition Modeling

Chapter 1

1. Introduction and literature review

1.1. Problem statement

Microfluidics is a multidisciplinary area comprising several disciplines such as biology, chemistry and engineering, which leads to manipulation and analysis of fluids through micro channels. Microfluidic devices provide several benefits for economical point-of-care diagnosis compared to conventional testing devices. In addition, more recently organ-on-a-chip has offered a microfluidic chip that stimulates the response of an organ system which lead to a significant reduction in the costs of developing new pharmaceutical drugs. In spite of the multiple advantages of microfluidic devices, barriers exist in current microfabrication methods.

Fabrication of molds for polymer-based microfluidic devices requires cleanroom facilities and is a costly and tedious process which hindered the commercialization of chips. Although using 3D printed molds has been suggested to simplify fabrication of microfluidic chips, their resolution is limited to 100 μm. In addition to these factors, molding process is difficult to fully automate which means that it is in contrast to the vision of cost-effective and mass production of these devices [1]. Moreover, direct printing of microfluidic devices is difficult due to their low resolutions. Therefore, a fully automated, rapid process is required to guide microfluidics towards the development of low-cost, more commercially devices [2].

1.1.1. Microfluidics

Microfluidics is a multidisciplinary area coupling several disciplines such as biology, chemistry and tissue engineering, which lead to manipulation and analysis of fluidics through micro channels. The first microfluidic chip was a gas chromatographic air sensor constructed on a silicon wafer in 1979 [3]. Thirteen years later, Harrison et al. developed a microfluidic device for particle separation based on electrophoresis [4]. However, these chips were fabricated using costly and time-consuming methods to selectively etch rigid substrates such as glass and silicon wafer. A significant development in the fabrication of microfluidic devices established by Whiteside's group by using poly(dimethylsiloxane) (PDMS) in a microfluidic system [5]. Since fabrication of microfluidic devices with PDMS was much accessible, it has rapidly become the most commonly used material for fabrication of these devices. In the next section, limitations of conventional methods will be discussed.

1.1.2. Traditional fabrication methods for Microfluidics

PDMS, glass, and silicone have been widely used to fabricate microfluidic channels. However, micromachining method differs for each material [6].

Bulk micromachining is the earliest MEMS technology and is based on using chemical etchant to selectively pattern the substrate [7]. In contrast to this method, *surface micromachining* methods construct structures, by deposition, patterning, and etching multiple layers over a substrate [8].

Micromachining methods have remained to develop, and a number of researchers have fabricated microfluidic devices by taking advantages of surface micromachining [9]–[12]. However, these methods were widely used to construct 2.5D channels due to their limitations. For example, bulk micromachining requires accurate control of channel's aspect ratio because of etch-rate deviations. In addition, surface micromachining is limited to the availability of suitable etchants for sacrificial layers that do not damage the substrate or other layers [8].

Over the past decade, researchers have shown an increased interest in using polymers as an alternative to hard substrates mostly due to their biocompatibility and lower production costs. Therefore, several methods for polymer-based fabrication have been proposed. These methods may be classified into two types of direct micromachining and replication.

Direct micromachining methods such as laser micromachining are a more developed methods for construction of 3D channels. Direct micromachining technologies are based on focusing a laser beam onto the polymer to evaporate the polymer and obtain a void in it.

Replication micromachining methods including *hot embossing*, *injection molding*, and *soft lithography* consist of multiple steps to obtain a mold for polymers.

Soft lithography is a range of microfabrication methods for fabrication or replication structures using patterned elastomer, usually PDMS. This method has several advantages compared to photolithographic etching methods in terms of material cost, production time and reaction conditions. Since its beginning, soft lithography has rapidly become a dominant method in the field of microfluidics. However, this method is not capable of fabrication of microchannels with high aspect ratios and 3D structures [13].

Other methods such as Lithography Galvanoforming Abforming (LIGA), electroplating, micromilling, and microextrusion have also been applied to fabricate microfluidic channels [14]–[17]. However, these methods mostly require expensive machinery and materials.

Together, conventional microfabrication techniques tend to be complex, time-consuming, labor-intensive, manual and require cleanroom facilities which lead to limited growth on the field of microfluidics. In addition, these methods are mostly restricted to Planner channel in which the aspect ratio through the channel is uniform and causes improper microenvironment and cell-to-cell interactions and consequently induce ineffective drug delivery in microfluidic systems [2]. Therefore, traditional fabrication methods have hindered the development of commercial microfluidic devices and a cost-effective automated method is required to benefit and expand this field.

1.1.3. Additive manufacturing

The first method for creating a three-dimensional part using computer-aided design (CAD) was developed in the 1980's in order to create and fast prototype parts. This layer by layer method was developed to assist engineers and designers to rapidly visualize their models [18].

Additive manufacturing first appeared in 1987 by 3D Systems. They invented stereolithography (SL) method in which thin layers selectively solidifies ultraviolet (UV) photo-sensitive liquid resin using a laser. In 1991, several additive manufacturing methods were commercialized, including solid ground curing (SGC) from Cubital, laminated object manufacturing (LOM) from Helisys, and fused deposition modeling (FDM) from Stratasys. In 2015, revolutionary ultra-fast 3D printing machine was introduced by Carbon 3D. Their 3D printer is 100 times faster than currently commercial 3D printing machines.

SGC used photo-sensitive liquid resin, curing layers in one step by exposing UV light through masks fabricated by electrostatic toner on a glass slide. LOM glued and cut paper, plastic, or metal laminates using a digitally guided laser. FDM deposits thermoplastic materials through a hot extruder to manufacture parts layer by layer [19]. In 2009, Fused Deposition Modeling (FDM) printing process patents expired which led to establishing many low-cost 3D printers.

The term “3D Printing” is growingly used as a synonym for AM. This term was primitively the name of rapid prototyping technology invented by MIT. However, Additive Manufacturing is the professional definition of the method that is clearly different from conventional methods of production such as material removal and molding [18].

There are many advantages for additive manufacturing including fast prototyping, single step cost-effective manufacturing and less labor cost. Additive manufacturing enabled to produce parts rapidly compared to traditional manufacturing methods. Complicated designs can be produced from CAD software and printed in few hours. The benefit of this is the rapid development and verification of design ideas, especially in research and development departments. Although industrial additive manufacturing machines take a longer time to construct and post-treat a part, the capability to manufacture functional end parts for mass customization allows huge time-saving benefits when compared to conventional manufacturing techniques.

How to manufacture a part as efficiently as possible is a significant concern for a designer. A number of manufacturing steps are required to produce a part by traditional methods. These steps affect the quality of the design. In addition, it often happens that the designer needs to alter the model due to the complexity of the manufacturing process.

Despite conventional manufacturing processes, additive manufacturing machines print the part in single step with no need to manufacturing specialists. Once the model is designed, it can be uploaded to the machine and printed in few hours.

The production costs can be classified into 3 categories including material cost, machine operation cost and labor costs which are explained as follows [20]:

The material cost for additive manufacturing depends on the technology. Filaments used in FDM 3D printers cost around $30 per kg. The photo-sensitive resin for SLA 3D printers costs around $150 per liter. Polymer powder used in SLS printers costs around $70 per kg, while comparable pellets utilized in injection molding costs not more than $10 per kg. Although Material costs for additive manufacturing are significantly higher than other methods, it is worth considering that the wastage of materials in AM methods is lower [21].

Low-cost 3D printers consume the same amount of power as a desktop computer. Although industrial additive manufacturing machines use high powers to print a part, the capability to produce parts with complex geometries in a single step leads to higher efficiency and environmentally friendly production.

Another advantage of 3D printing is the low labor cost. Despite traditional manufacturing methods, where highly skilled specialists and operators are usually required the cost of labor for a 3D printer is almost zero. Post-processing aside, most of the additive manufacturing methods are automated and the operator is required to perform some simple setting.

Additive manufacturing is an appealing method at low volumes compared to conventional manufacturing methods. For verification of a prototype, it is significantly more economical than other manufacturing methods. However, traditional manufacturing methods become more cost-effective for mass production. In general, the cost of one part being fabricated by 3D printing is usually higher than that if it was mass produced. However, the higher cost is worth it for small production. The initial cost for traditional manufacturing is generally high due to the setup of CNC machines and tooling [22].

Despite all advantages of additive manufacturing, there are still some limitations and barriers to these methods. One of the barriers is the high-quality additive manufacturing machines leads to expensive machines. In addition, dimensional accuracy and the surface finish of parts are lower and require post-processing prior to using. Build rate of these methods can be higher compared to some of manufacturing methods dependent on the design. Furthermore, there is along way to development of materials which can be printed. Last but not the least, is their poor mechanical properties since these methods are layer by layer. For instance, achieving a transparent part by additive manufacturing is still a challenge [23].

1.1.4. Additive manufacturing and microfluidics

As it was discussed, the most common way for fabrication of microchannels relies on photolithography for master fabrication which possesses many limitations. These limitations make other fabrication methods such as 3D printing interesting for microfluidics. Recently, improvement in additive manufacturing in terms of material, resolution and printing time have led to ease fabrication process of microfluidic chips and 3D printing is fast becoming a key method in the fabrication of microfluidic devices. Publications on 3D printed microfluidics have been significantly increased in recent years. Number of publications related to microfluidics and 3D printed microfluidics are presented in Figure 1.1 [1].

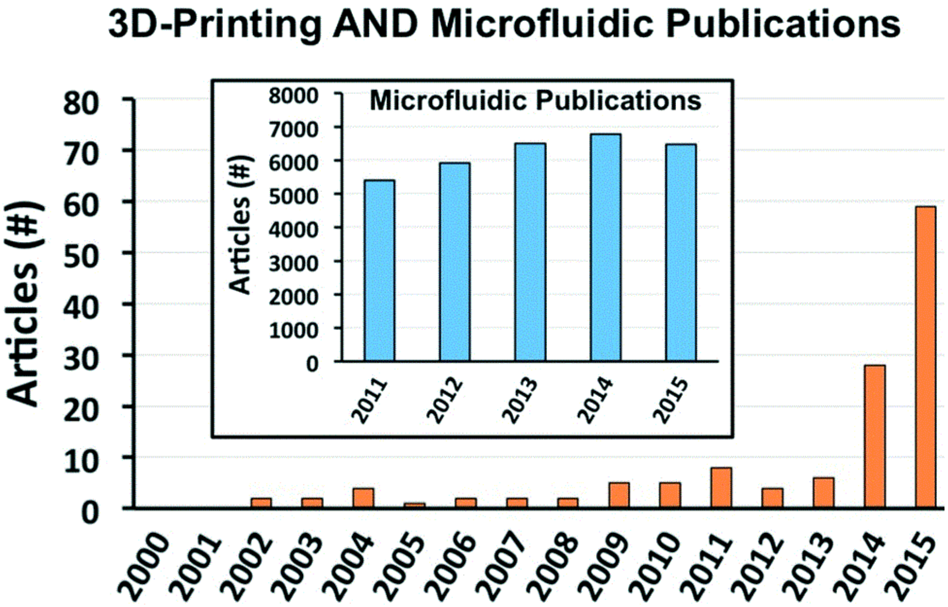

Figure 1-1 Publication trends. Blue bar-graph provides number of publications in the field of microfluidics in 2011-2015; orange bar-graph presents number of publications with keywords of "3D-printing" and "microfluidic" [1]

Fabrication costs and time could be reduced significantly by commercialized 3D printers. In addition, the process can be performed with one fully automated machine and can be readily replicated. In order to use 3D printers for biomedical microfluidic applications printing time, cost, resolution and material should be taken into account to obtain optimal results [24]. As was mentioned in the previous section, fabrication of small features on a master mold is a tedious and time-consuming process for fast prototyping. Multiple high resolution photomasks are required and it is a burdensome process to align and expose layers of photoresist in the soft lithography technique. On the other hand, additive manufacturing takes the STL file from CAD software and does not require masks for construction of micropatterns and provides a flexibility to the designer to fabricate a 3D model, with no considerable increase in printing cost, time and, complexity [25]. In addition, the design file can be shared simply which facilitate collaboration. Fabrication process of a microfluidic device for conventional methods and 3D printing method is compared in Figure 1.2.

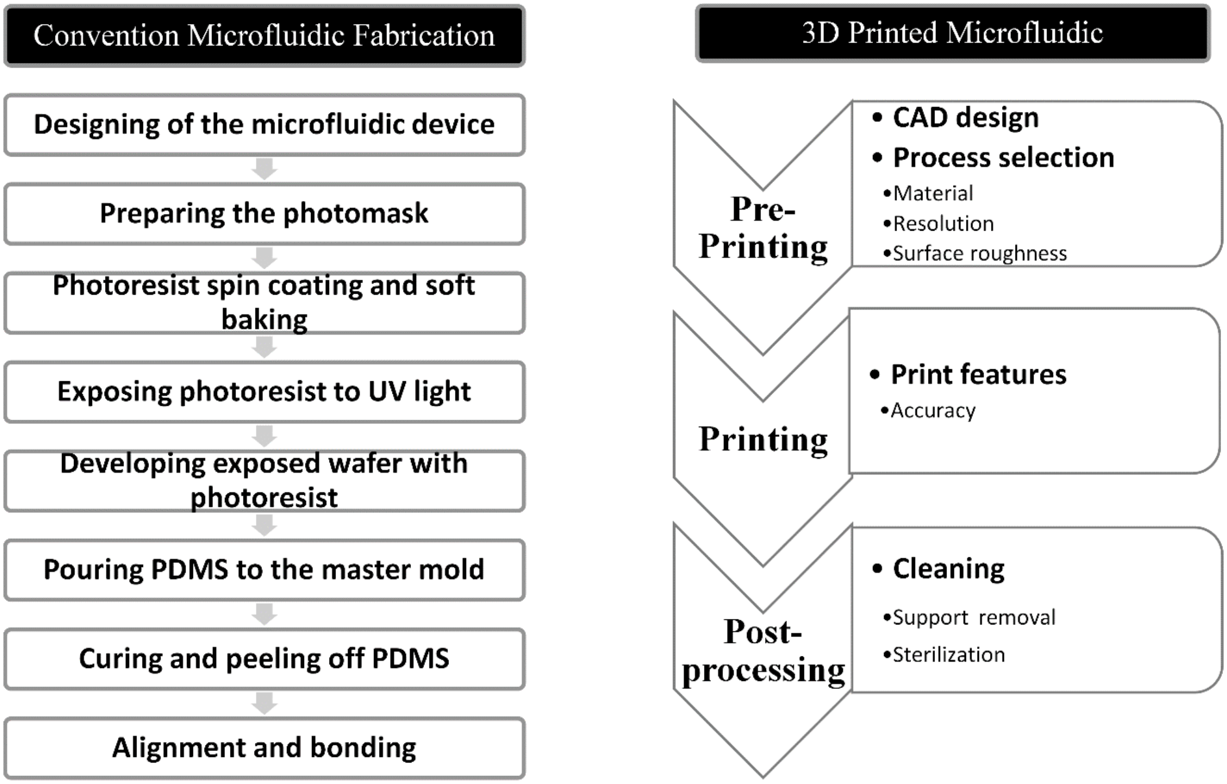

Figure 1-2 Comparison of conventional and 3D printing methods for microfluidic chip fabrication; process selection and design criteria are also illustrated for the 3D printing method

Recent advances in 3D printing methods have attracted many researches. 3D printing facilitates fabricating 3D channels in a way that has not been accessible earlier. This provides more freedom and alternatives in design in the area of microfluidics to researches and has been emerged new opportunities to manipulate fluids in three dimensions. In addition, it gives the ability to researchers to follow a “fail fast and often” strategy since the process to achieve the desired microfluidic chip require the designer to adjust the model. A complete microfluidic chip can be fabricated in less than an hour and the design can be altered easily for an agile iterative design [26]. Various additive manufacturing methods in comparison with conventional additive manufacturing methods in terms of resolution and automation are illustrated in Figure 1.3 [27]. As it can be seen in the figure, although conventional microfabrication methods have higher levels of resolution, these processes are mainly manual and not suitable for mass production of microfluidic devices.

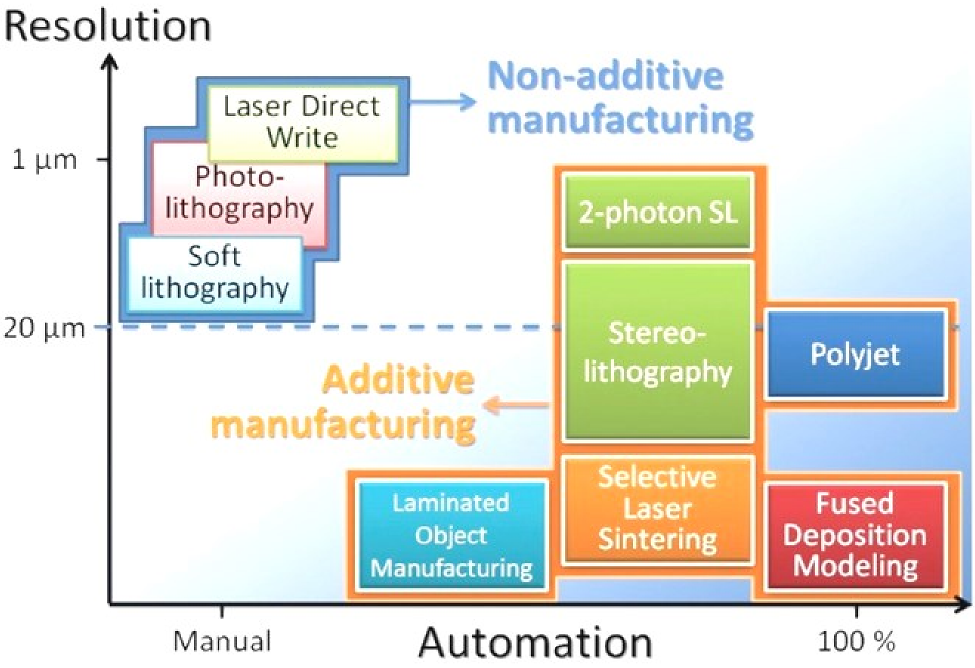

Figure 1-3 Automation and resolution trade-off in transition from conventional microfabrication methods to 3D printing [27]

At the beginning, 3D printers were used for fabrication of molds for polymer-based microfluidic devices. This method significantly facilitates the fabrication process compared to conventional methods. As the resolution of 3D printers improved, direct manufacturing of microfluidic devices were achieved. Application of these devices for biomedical purposes are mainly developed from 2013 onward. With improvement in resolution and materials, devices consist of dynamic structures such as mixers and valve can be fabricated directly [28].

1.1.4.1. Limitation of current 3D printing methods

As an emerging and rapidly growing technology, 3D printing also possesses some restraints in terms of resolution, surface properties, and compatibility.

In spite of the fact that, the resolution of many commercial 3D printers has claimed to be as low as a few microns, the smallest 3D printed channel is 200 µm wide. Most of current 3D printed microfluidic devices have reported a channel size from hundreds of microns to a few millimeters [29], [30]. This is usually due to resin sticking in the microfluidic channel. This led to using 3D printed mold instead of direct printing of a microfluidic device. The low resolution leads to rough surface profile in a 3D printed microfluidic channel [28].

In addition, many 3D printing materials suffer from absorption and adsorption. Some of 3D printing materials absorb lipids and proteins, which may result in a reduction in the concentration of analytes of interest and changing the sensitivity of the sensor [31]. However, some protocols have been reported to avoid the biotoxicity concern and improve the surface roughness. For instance, a layer of PDMS was coated successfully in a 3D printed channel in order to culture endothelial cell [32].

The biocompatibility of most of resins used in 3D printers is unknown. However, the photoinitiator used in SLA resin can negatively affect cell culturing. Few biocompatible 3D printing resins have been introduced by several companies that are expected to be non-toxic to biological samples. However, most of these resins are not flexible [33].

In addition to these points, PDMS devices are completely transparent and suitable for optical detection. Although "clear resins" are available for many 3D printers, the printed part with these resins usually are semi-transparent. Post-processing and polishing are required to make the part clear while the printed channels still remain translucent. Therefore, optical observation of the channel is unfeasible. Moreover, despite of PDMS which is gas permeable, most of the 3D printing resin are not, which makes them not applicable for cell culturing inside a channel.

1.1.4.2. Polymer-based microfluidics and 3D printing

Polydimethylsiloxane (PDMS) is the most common polymer being used in the field of microfluidics. It possesses several superior properties including biocompatibility, oxygen permeability, being relatively inexpensive, optical transparency, water impermeability, flexibility and moldability with a submicron resolution [34]–[36]. In addition, PDMS is not a toxic material for biological samples and cures at relatively low temperatures. Moreover, it is a preferable material for microvalves and micropumps fabrication [27], [37]. it has been used in a wide range of applications such as cell culturing, microfluidics, medical devices, and electronics [38]–[41].

However, fabricating a mold for microfluidic applications is a dominantly manual process and requires expensive facilities. These problems have hindered the commercialization of Polymer-based microfluidic devices and translation of them from research labs to biomedical companies [1]. In order to overcome these problems, the manufacturing cost per unit needs to significantly reduce.

Direct additive manufacturing of PDMS is still in its initial phase of development. Three considerable challenges for 3D printing of PDMS are its low viscosity, long gelation time and low elastic modulus [42]. Although, the low viscosity of it allows deposition from an extruder, the long gelation and curing time prevent it from construction of a model. In addition, printing a structure with PDMS requires supports due to its low Young's modulus.

However, several research groups have attempted to 3D print PDMS with various techniques. These methods mostly are based on either adding a material to increase the viscosity or adding a photoactive cross-linking agent to print it with SLA 3D printers. Wessling group have developed a PDMS based resin by adding a photoinitiator to PDMS. However, optical transparency of PDMS was sacrificed due to the photoblocker added to PDMS [43]. In addition, biocompatibility of the photoinitiator has to be taken into consideration. Recently, a PDMS ink was developed by adding a SE 1700 elastomer to PDMS [44]. However, the ink does not possess the same mechanical properties and transparency of PDMS and is limited to the construction of 2.5D geometries with a relatively low resolution. In addition, a method to 3D print PDMS in a support bath is reported which suffers from a low resolution and limitation in fabrication and design [42]. The last two explained methods are not able to construct a part in order of microns. Recently, a PDMS-based resin for SLA 3D printer was introduced in a paper published in Advanced Material journal [45]. However, printed parts with this resin requires multiple steps to make them suitable for cell culturing. The models printed with above-mentioned methods are illustrated in Figure 1.4.

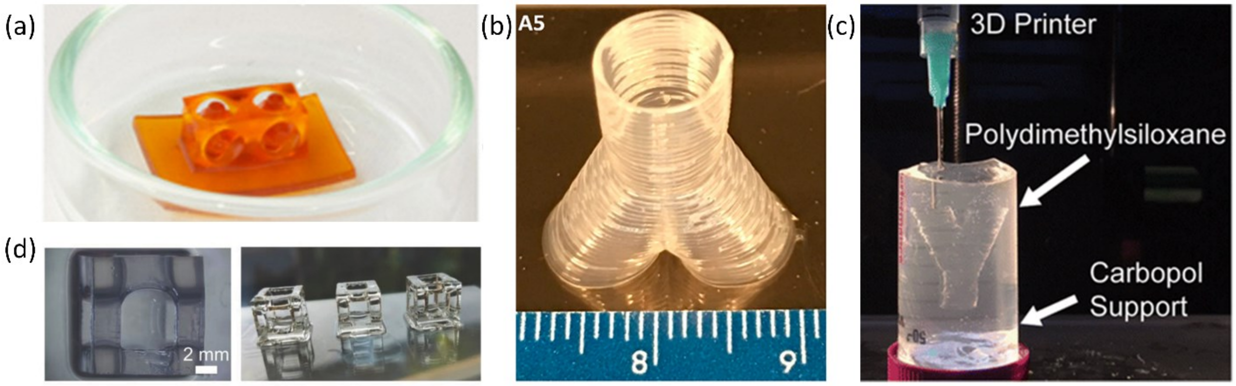

Figure 1-4 3D printed parts with PDMS; (a) by adding a photoinitiator to PDMS [43]; (b) by adding a SE 1700 elastomer to PDMS [44]; (c) by using a support bath to 3D print PDMS [42]; (d) transparent part by adding a photoinitiator [45]

Overall, all 3D printing methods suffer from several major problems including a low resolution for microfluidic applications and different mechanical and chemical properties due to adding additional material to PDMS. Therefore, a method that can additive manufacture PDMS without adding additional materials and while providing a high resolution is essential to overcome these limitations. This can be a step forward to translate PDMS to a commercial scale and lead to facilitation and improvement in the fabrication of microfluidic devices. In the next section, an additive manufacturing method is presented that can rapidly print polymer-based devices with a relatively proper resolution for microfluidic applications.

1.2. Objective of the thesis

The objective of this thesis is to develop an additive manufacturing method to rapidly fabricate 3D printed structures using thermosetting polymers. The proposed method was finally applied to fabricate a fluidic channel. More specifically, the objectives of the thesis are the following:

1. Literature review on current status of methods to fabricate a microfluidic device and the future of 3D printing of 3D microfluidic devices
2. Fabrication of 3D microfluidic devices by a commercialized 3D printer and characterization of printed devices
3. Design, fabrication, and development of an acoustic-assisted additive manufacturing method by using a HIFU transducer in order to selectively solidify polymer by heat induced by focused ultrasound
   3.1. Modeling of the acoustic wave and the heat induced by that in order to optimize the additive manufacturing process prior to the experiment
   3.2. Fabrication of channels with a biocompatible material

Altogether, a promising additive manufacturing method toward printing a polymer-based device by using an acoustic assisted 3D printing method will be presented. This method is based on heat induced by a high intensity focused transducer to selectively solidify the thermoset resin. This method can significantly simplify and improve fabrication of microfluidic devices. This fully automated, rapid process can guide microfluidics towards the development of low-cost, more commercially devices.

1.2.1. Ultrasound transducers

Sound is a longitudinal, mechanical wave that produces vibrations that propagate through any medium and these sound waves transfer energy over distance without matter being transferred. Vacuum contains no particle to vibrate and cannot sustain waves at all. The wave frequency as a basic characteristic of sound indicates how often the particles vibrate while a wave passes through the medium. In other words, it identifies the number of vibrations per second. The human audible range is generally 20 Hz to 20 kHz. Sound waves with a frequency higher than this are considered as ultrasound and cannot be sensed by human [46], [47].

Prior to applying of ultrasound in medicine, it was used to detect and characterize submerged objects in water. After the World War II, scientists started to use ultrasound in medicine in order to treat diseases in the body. In 1942, the first sonography device for medical diagnosis was invented by researchers from Japan. In 1960's, pulsed Doppler ultrasound technology was applied in order image flow in various layers of the heart. Later, ultrasound was applied for Non-destructive testing for flaw detection and thickness gaging [48].

The concept of generating sounds with high frequencies is based on a piezoelectric actuator which converts electrical pulses to mechanical movement, and mechanical vibration to electrical pulses. An ultrasonic transducer or ultrasonic sensor converts electrical signals into ultrasound waves, and vice versa. These transducers can be categorized into receivers, transmitters, and transceivers. The heart of the transducer is a piezoelectric crystal which is a polarized material that produces electricity when subjected to mechanical forces. This phenomenon is called piezoelectric effect.

In the early 1950s, quartz crystals were the most common material for piezoelectric crystal transducers. Piezoelectric ceramics were used later. A piezoelectric ceramic is the active element of most acoustic transducers which are made of fine PZT powder and a mass of ceramic crystals. These elements can be manufactured in a wide variety of sizes and shapes and operate at low voltages as well as being functional up to 300°C. These factors made it the dominant material for transducers. The most widely used ceramic transducer materials are lead zirconate titanate (PZT) compositions [49].

The actuation frequency of the transducer determines the thickness of the active element. The vibration of a wafer element happens with a wavelength that is two times its thickness.

Accordingly, piezoelectric crystals are cut to a thickness that is half the desired wavelength. Consequently, manufacturing transducers for high frequencies which lead to the thinner active element is costly. Therefore, production of high-frequency contact transducers is limited, since these elements are very thin and fragile [50].

1.2.2. HIFU transducers

High intensity focused ultrasound (HIFU) transducer is an ordinary ultrasound transducer that consists of a bowl aperture. Therefore, it has remarkably higher intensities in a small region called the focal region of the transducer. Due to the spherical geometry of the HIFU transducers, they can precisely deposit intensive acoustic energies in the focal region. The deposition of HIFU energy leads to a rapid temperature rise in the focal zone. Therefore, these transducers are widely used to deliver heat into the body. HIFU transducers have several applications on biomedicine including non-invasively ablation of tumors and breaking up kidney stones. HIFU was utilized for the first time in 1950's in order to examine tumor ablation [51].

In contrast with diagnosis ultrasound transducers, high intensity focused ultrasound transducers offer ultrasound with intensities that differ between 100 to 100000 W/cm^2 [52]. In addition to the temperature rise, the acoustic field of the HIFU transducer results in cavitation and streaming within the focal zone. The acoustic pressure field generated by the HIFU transducer depends on the transducer geometry, input power, and frequency. Another method to generate high-intensity focused field is by using two-dimensional arrays of transducers [53].

High intensity focused ultrasound transducers have only been used in biomedical applications. However, it possesses a great potential for applications that require a rapid temperature rise within a small region. In this thesis, HIFU transducers will be utilized for additive manufacturing for the first time.

1.3. Contributions

1. Karamzadeh, V., Foroughi, Sh., Kashani, A., and Packirisamy, M. Characterization of a 3D Printed Mold for a Cell Culturing Microfluidic Device. 5th International Conference of Fluid Flow, Heat and Mass Transfer, Niagara Falls, Canada, June 7-9, 2018.
2. Foroughi, Sh., Karamzadeh, V., Habibi, M., and Packirisamy, M. Numerical Analysis of Acoustic Propagation inside Multiple Liquids. 5th International Conference of Fluid Flow, Heat and Mass Transfer, Niagara Falls, Canada, June 7-9, 2018.

3. Foroughi, Sh., Karamzadeh, V., and Packirisamy, M. Design and Analysis of a Close-Loop Opto-Electrothermally Actuated Cell Microgripper. 20th International Conference on Mechanical Engineering, Montreal, Canada, May 24-25, 2018.
4. Karamzadeh, V., Adhvaryu, J., Chandrasekaran, A., and Packirisamy, M. A Simplified, Fabrication-friendly Acoustophoretic Model for Size Sensitive Particle Sorting. 20th International Conference on Biomedical Devices, Sensors and Signal Processing, Montreal, Canada, May 24-25, 2018.
5. Karamzadeh, V., Foroughi, Sh., and Packirisamy, M. Characterization of a 3D Printed Mold for a Droplet Generation Microfluidic Device. (Journal paper to be submitted).
6. Foroughi, Sh., Karamzadeh, V., Habibi, M., and Packirisamy, M. Study the effect of lamilar orientation in layer-by-layer 3D printing for fabrication of free standing structure. (Journal paper to be submitted).

In the next chapter, types of additive manufacturing methods will be discussed. In addition, two techniques for fabrication of microfluidic devices using additive manufacturing will be studied.

Chapter 2

2. Types of additive manufacturing methods

There are several methods for additive manufacturing available in the commercial market. The main factors in selecting the machine of choice are material, resolution, printing time, price, and build size. In this chapter, first additive manufacturing method will be introduced in brief. Then, additive manufacturing methods that are suitable for fabrication of microfluidic channels will be presented. Finally, two common methods for fabrication of microfluidic devices using additive manufacturing will be discussed.

2.1. Additive manufacturing methods classification

There are many additive manufacturing processes which are different in terms of the material or machine technology. Therefore, in 2010, the American Society for Testing and Materials (ASTM) group classified the range of Additive Manufacturing technologies into 7 categories [54]. These categories are:

1. **VAT Photopolymerisation**: method that uses photo-sensitive polymers in a vat to selectively solidify resin using UV-light
2. **Material Jetting**: method that constructs 3D parts in a similar way to a regular inkjet printer
3. **Binder jetting:** powder based material and a binder are used in this method by depositing layers of the base material and the binding material. The base material is usually in powder form and the binder in liquid form
4. **Material Extrusion:** refers to a method in which thermoplastic material is drawn through a heated nozzle to build a 3D subject layer by layer. This method is known as Fused Deposition Modeling (FDM).
5. **Inkjet Printing:** method that deposits droplets of ink onto a substrate by using thermal, piezoelectric, or electromagnetic technology.
6. **Sheet Lamination:** refers to a technology that includes laminated object manufacturing
7. **Directed Energy Deposition:** a range of methods including: 3D laser cladding, direct metal deposition, directed light fabrication and laser engineering net shaping which are more advanced methods are being used to repair or add material to existing components [55].

In addition, another classification approach is to classify 3D printing methods according to the state of the material [56]. Figure 2.1 is a representation of this classification.

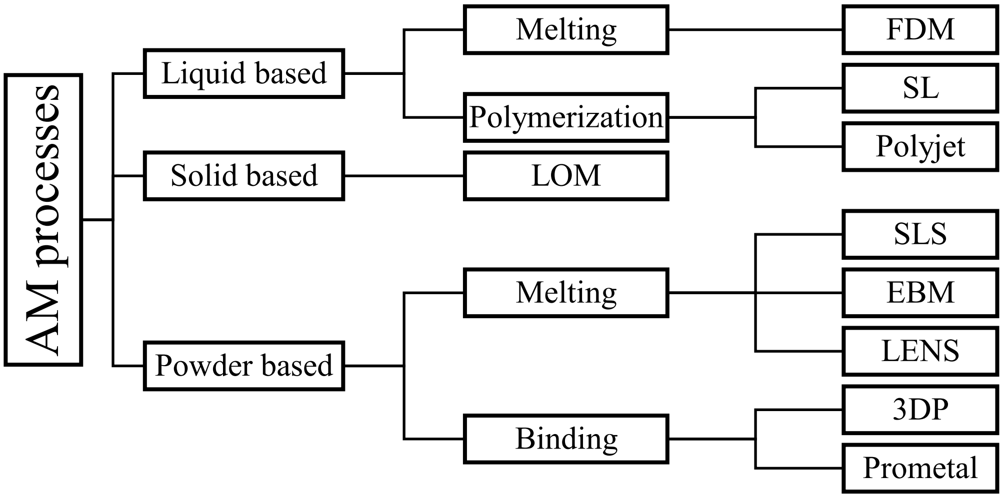

Figure 2-1 Additive manufacturing process classification based on the state of the material

Other classification methods have also been reported based on material properties, comprising plastic, metal, ceramic and biomaterial.

2.2. Additive manufacturing technologies

2.2.1. Stereolithography (SLA)

SLA is the first commercialized additive manufacturing method which was introduced by Chunk and commercialized at 3D systems [57]. These 3D printers utilize ultraviolent light to selectively solidify liquid polymer in a layer-by-layer manner, constructing a 3D structure on a build platform. Photopolymerisation of a photo-reactive liquid resin is accomplished by a scanning laser or a digital light projector (DLP). One of the limitations of SLA 3D printers is that the liquid resin must be a photo-sensitive resin. The SLA resins are usually epoxy-based or acrylic-based [58].

Several research groups have fabricated microfluidic devices using a SLA 3D printer [41], [59], [60]. SLA 3D printers have been used for fabrication of the molds for PDMS-based microfluidic devices and single step printing of unibody microfluidic devices. The main limitation of fabrication of microfluidic devices with SLA 3D printers is having to remove the viscous uncured resin. This leads to curing resin inside of small channels. In addition, explosion depth of the laser beam has to be taken into account as another restraint in fabricating channels with a diameters smaller than 200 μm [61]. The method is presented in Figure 2.2 (b)

2.2.2. Fused Deposition Modeling (FDM)

FDM was initially introduced by Crump in 1992 and is the most common and cost-effective method for fast prototyping [62], [63]. FDM is a thermoplastic filament-based technology which deposits a thermoplastic material through an extruder, layer by layer. In FDM printers, the resolution is a factor of the nozzle size and the positioner. FDM uses inexpensive biocompatible materials such as poly(lactic acid) and acrylonitrile butadiene styrene (ABS) [27]. Fabrication of microfluidic devices using FDM 3D printing method has been reported [64], [65]. However, this method suffers from low resolution and high surface roughness which is not applicable for most the microfluidic devices. This method is illustrated in Figure 2.2 (a).

2.2.3. Photopolymer jetting

Photopolymer jetting was first introduced by Gothait in 2001 [66]. This method uses the same concept as inkjet printers to deposit photopolymer liquids onto a build platform. The polymers are then solidified by UV light in a layer-by-layer manner. This approach has been investigated to fabricate microfluidic chips [67], [68]. The price of these 3D printers is relatively high compared to SLA and FDM 3D printers.

2.2.4. Material jetting

Material jetting additive manufacturing method uses inkjet print heads in order to jet melted materials on a build platform as illustrated in Figure 2.2 (d). A solid structure is formed by cooling the wax-like material. This process is capable of printing multiple material parts with various colors in a single printing process. Since the material must be deposited in forms of drops, the number of materials that can be used for this method is limited. This method has been applied for additive manufacturing of polymers, metals, ceramics, and biomaterials [69], [70].

2.2.5. Binder jetting

Binder jetting additive manufacturing technique is similar to photopolymer and material jetting methods unless the inkjet heat deposits a liquid adhesive onto thin layers of powder on a build platform as shown in Figure 2.2 (c). Powder particles are bound together to produce a 3D structure layer-by-layer in the powder bed. The main advantages of this method are printing without any support material and being capable of applying any material that is accessible in the form powder [71], [72].

2.2.6. Laser melting

Laser melting was introduced in 1995 at the Fraunhofer Institute ILT. Laser Melting 3D printers use a laser source to draw a pattern on a layer of powder to solidify a desired path. They construct a 3D part by a metal powder. The part is anchored to the build platform to allow heat transfer from the part to decrease thermal stress. This method is relatively slow and expensive [73].

2.2.7. Laser sintering

The working principle of laser sintering additive manufacturing is similar to laser melting. This method uses a laser as the power source and scanning mirrors to melt and coat a thin layer of plastic powder onto a build platform. Layers sinter and plastic powder layer is deposited for the next layer. 3D parts are built in the powder bed by repeating the process. In this method, the model can be printed without a support structure. This technique requires high-powered lasers that are often expensive [74].

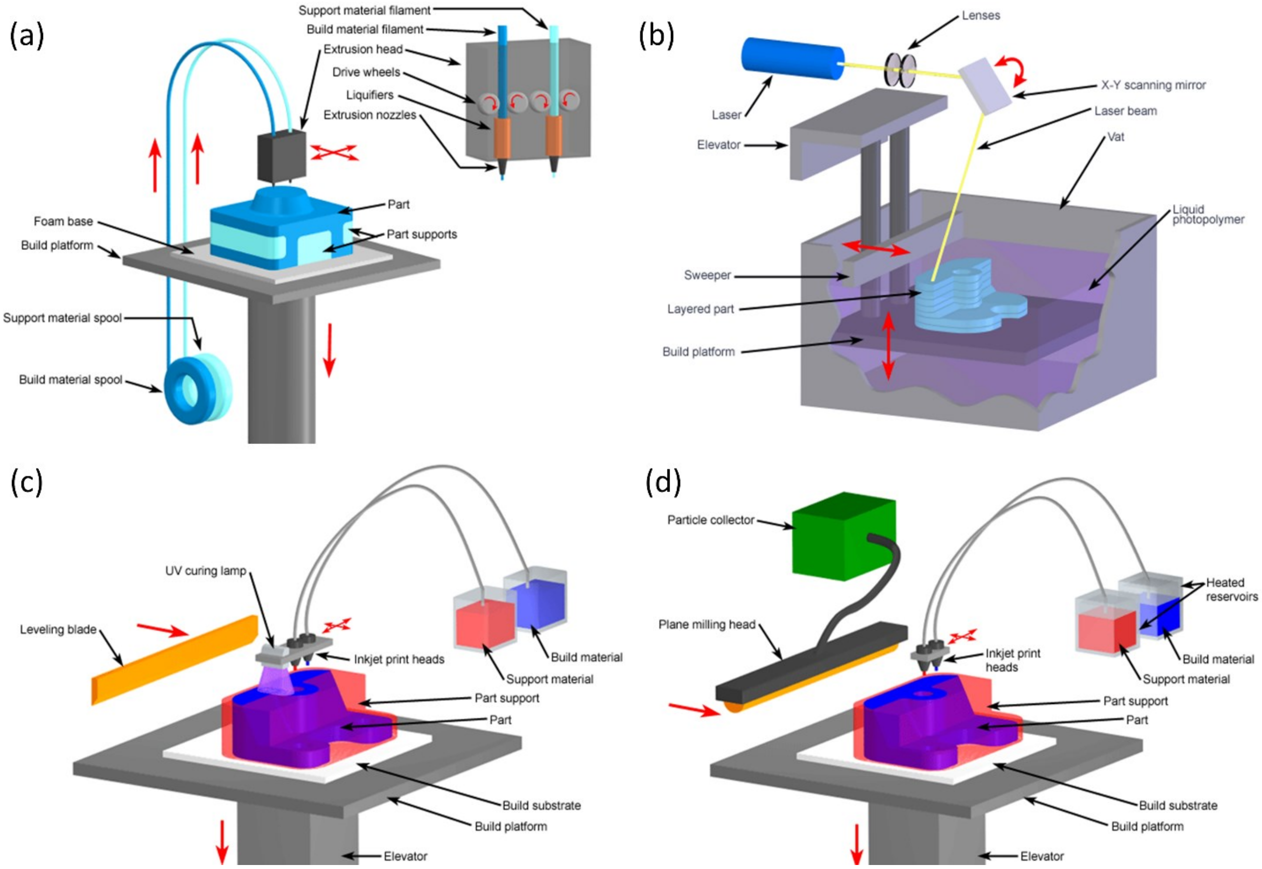

Figure 2-2 Various 3D printing methods for microfluidics. (a) Fused deposition modeling; (b) Selective laser sintering; (c) Photopolymer jetting; (d) Material jetting. Images courtesy of custompartnet.com.

2.2.8. Electron beam melting

The working principle of electron beam melting is similar to laser melting unless an electron beam melts the metal powder instead of a laser source. The main advantage of this method compared to the laser melting method is generation of lower thermal stress that decreases the number of support structures and leads to faster fabrication [54].

2.3. 3D-printed microfluidic fabrication methods

3D printing can be used for fabrication of microfluidic devices in two different ways. First, it can be used to print a master mold to fabricate polymer-based microfluidic devices. In a different approach, microfluidic chips can be printed in one single step. In both approaches, additive manufacturing replaces the expensive cleanroom facilities and facilitates fabrication of devices with complex geometries and reduces fabrication cost and time significantly [75]–[77]. Additive manufacturing technologies that fabricate microfluidic devices are mainly based on methods in which photopolymer resin is used as the material. These methods include SLA, inkjet printing and binder jetting. In addition to photo sensitive resins, thermoplastic materials is used in other techniques such as FDM. Here, two common approaches for fabrication of microfluidic devices using 3D printer will be discussed.

2.3.1. Fabrication of mold for Polymer-based microfluidic devices

Fabrication of polymer-based microfluidic devices using 3D printed molds presents several advantages compared to conventional methods. PDMS material properties such as biocompatibility and transparency are maintained in this method. In addition, this method reduces fabrication costs and time. Also, it does not suffer from disadvantages of photopolymer resin with unknown biocompatibility and surface properties. Molds for microfluidic devices with features of 150 μm can be achieved by using this method. A smaller channels can be printed by this method compared to single step printing a microfluidic device.

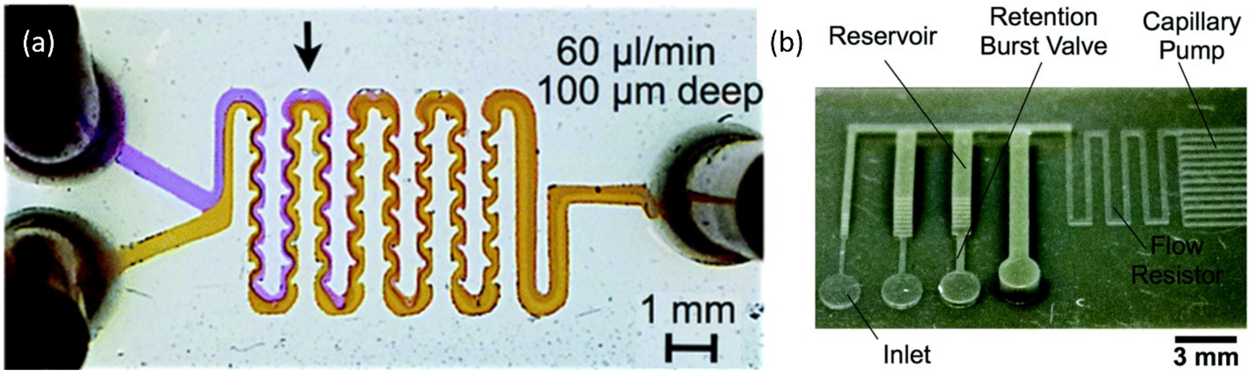

Figure 2-3 PDMS-based microfluidic devices fabricated by 3D printed molds. (a) 100 µm deep chaotic mixer [41]; (b) a 3D printed mold for autonomous microfluidic capillaric circuit [78]

3D printed microfluidic molds have been studied by many researchers using different 3D printers and a number of them have sought to determine the feasibility of this method. In 2013, Comina et al. published a paper in which they used 3D printed templates which were fabricated by a DLP 3D printer for glucose sensing [41]. PDMS casting and characterizing the roughness of 3D printing has been demonstrated in a report by Bonyar et al [78] and a new method for fabricating helical channels by 3D printing the structure, casting PDMS around it and removing the structure from the molds was used by Hwang et al [79]. In this research, a microfluidic device for cell stimulation was achieved by 3D printed templates [80]. Chan et al. proposed three-step procedures for post-treating of 3D printed masters due to their issue for direct molding [76]. In addition, a novel capillary-driven microfluidic device was fabricated by Olanrewaju et al. [81]. Also, Kang reported a soluble 3D printed master for PDMS casting and created channels smaller than 200 µm [82]. This method can overcome the low resolution of 3D printers. Moreover, Didar lab has recently demonstrated a method that reduced the roughness of microfluidic channels which were fabricated by a 3D printed mold from 2 µm to 0.2 µm [83]. In view of all that has been mentioned, 3D printing can improve and accelerate research in the field of microfluidics. In addition, low-cost 3D printed molds can make it accessible to more research labs. However, one of the major barriers in commercialization of microfluidic devices remains by using this method since it includes several manual fabrication steps such as post-treating the mold and plasma bonding to glass.

2.3.2. Single step fabrication of a microfluidic device

Microfluidic chips have also been printed in one single step. These microfluidic devices entail no additional component to complete. This method can automate the process wherein a complete microfluidic device is printed with no operators and reduce the time and related training. Indeed, following printing, simple post-treating steps include resin cleaning or support removal are required prior to using the device. In addition, 3D printing simplifies making complex 3D microfluidic networks.

FDM 3D printers are limited because of the printer nozzle. A melted thermoplastic filament spreads out before cooling and turns to the desired shape. In SLA 3D printers, the uncured photopolymer within internal channels must be flushed to achieve a microfluidic channel. This resin can be easily removed by a vacuum, especially for low-viscosity resins [84].

Most 3D printed microfluidic devices are in the range of 0.5 mm to 1 mm which make them suitable for many applications, but there are still limitations for many analytical applications. Recently, Macdonald et al. compared a Y channel microfluidic model with an interior channel as small as 150 μm created by FDM, poly jet, and SLA 3D printers. Surface roughness, post-processing steps, device cost, and fidelity were evaluated by them. They concluded that poly jet printers have high resolutions but are high-priced and flushing of channels are difficult; FDM 3D printers provide range of biocompatible materials and low-cost 3D printers but the resolution is not suitable for most of microfluidic applications; SLA 3D printers offer lower fabrication throughput compared to PJ printers, but they render the smoothest and well-defined channels with simple post-treating [85].

Nordin Group has developed a customized resin and SLA 3D printers that can print channels as small as 18 μm × 20 μm. Twenty absorbers were tested and they introduced a new mathematical model in order to characterize the photopolymer resin optical penetration depth [86]. Recently, a 45 3D printed valve array with a diameter of 300 μm was fabricated by them. These valves were tested to 10000 actuates and no sign of valve failure was observed[87]. Fabrication of this device by conventional micro fabrication methods is tedious and almost impossible.

Recently Albert Folch group introduced a 3D-printable PDMS resin that can be used in SLA 3D printers. An optically transparent microfluidic device was demonstrated by them. In addition, it was shown that the 3D printed device can be used for culturing mammalian cells. However, several post-processing steps is required to make it suitable for biological samples which take approximately 2 days. An organic solvent was used to flush the uncured resin and penetrate to extract toxic photo initiator. They have reported 90% viability of cells after post-treating which is comparable with cured Sylgard-184 PDMS [45]. The above mentioned printed parts are illustrated in Figure 2.4.

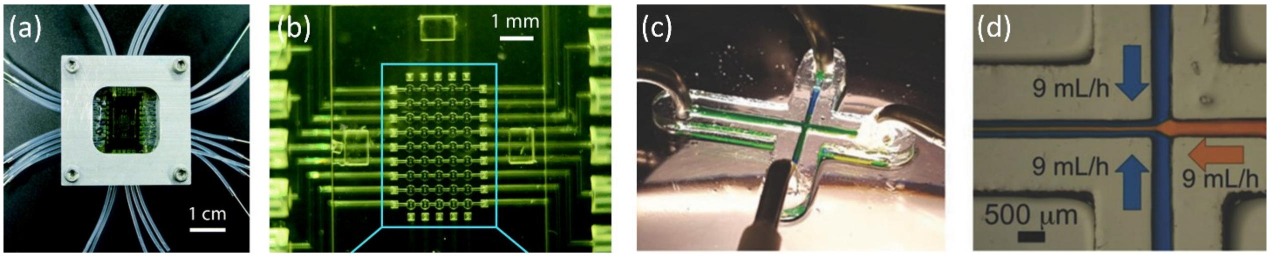

Figure 2-4 Direct printed microfluidic devices; (a) and (b) 45 microfluidic valves fabricated in a single step [87]; (c) and (d) a transparent microfluidic device fabricated with a PDMS-based resin [45]

Finally, it is expected that printing resolution and material to be rapidly advanced in future. These studies indicate that additive manufacturing procedures for microfluidic device fabrication are relatively fast and simple compared to traditional microfabrication methods. In addition, it provides flexibility in design which was not possible before. In the next chapter, a numerical method will be presented to demonstrate the potential of using high intensity focused transduces for additive manufacturing of polymer-based microfluidic devices.

Chapter 3

3. Simulation

3.1. Introduction

A model which mimics a physical phenomenon could be a tool for improving the device and studying the effects of different parameters such as materials, frequency, and power on temperature rise and curing process. In this chapter, the simulation of the acoustic wave and the heat induced by that is presented to optimize the printing process for a channel. The printing resolution and printing time can be enhanced by these parameters. The COMSOL® Multiphysics v5.3 (COMSOL, Burlington, MA) acoustic and heat transfer modules are used for the finite element analysis of this model. FEM of a 2D axisymmetric model is used instead of a 3D model to reduce the computational cost. The curved surface of the ultrasound transducer leads the waves to converge at a focal point, which is located in the resin tank. The HIFU transducer is modeled with an inner diameter and outer diameter of 22.6 mm and 64 mm, respectively.

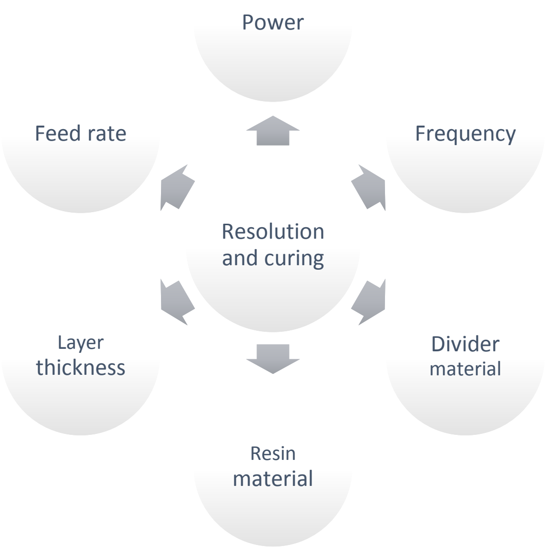

Figure 3-1 Leading parameters in the printing process

The printer resolution and curing time are dictated by parameters mentioned above. Feed rate and layer thickness are defined in the G-code. Here, the impacts of each of these parameters are investigated and discussed.

3.2. Geometry

3.2.1. Channel geometry

The designed device consists of a channel with a depth of 800 um and a width of 1.6 mm. This model requires high resolution in the channel part. However, a lower resolution can be used for other parts of the device to accelerate the printing time. Therefore, the influence of different parameters such as spot size, frequency, and power is needed to be taken into account to achieve a high resolution printed part in the least time.

3.2.2. Model geometry

The domain consists of three regions, water, divider and resin. It is modeled in 2-D axisymmetric geometry, as demonstrated in Figure 3.2. The transducer is depicted in yellow. The opening to the right of the transducer is considered to model a hole in the center of the transducer in which a hydrophone is usually placed. Perfectly Matched Layer (PML), also known as absorbing boundaries is used to absorb the outgoing waves.

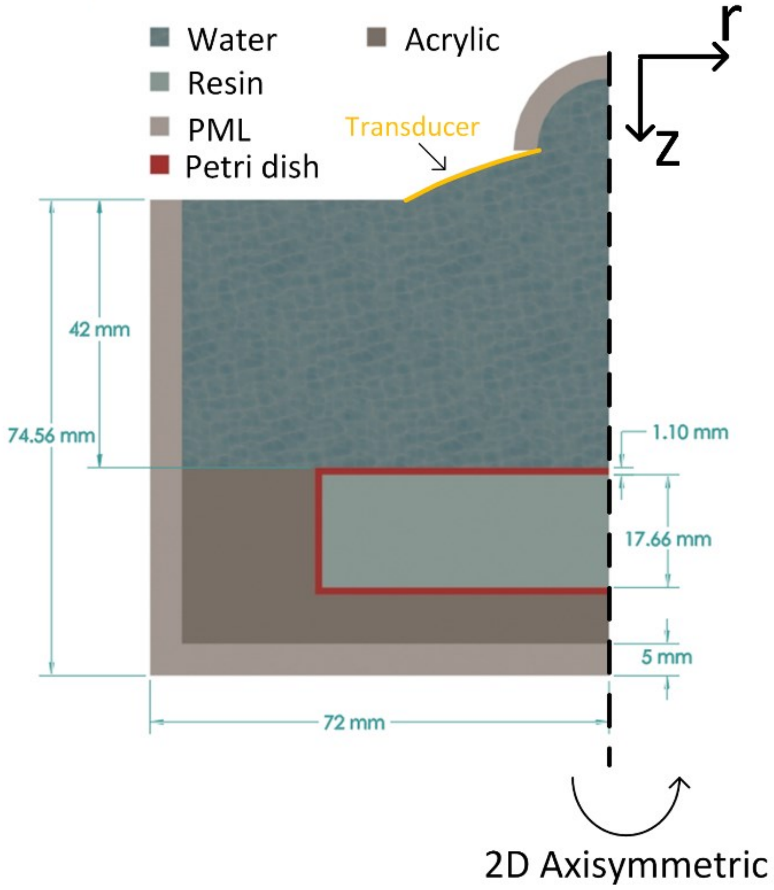

Figure 3-2 Model geometry

3.3. Acoustic field theory

When a particular volume of resin is passed by an ultrasound beam, the emitted acoustic energy in the form of pressure waves is mostly absorbed by the material and generates heat. The transducer is immersed in water and the resin is separated by a divider with an acoustic impedance close to water's to decrease the absorption of acoustic waves through the divider. The transducer is driven at the frequency of 2.15 MHz.

The pressure acoustic module in the frequency domain interface is used to model the stationary acoustic field in the water and the resin domains to obtain acoustic intensity distribution in resin. The absorbed energy by resin is computed and used as the heat source for the heat transfer interface model.

3.3.1. Ultrasound Equation

In order to model ultrasound physics, the Helmholtz equation which represents a time-independent form of the wave equation was solved in 2D axisymmetric cylindrical coordinate:

$$\frac{\partial}{\partial r}\left[-\frac{r}{\rho_c}\left(\frac{\partial p}{\partial r}\right)\right]+r\frac{\partial}{\partial z}\left[-\frac{1}{\rho_c}\left(\frac{\partial p}{\partial z}\right)\right]-\left[\left(k_p\right)^2\right]\frac{rp}{\rho_c}=0 \tag{1}$$

Where $k_p = \frac{\omega}{c_c} - i\alpha$ is the wave number, p is the acoustic pressure, ω is the angular frequency, α is attenuation and r and z are the radial and axial coordinates. The density, ρ_c, and the speed of sound, c_c, are complex-valued to account for the material's damping properties. The complex density ρ_c is dependent on density, speed of sound, and the complex speed of sound c_c:

$$\rho_c = \rho_t \times (\frac{c_0}{c_c})^2 \tag{2}$$

where c_0 represents the signal sound speed and c_c is the complex speed of sound, defined as:

$$c_c = \frac{\omega}{k} \tag{3}$$

Equation 1 is solved using the PARADISO direct solving method [88].

In the Equation 1, it is assumed that the amplitude of shear waves in the domain is much smaller than that of the pressure waves and the acoustic wave propagation which is linear. Therefore, each successive wave is identical to the previous one. Consequently, shear waves and nonlinear effects are neglected. However, it provides valuable information about the sensitivity of the focal zone to the transducer parameters.

Density of the medium and the ultrasound wave velocity were considered as functions of temperature and frequency and they were set as 998 kg/m^3 and 1483 m/s^2 in 21°C, respectively.

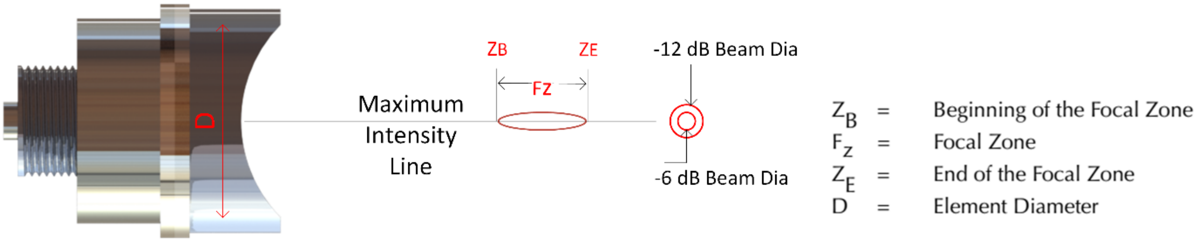

Figure 3-3 Focal zone is depicted

The size of the focal zone is reduced by increasing the frequency. The beam diameter or focal width which is equal to -6 dB pulse-echo of the beam diameter can be calculated using Equation 4 [89].

$$BD(-6dB) = 0.2568DS_f \tag{4}$$

where D is the element diameter and S_F is the normalized focal length which is determined by the Equation 5.

$$S_F = \frac{F}{N} \tag{5}$$

where N is the near field distance calculated by $N = \frac{D^2 f}{4c}$. The two ends of the focal length are located where the on-axis intensity drops to -6 dB of the focal point. The length of the focal zone is given by Equation 6 [90]:

$$F_Z = N \times S_F^2 [\frac{2}{1 + 0.5 S_F}] \tag{6}$$

The given formulae gives us the focal width and the focal depth as 0.70 mm and 5.27 mm for the transducer at the frequency of 2.15 MHz.

The displacement amplitude (ξ) of the transducer is dependent on the input power and frequency of the transducer according to the following equation:

$$I = \frac{P}{A} = \frac{\xi^2 \omega^2 Z}{2} \tag{11}$$

In this simulation, the displacement amplitude (ξ) is 21.2091 nm which is correlated to the input power of 218 W with efficiency of 85 % and the frequency of 2.15 MHz. A is the area of the transducer surface and Z is the acoustic impedance of the medium through which the wave is propagating. The acoustic impedance determines the transmission and the reflection of the wave when it passes a boundary with another material. The acoustic impedance is related to the density of the medium and the speed of the sound through that medium. They are related to each other:

$$Z = \rho \times c \tag{12}$$

Therefore, the augmentation of the density, results in an increase of acoustic impedance. Here the acoustic impedance of water is used when determining the displacement amplitude of the transducer head.

3.4. Heat transfer field

Heat transfer in the domain is governed by the heat transfer equation:

$$\rho c_p \frac{\partial T}{\partial t} - \nabla . (k \nabla T) = \dot{q}_v \tag{7}$$

where $\dot{q_V}$, is the volumetric heat source; more specifically the absorbed ultrasound energy calculated from the acoustic wave simulation, T is the temperature, ρ is the mass density of the material, k is the thermal conductivity and C_p is the specific heat. $k\nabla^2 T$ governs the thermal diffusion through the domain. In this model, water properties such as density and attenuation are changed by temperature rise and frequency.

The term associated with the heat source from the acoustic wave simulation; $\dot{q_V}$ must be determined by the following equation:

$$\dot{q_V} = 2\alpha I \tag{8}$$

where I is the intensity of the acoustic field and α is the attenuation coefficient of the domain.

The intensity is defined by:

$$I = \sqrt{I_z^2 + I_\emptyset^2 + I_r^2} \tag{9}$$

where I_z^2, $I_\emptyset^2$ and I_r^2 are the wave intensities in the axial, angular and radial directions, respectively. These components are determined by taking the dot product of the particle velocity and the pressure at each point in the domain:

$$I_z = 0.5\left(p.(-\frac{\frac{dp}{dz}}{(\rho_c \times i\omega)})\right), I_\emptyset = 0.5\left(p.(-\frac{\frac{dp}{d\emptyset}}{(\rho_c \times i\omega)})\right), I_r = 0.5\left(p.(-\frac{\frac{dp}{dr}}{(\rho_c \times i\omega)})\right) \tag{10}$$

where ω is the angular frequency, i is the imaginary number and $\frac{dp}{dr}$ is the pressure gradient with respect to the r.

Attenuation is the combined effect of absorption and scattering. In other words, it is the decay rate of the acoustic wave as it passes through the medium. Attenuation may be classified according to its source to attenuation due to grain scattering and attenuation due to absorption [91]. Acoustic attenuation is temperature and frequency dependent and is approximately characterized by the following equation [92], [93]:

$$\alpha = \alpha_{cte} f^n \tag{11}$$

where α_{cte} represents the attenuation constant coefficient for the material. Table 3.1 provides the material properties in the model simulation.

Table 3-1 Material properties

Material	**Density (kg/m^3)**	**Speed of sound (m/s)**	**Attenuation (Np/m) @ 2.15 MHz** [94]	**Specific heat (j/(kg.k))**	**Thermal conductivity (W/(m.k))**
Water (at 293.7 K)	998	1483.16	0.115	4150	0.60
Cured PDMS(10:1)	1028	1055	76.09	1550	0.16
LDPE	913	1950	5.10	2100	0.33
ABS	968	2250	23.20	1420	0.17
Polystyrene	1051	2450	3.82	1400	0.15
Acrylic	1190	2750	13.62	1470	0.18

3.5. Ultrasound and heat transfer mesh

Free triangular mesh is generated for heat transfer and acoustic pressure. The generated mesh for the acoustic model must be significantly fine in order to resolve different phases of the pressure waves created by the ultrasound transducer. Therefore, the maximum element size is set to one third of the wavelength of the waves. A coarser mesh with a maximum size of 5 mm is set for the heat transfer model with a finer mesh which is one- eighth of the wavenumber in the focal region.

3.6. Results

In this section, the effects of different parameters that can affect the printing time and resolution are investigated. First, results for a working frequency of 2.15 MHz and a power of 218 W are presented. Then, the influence of frequency, power, divider and resin material are studied. The resolution of the 3D printer is primarily dictated by the size of the focal region.

3.6.1. Acoustic and thermal fields at the frequency of 2.15 MHz and the power of 218 W

In this section the ultrasound beam only passes in water at a frequency of 2.15 MHz and a power of 218 W, at room temperature; T=21 °C. The results of the simulation for the acoustic field are illustrated in Figure 3.4. Maximum acoustic pressure of 29.5 MPa is achieved at the focal point due to the waves converging at this power. In addition, the acoustic pressure amplitude reaches 37.1 MPa at a frequency of 2 MHz and an input power of 400 W. This pressure is in good agreement with pressure focus of the transducer's datasheet which is 37.21 MPa. Minimal acoustic pressure changes is shown at the rest of the media.

The acoustic intensity magnitude in the water domain is presented in Figure 3.4 (b). This plot demonstrates an oval shape which is about 5.27 mm long and 0.70 mm wide with high intensity which leads to an elevation of the temperature at this region. In this plot, acoustic energy distribution is clearly shown.

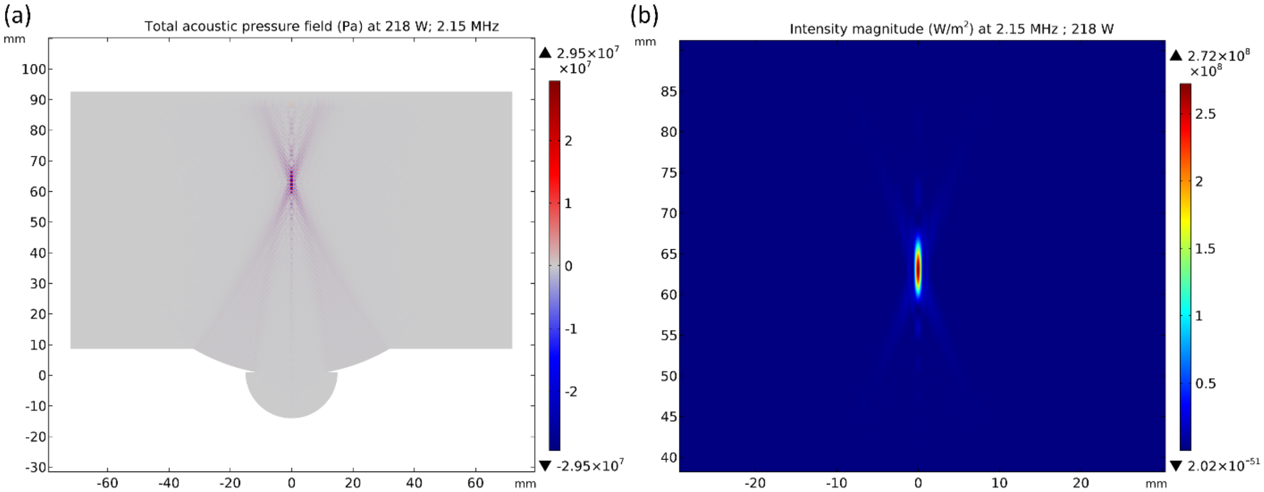

Figure 3-4 Acoustic field in presence of water. (a) pressure field; (b) intensity field

The acoustic pressure amplitude profile along the *z*-axis ($r = 0$) is illustrated in Figure 3.5 (a). According to the plot, the exact location of the acoustic focus is 54.5 mm away from the surface of the transducer. A depiction of the pressure amplitude profile along the radial direction in the focal plane is given in Figure 3.5 (b).

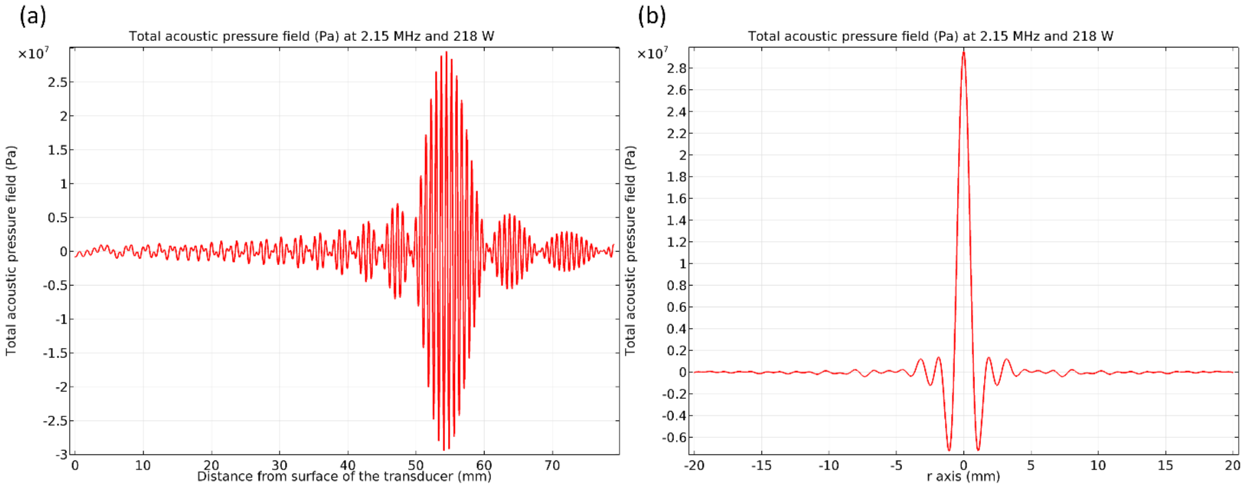

Figure 3-5 (a) acoustic pressure amplitude profile along the z-axis; (b) acoustic pressure amplitude profile along the radial direction in the focal point;

We are interested in minimizing any temperature rise in the area surrounding the focal region. Temperature rise in a larger region leads to a decrease in the resolution of the printed part. The heat induced by the acoustic field after 1 second insonation in presence of water is shown in Figure 3.6.

Temperature rise contours can be seen in Figure 3.6 (a) for the frequency of 2.15 MHz at t= 1s. As it is shown in the plot, the maximum temperature rise is 6 °C. The oval-shaped heated spot and the acoustic focal area are about the same size, which is clearly presented in the contour plot of the temperature in Figure 3.6 (a). In addition, this plot shows a minimal temperature rise in the non-focal region.

Figure 3.6 (b) provides the temperature profile at the focal point with respect to time for a focal pressure amplitude of 29.5 MPa. According to the aforementioned figure, there is a sharp rise in temperature during the insonation. It also gives valuable information about the cooling process after the acoustic source is turned off. The difference between temperature at focus point and 0.5 mm off the acoustic focal is 3.2 °C. A pulse of ultrasound emitted from the transducer is determined as a peak in temperature.

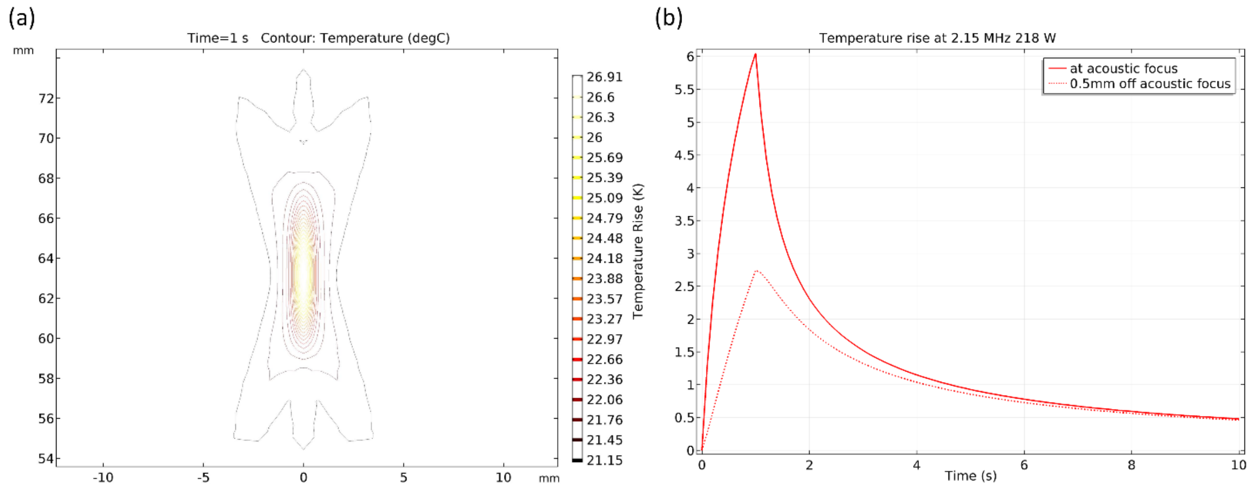

Figure 3-6 Thermal field in presence of water. (a) Contour plot of the temperature rise after 1 second of insonation; (b) heating and cooling curves at acoustic focus and 0.5 mm off-axis in the focal plane;

These results indicate that the temperature profile is dependent on the acoustic intensity profile. Normalized intensity and temperature profile along the radial axis is illustrated in Figure 3.7. Due to the smoothing effect of the thermal conduction, intensity profile converts to a smooth temperature response.

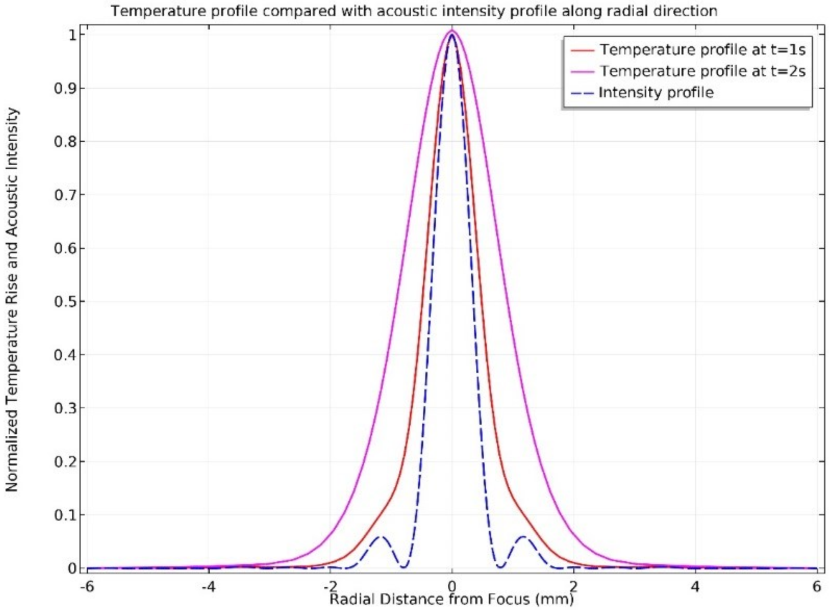

Figure 3-7 Normalized temperature and intensity profile

3.6.2. Effect of frequency on pressure and thermal fields

This section discusses the influence of frequency on the printing process. Frequency is a key factor that can significantly affect the printing resolution and printing time. However, frequency has a number of limitations. The major limitation of this parameter is dependent on the transducer. Transducer actuates at its natural frequency which results in a limitation in the frequency range. However, frequency can vary in the range of 1.6 MHz to 3MHz. In addition, the output of the pulse generator is dependent on frequency. Consequently, higher frequencies lead to lower power output. All simulations in this section are performed in a power of 218 W at water.

Figure 3.8 (a) presents the intensity field with respect to the distance to the surface of the transducer in presence of water for frequencies of 0.4, 1, 1.6, 2, 2.6 and 3 MHz. It is needed to be taken into account that attenuation coefficient is variable as a function of frequency and temperature. In this work, the attenuation coefficient is determined by the formula reported by Krautkramer [95]. Equation 13 defines attenuation coefficient as a function of frequency (Hz).

$$\alpha = 2.17 \times 10^{-15} f^2 (dB/cm) \qquad (13)$$

Also, the absorption coefficient of water as a function of temperature, PH, salinity and frequency is reported [96], [97].

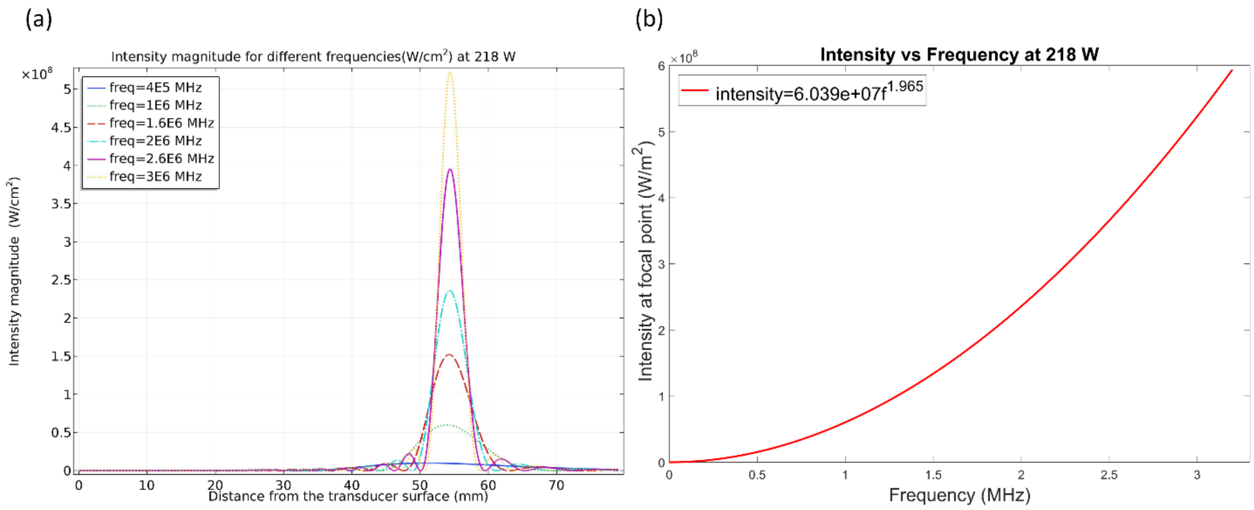

Figure 3-8 (a) intensity profile along the z-axis for different frequencies; (b) intensity as a function of frequency.

From the graphs, we can see that the focal length is reduced by increasing the frequency. Therefore, better printing resolution can be achieved by increasing the frequency.

The correlation between frequency and acoustic field is investigated in Figure 3.8 (b). As shown in this figure the intensity is significantly increased by increasing frequency. A power curve is fitted to the result for frequencies between 0 to 3.2 MHz versus the maximum intensity. This function can be used to predict the intensity at the focal region according to the frequency. The maximum intensity is 6 kW/cm^2 at a frequency of 1 MHz and 23.9 kW/ cm^2 at a frequency of 2 MHz. These results indicated that, resin curing can be controlled by altering the frequency.

In addition, the spot size is related to frequency; more specifically smaller spot size can be achieved by using higher frequencies. Spot size or focal size plays an important role in printing resolution. Knowledge of the beam width and focal length is necessary to determine whether the spot size is appropriate to print a part or not. Resolution of printing can be enhanced by decreasing the spot size. For instance, parts of a model which need higher accuracies can be printed by higher frequencies and for parts which don't require high resolutions such as supports, lower resolutions can be applied.

The focal width and the focal length as a function of frequency are illustrated in Figure 3.9 (a) and Figure 3.9 (b). The focal width and the beam diameter for the frequency of 2 MHz are 0.76 mm and 5.72 mm, respectively.

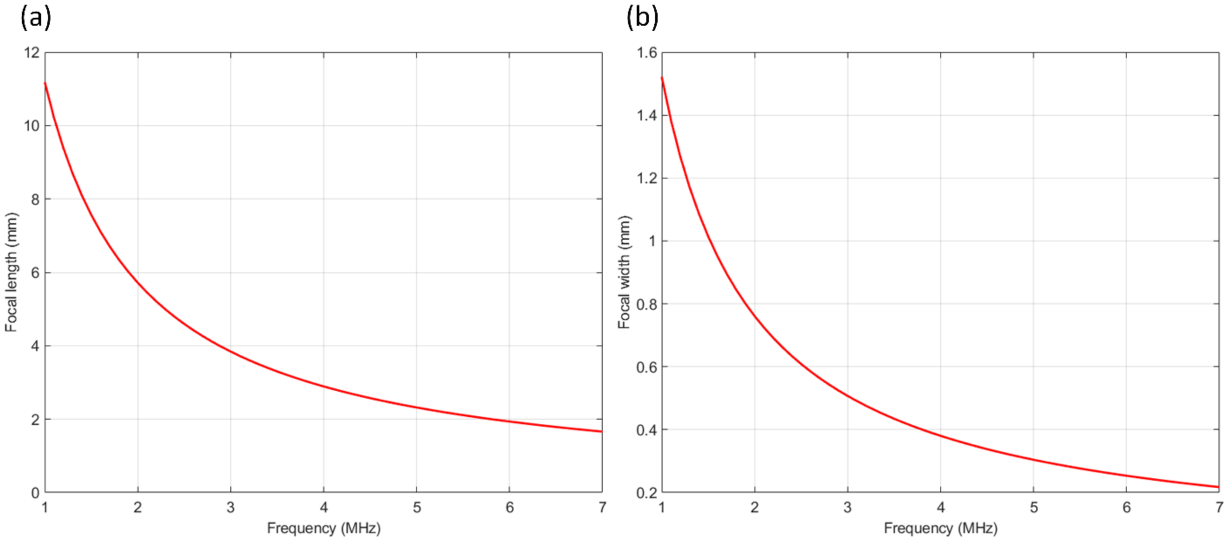

Figure 3-9 Focal length (a) and focal width (b) as a function of frequency

In order to print a microfluidic channel, the focal width and length are taken into account to achieve the desired design. The beam diameter has significant effects on the channel width, while the focal length has an impact on the channel height.

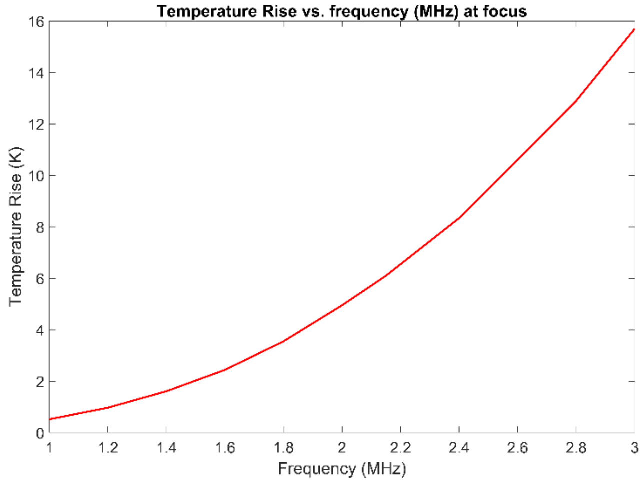

Figure 3-10 Temperature rise at the focus as a function of frequency

Figure 3.10 shows the temperature rise after 1 second of insonation for different frequencies. Higher temperature rise can be achieved with higher frequencies. Consequently, printing can be accelerated by higher frequencies.

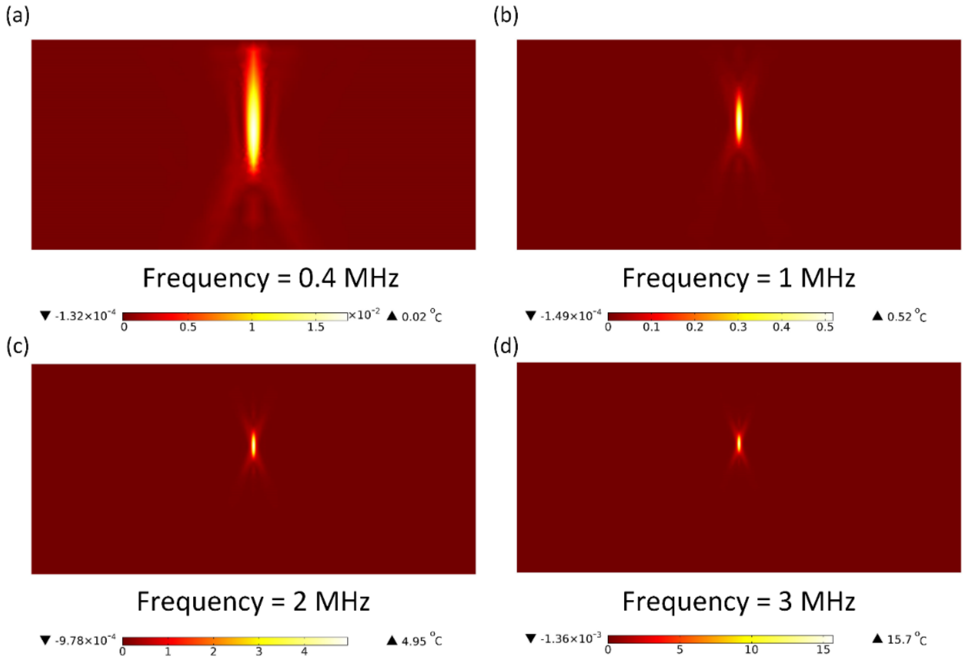

Figure 3-11 Surface plot of the temperature rise in presence of water after 1 second of insonation for frequencies of: (a) 0.4 MHz; (b) 1 MHz; (c) 2 MHz; (d) 3 MHz.

The results of the temperature rise field in presence of water after one second of insonation for frequencies of 0.4, 1, 2 and 3 MHz are shown in Figure 3.11 (a-d). Results reveal the importance of selecting a proper transducer with a small focal size. Furthermore, it provides valuable information about the effect of frequency in the resolution.

3.6.3. Effect of power on pressure and thermal fields

In this section, the effect of power on the printing process is studied. The input power plays a critical role in 3D printing process. Despite the limited range of input frequencies, the input power for the transducer can be variable between 1 W to 218 W. As a result, more flexibility could be reached using this parameter. On the other hand, deposit energy rate at a constant federate can be altered by the input power. In addition, unlike attenuation which is variable for various frequencies, attenuation for different powers is constant which makes it a pivotal parameter in the process.

The result obtained from the simulation in presence of water at a frequency of 2.15 MHz are set out in Figure 3.12 and Figure 3.13. The maximum intensity for power of 218 W, 158 W and 68 W are 27.2 kW/cm^2,19.7 kW/cm^2, and 8.47 kW/cm^2. As shown in Figure 3.12 (b), the correlation between power and the intensity is linear which makes it accessible to control.

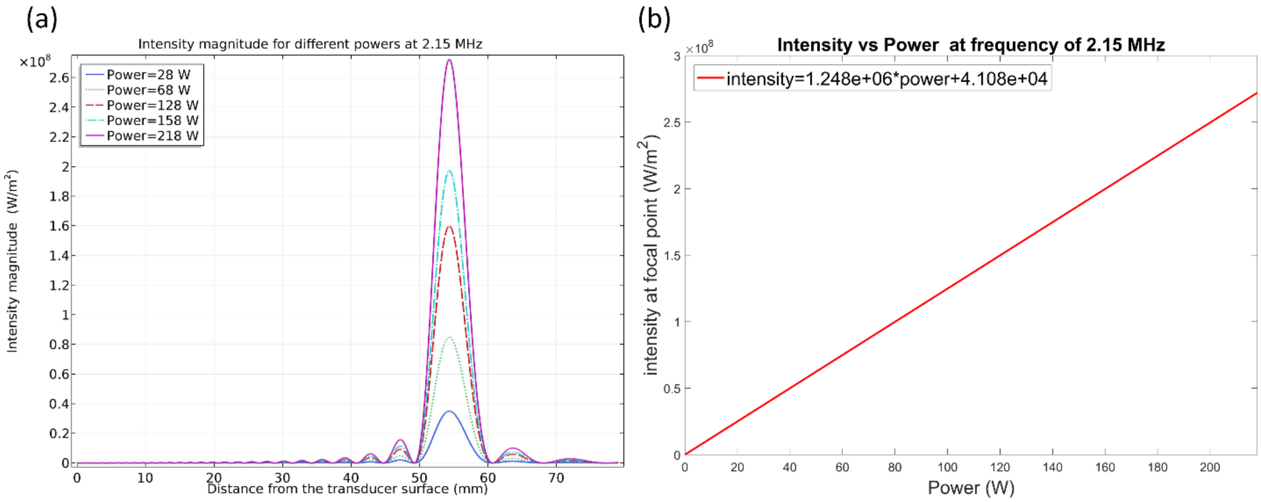

Figure 3-12 Maximum intensity at the focus point for various powers

In addition, power does not have an impact on the focal size. Focal size has a significant impact on the resolution of a printed part.

Figure 3.13 presents the temperature rise after 1 second of sonication for different powers. It is apparent from this graph that the temperature rise is changed linearly by power.

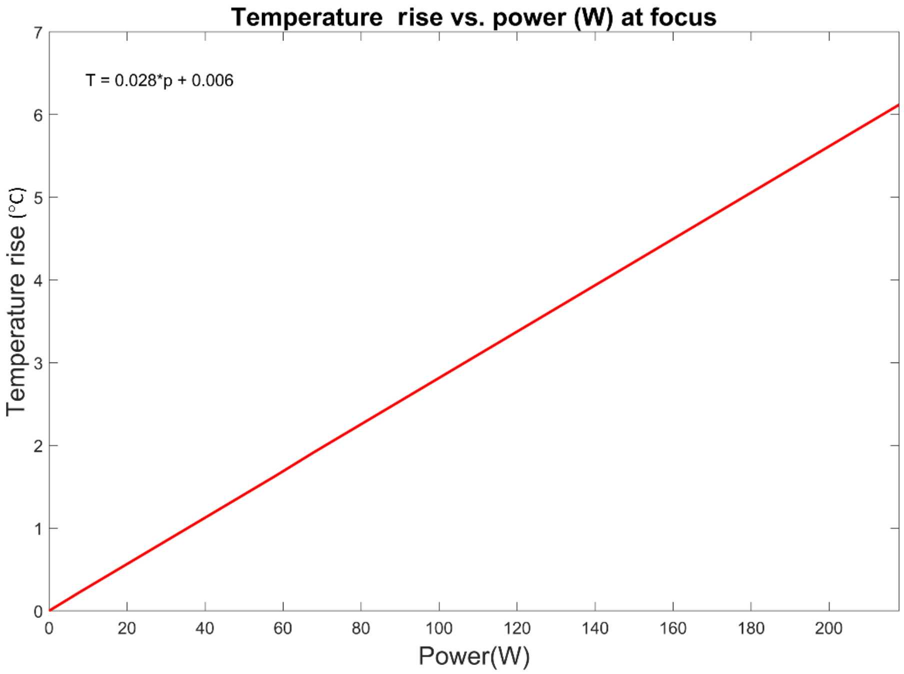

Figure 3-13 Temperature rise after 1s of sonication for different input powers

Since curing time is correlated to the temperature rise, different powers can be used for different part of the model. For instance, lower power is suggested for channel edges and higher power can be used for other parts of the model to decrease the printing time.

3.6.4. Effect of the divider material on the pressure field

The resin container is separated from the water container by a divider. Properties of the divider such as acoustic impedance, attenuation and thickness are considerable factors in designing the resin box. Therefore, having a proper model to predict these factors is essential to eliminate acoustic loss through the divider. Simulation at a frequency of 2.15 MHz and a power of 218 W in presence of water for three materials were achieved by COMSOL and presented in Figure 3.14 and Figure 3.15. The divider was placed 42 mm far away from the surface of the transducer.

As Figure 3.14 (a) shows, there is a remarkable difference in maximum acoustic intensities of different materials. The maximum acoustic intensity for 3 mm plates is 24.7 kW/cm^2, 18.1 kW/cm^2 and 18.2 kW/cm^2 for Low-density polyethylene (LDPE), polystyrene and ABS sheets, respectively as illustrated in Figure 3.14 (a). Since acoustic impedance of LDPE (1.79 kgm^{-2}s$^-$

$^{1}\times10^{6}$) is close to water's (1.48 $\text{kgm}^{-2}\text{s}^{-1}\times10^{6}$), most of the energy is transmitted through the divider and lower loss is observed. Also, another intensity peak is observed especially for the polystyrene plate where waves were transmitted through the plate. These results indicate that LDPE plate is the best material that can be used as a divider. However, due to the low melting point of LDPE (48 °C) and its improper surface roughness, it cannot be used in high temperatures and this makes other materials an option for consideration. Polystyrene is a suitable material due to its low roughness and transparency.

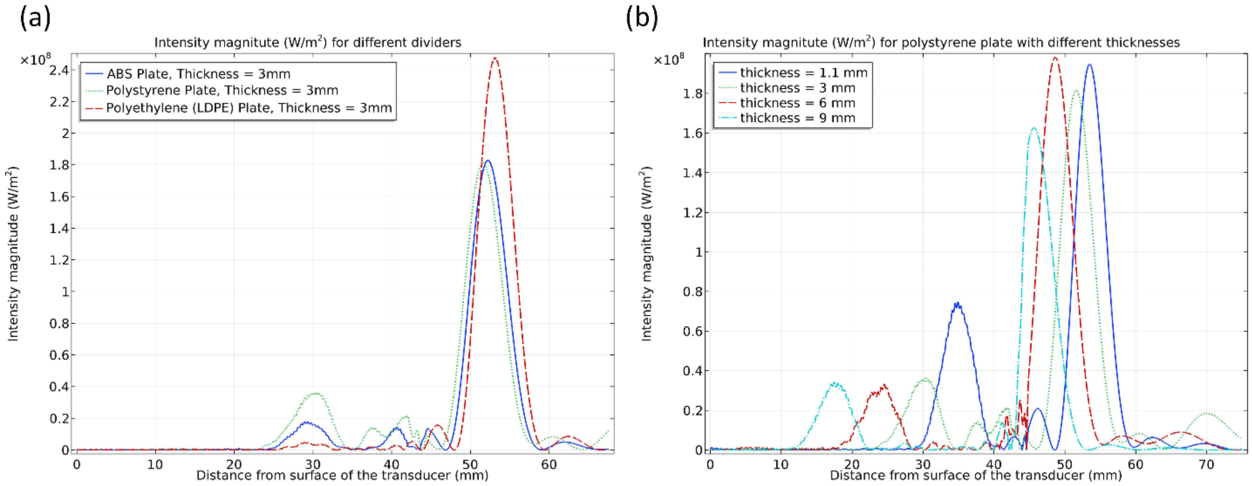

Figure 3-14 Acoustic field in presence of water and the divider. Intensity profile: (a) different divider materials; (b) polystyrene dividers with various thicknesses

In Figure 3.14 (b), acoustic field for a polystyrene plate with a variety of thicknesses of 1.1, 3, 6 and 9 mm is presented. The acoustic attenuation of the polystyrene plate is 3.82 Np/m at a frequency of 2.15 MHz.

As it is illustrated in the figure the acoustic intensity is not only dependent on the divider thickness but also to the higher acoustic attenuation in the solid material. Since the speed of sound is higher in solid materials focal region gets closer to the transducer due to the refraction of ultrasound waves. This graph reveals that, the divider thickness and the material acoustic attenuation need to be considered as crucial factors during the design of the resin container.

In addition, acoustic intensity is reduced by increasing the attenuation of the plate and maximum intensity decreases exponentially by increasing the attenuation of the plate. Therefore, a plate with lower attenuation should be chosen as the divider to achieve the maximum intensity and pressure in the focal region.

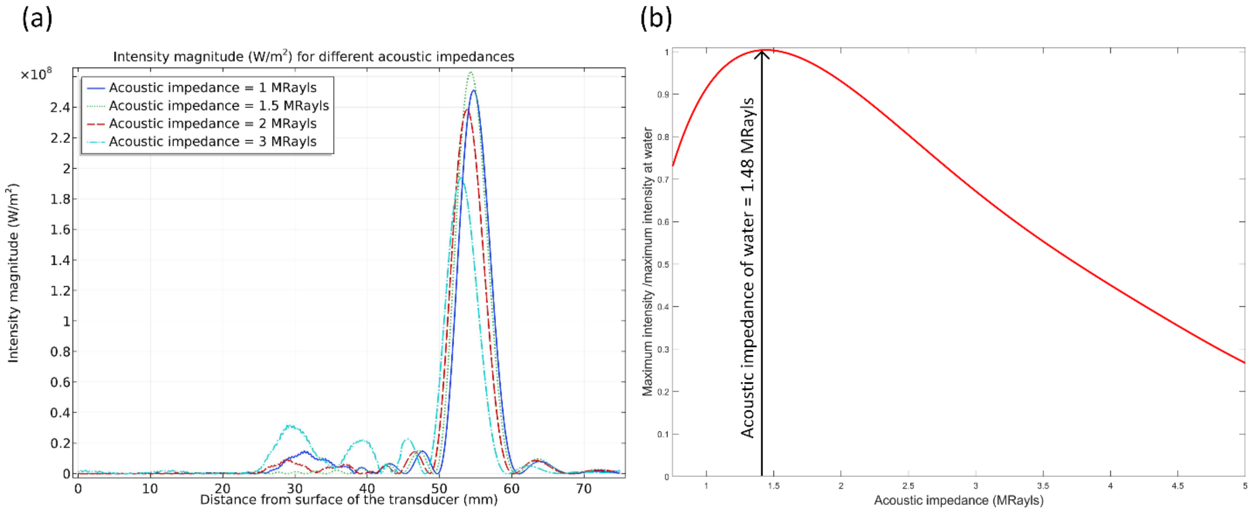

Figure 3-15 Acoustic field in presence of water and the divider. (a) different acoustic impedances; (b) maximum intensity versus acoustic impedance.

The effect of divider acoustic impedance on acoustic field at a frequency of 2.15 MHz is investigated in Figure 3.15. As can be seen from Figure 3.15 (b), the maximum intensity is achieved at the acoustic impedance of 1.48 MRayls which is the acoustic impedance of water. In addition, the focal region gets closer to the divider for material with higher acoustic impedance due to the refraction of sound waves through the divider which is in agreement with Snell's law. The distance of the focal point from the surface of the transducer for acoustic impedances of 1, 1.5, 2 and 3 MRayls is 54.8 mm, 54.4 mm, 53.8 mm and 53 mm, respectively. These results suggest that plates with an acoustic impedance close to water's should be chosen as the divider to minimize the loss.

3.6.5. Effect of resin material on acoustic and thermal fields

In order to achieve a reasonable printing resolution, we need to choose a thermoset polymer with acoustic and thermal properties that reduce the focal region size and printing time while increasing the intensity. Here, a simulation for PDMS resin with a variety of acoustic attenuations is presented. However, since attenuations of resin systems during the curing process were not reported, we assumed PDMS with variable attenuations between 0.1 Np/m to 70 Np/m. Since most of the reported attenuations for resin are in this range.

Despite PDMS resin system, acoustic attenuation during the curing process has been mentioned for other materials such as Epon 815c and polyester resin in different frequencies [98],

[99]. According to these papers, attenuation of the resin system alters during the curing process and reaches a significantly higher attenuation during the curing process. However, the attenuation is changed less than 10% for a cured part compared to an uncured part. Also, attenuation for cured PDMS and EPON 828 at different frequencies has been reported [100], [101].

Results for the acoustic intensity profile along the z-axis at a frequency of 2.15 MHz is shown in Figure 3.16. In this simulation, a polystyrene petri dish with a thickness of 1.1 mm is considered as the resin container which mimics the experimental setup. From the graph, it can be seen that the greatest intensity is associated with the smallest absorption coefficient. Additionally, the focal point location is not dependent on the attenuation coefficient.

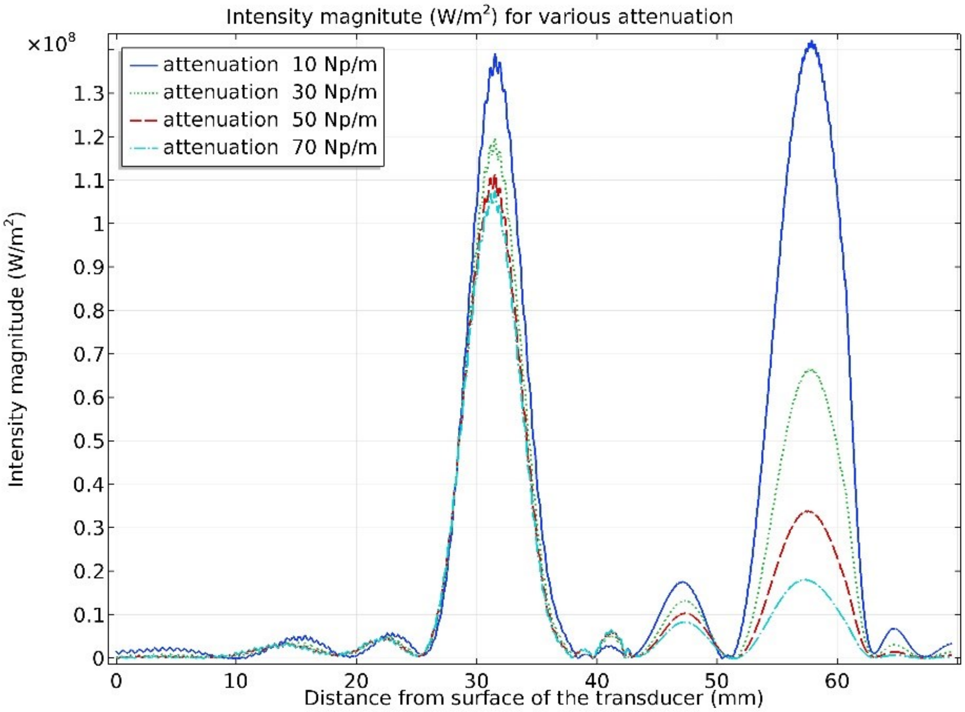

Figure 3-16 Acoustic intensity profile along the z-axis for different attenuations

A significant reduction compared to Figure 3.14 (b) was found in the maximum intensity. A comparison of the two figures reveals the importance of choosing materials with low attenuation in order to reach a sufficient resolution. Taken together, attenuation coefficient plays a key role in the curing process and makes it essential to find a resin system with proper absorption coefficient.

The attenuation coefficient is a critical parameter because this parameter is present in the source term of heat transfer equation. Here, the sensitivity of the absorption coefficient of the resin was checked and it was concluded that the temperature rise is remarkably sensitive to the absorption coefficient. A parametric sweep was carried out to analyze the temperature rise after 1 second of sonication against the various attenuations coefficients.

Temperature rise as a function of attenuation is presented in Figure 3.17. This figure is quite revealing in several ways. Highest temperature rise is observed for an attenuation of 30 Np/m. A possible explanation for this result may be due to having a model with multiple materials such as acrylic, polystyrene, water, and PDMS with different acoustic and thermal properties. It seems that the result is highly dependent on the geometry and the material. For instance, the volume of the petri dish may affect the temperature increase since the thermal conductivities of the materials are not same. In addition, acoustic waves cannot pass through the petri dish for higher attenuations as it is shown in Figure 3.16. Therefore, after a certain attenuation, temperature rise decreases and most of acoustic waves are absorbed.

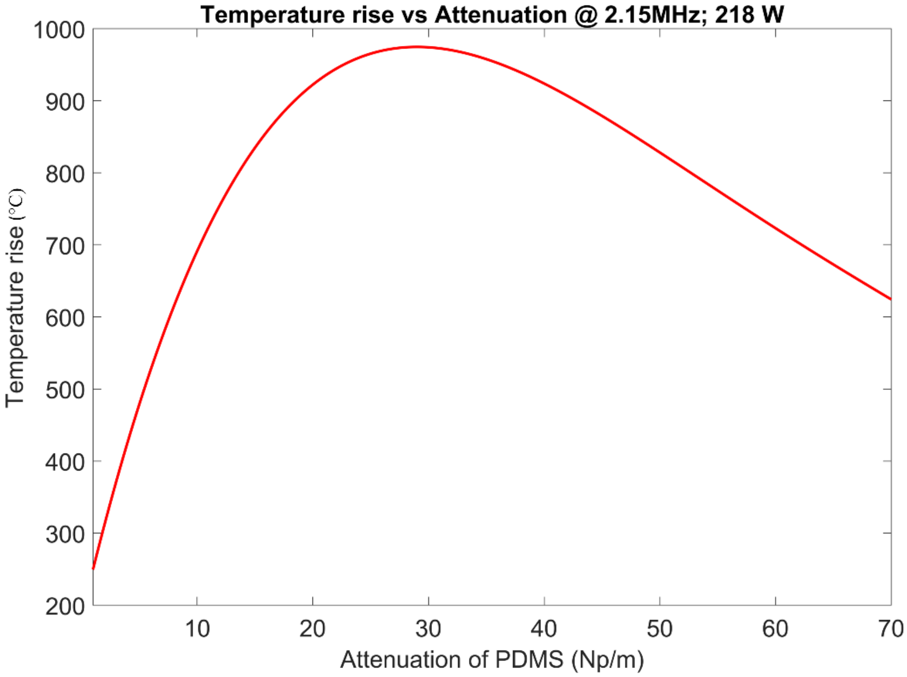

Figure 3-17 Temperature rise in the focus point as a function of absorption coefficient

Temperature field at the resin tank is depicted in Figures 3.18 (b) for attenuation of 1, 30, 50, 70 Np/m. Temperature rise at t=1 for these values are 218 °C, 973 °C, 829 °C and 623 °C, respectively. It is apparent from these data, highest temperature occurs in the acrylic plate for an attenuation of 1 Np/m. The reason behind this is the higher acoustic attenuation for acrylic.

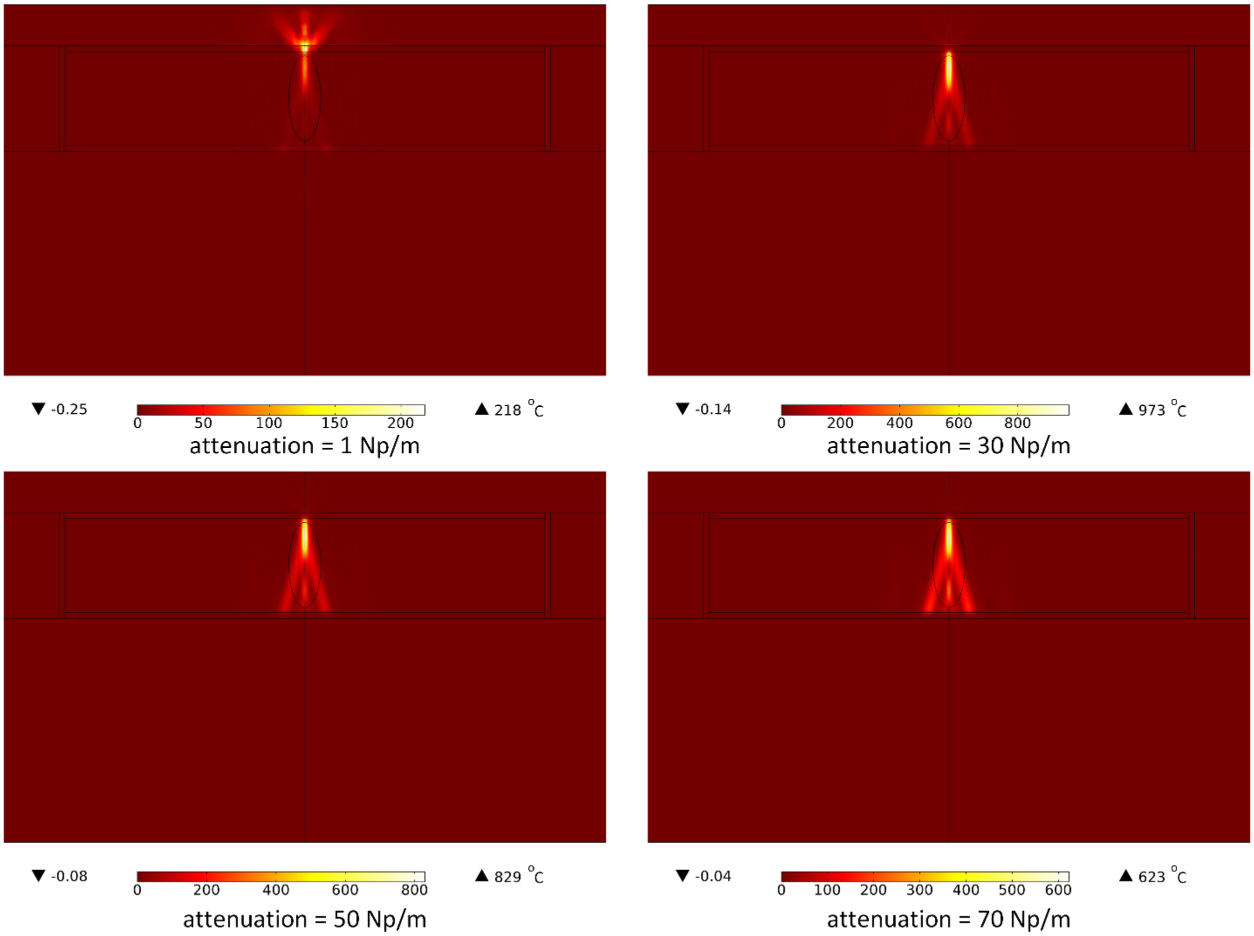

Figure 3-18 Surface plot of temperature rise in the petri dish for various attenuations in the petri dish.

These results reveal that temperature release is not only dependent on the intensity profile. It is also highly dependent on thermal and acoustic properties of the material. The temperature increment in the petri dish needs to be contorted. In order to control the temperature at the petri dish, it can be surrounded with a thermoelectric cooler.

The results of this study indicate that, determining the attenuation of the resin during the curing process is crucial. This parameter has an impact on the total deposition energy in the resin container and consequently curing the resin and printing the part.

3.7. Conclusions

In this chapter, acoustic pressure and heat transfer in the domain set out to study the impacts of different parameters on printing time and resolution. The model provides a good understanding and estimation of acoustic field, temperature increase, focal region size and curing time for the focal pressure. The result shows the temperature rise is not necessarily proportional to the acoustic intensity. The sensitivity of the system to acoustic impedance, frequency, power and acoustic absorption were investigated, and was found that these factors had a considerable effect on temperature rise. Totally, the simulation reveals that the temperature rise depends on acoustic and thermal properties of the material, as well as to the power and frequency of the transducer. These models give us a valuable understanding of the phenomena and can be used prior to the experiment. Also, it can be implemented to model the response of the system to different pulse shapes and duration times. In the next chapter, the limitations and the accuracy of using 3D printed molds for microfluidic applications with a commercial stereolothography 3D printer will be discussed to evaluate current state of 3D printers for using in microfluidic applications.

Chapter 4

4. 3D printed molds for non-planar PDMS microfluidic channels

4.1. Introduction

In this chapter, the limitations and the accuracy of using 3D printed templates for microfluidic applications with commercial stereolithography (SLA) and Fused Deposition Modelling (FDM) 3D printers, are presented. The application of channels with multiple thicknesses is a major area of interest within fields of tissue engineering and microfluidics. 3D printing facilitates cost-effective fabrication of PDMS-based microfluidics using 3D printed molds. Due to the low resolution of 3D printers for microfluidic applications, direct printing of high-resolution microfluidic devices is limited.

The main aim of this chapter is characterization and evaluation of 3D printed molds for microfluidic applications and comparison of materials and printing configurations. Therefore, three different platforms containing multiple thicknesses were fabricated using 3D printed molds. The accuracy of printed parts in three dimensions will be demonstrated and the limitations and applications of these molds will be studied.

4.2. Experiment and measurement

Stereolithography (SLA) and fused deposition modeling (FDM) methods were used in this work, to investigate the feasibility of each method for microfluidic applications. SLA is an additive manufacturing method that converts photopolymer materials into solid parts by curing them using an ultraviolet (UV) laser. FDM is a thermoplastic filament technology which deposits a thermoplastic material through an extruder, layer by layer. In FDM printers, the resolution is a factor of the nozzle size and the positioner. In contrast, SLA printers' resolution is dictated by radial beam scattering [102].

4.2.1. 3D printing of the mold

The CAD models of the devices were designed using Solidworks (Dassault Systèmes) and the designed models were exported as STL files. The models were printed using Formlabs 2 and LulzBot TAZ 6 which are SLA and FDM 3D printers, respectively. Two different types of stereolithography resin were tested. The resolution of the 3D printer according to its datasheet is

150 μm in the XY plane and 25 μm in the Z axis. In addition, the clear filament (NGEN clear, colorFabb Inc.) was used for the FDM 3D printer and the default setting on the 3D printer was applied. A thickness of 2 mm was considered for the base to prevent models from bending.

4.2.2. Post-processing of 3D printed molds

The 3D printed molds by the SLA 3D printer were washed with isopropanol for 2 minutes after printing, nitrogen gas then was used to dry them. For the next step, they were exposed to UV light (Stratalinker® UV Crosslinker 2400) for 6 min. The molds' roughness and accuracy were inspected using confocal microscopy. Since PDMS cannot be polymerized into a cured part in contact with the surface of the molds, they are treated with oxygen plasma at high power (Harrick Plasma, Inc.) before molding for 2 min and then the parts are coated with fluorinated silane (Trichlorosilane, Sigma-Aldrich, Inc.) for 6 hours at 60 °C. Consequently, the cured parts will be removed easily from the master mold and the surface will not be sticky [103].

4.2.3. Fabrication of microfluidic devices

PDMS components were purchased from Dow Corning Crop (USA). Mixed polymer at 10:1 ratio (w/w) was degassed in a vacuum chamber for 30 min prior to casting. Then, the polymer was poured into the master mold. The PDMS was cured in an oven at 70 °C in 4 hours. Afterward, the PDMS part was peeled off from the mold and cleaned with IPA. The required holes for fluid inlet and outlet were made prior to plasma treating and thereafter, a glass slide and the PDMS part were treated with oxygen plasma for 50 sec and were bonded to each other.

4.2.4. Characterization of surface topography

Surface profile was obtained by using a Confocal Laser Scanning Microscope (Olympus Inc.). In contrast to SEM, there is no need to prepare the part with a conductive coat. 5x and 20x lenses were used for confocal microscopy. The cutoff value (λ_c), is set to 0.8 mm. Area of 2.4 mm by 1.2 mm was scanned with the ultrafine setting. The scanning of this area takes 60 min. The surface roughness, height profile, and geometry were analyzed and 2D and 3D images were exported by the microscope software for future analysis.

4.3. Results and discussion

3D printing enables fabrication of microfluidic chips with multiple thicknesses. In contrast to photolithography method, multiple masks and alignments are not required. As the result, CAD models can be printed simply which make them ideal for fast prototyping.

A comparison of surface roughnesses, printing costs and times of a 2 cm × 5 cm × 2mm template for two different methods are presented in Table 4.1.

Table 4-1 Comparison of printing cost and time for different resins

Resin type	Cost/ Part	Printing time	Surface roughness [µm]
Clear; printed directly on the build platform	0.30 US	114 min	1.12
Clear; printed with supports	0.44 US	172 min	2.24
Flexible; printed directly on the build platform	0.40 US	113 min	0.43
Flexible Printed with supports	0.62 US	200 min	2.53
NGEN Clear Filament	0.05 US	21 min	7.61

Printing cost and time for the FDM 3D printer is considerably lower. However, these factors are inadequate to make it a reasonable method for microfluidic devices due to the printer's low resolution. Printing time for clear and flexible resin is almost the same. However, the flexible resin's printing cost is slightly higher than clear resin's.

More time is required if the model is being printed perpendicular to the build platform, since it includes more layers for printing. Basically, printing time is highly dependent on number of layers. Therefore, printing on the build platform is more time-saving. In addition, printing cost for models directly printed on the build platform is lower due to the volume of supports and hence the presence of more layers. Laser microscopy images of the surface of the models printed with flexible and clear resin by two different configurations are illustrated in Figure 4.2.

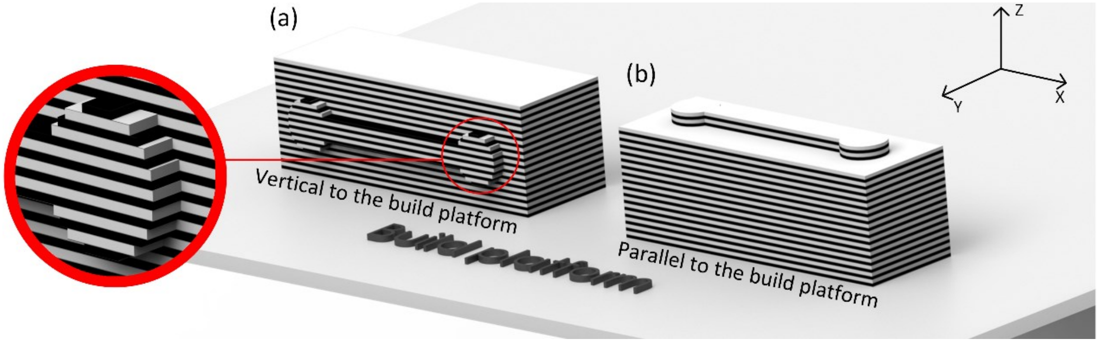

Figure 4-1 Printing on the build platform; printing layers are illustrated by black and white strips

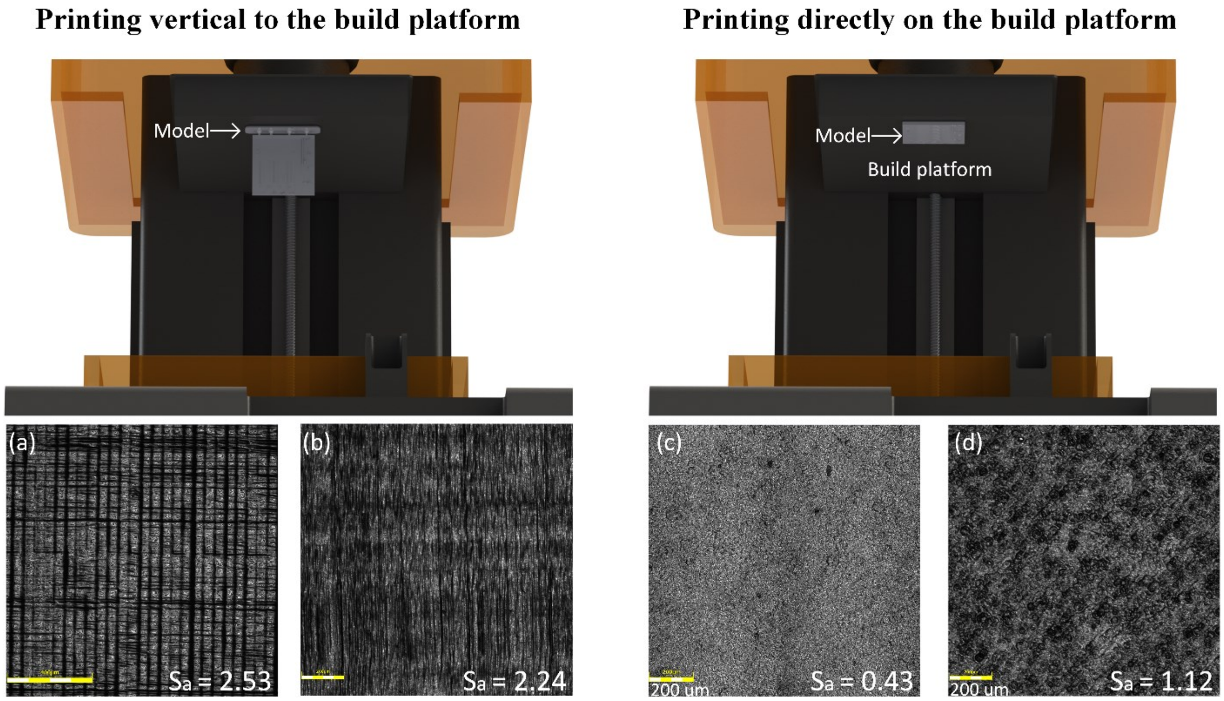

Printing vertical to the build platform

Printing directly on the build platform

Figure 4-2 Surface comparison of two models; model printed vertically; (a) flexible resin (b) clear resin; model printed directly on the platform; (c) flexible resin (d) clear resin.

The surface of the mold in the model printed horizontally is significantly smoother since the model surface is exposed to the UV light in a specific layer. In comparison to the model printed perpendicular to the build platform, distinctive layers are not apparent on the surface of the parts as it is demonstrated in Figure 4.1 and Figure 4.2.

Surface roughness was measured by the confocal microscope and the cutoff value was set to 0.8 mm. The average roughness was 1.12 µm, 0.43 µm, and 7.61 µm for clear resin, flexible resin, and FDM filament, respectively; all printed directly on the build platform. The surface roughness of flexible resin was 3 times better than clear resin. Therefore, fabricated channels with this resin are smoother and comparable to lithography.

It shows that SLA 3D printers are more suitable for microfluidic applications. Since flexible resin is not transparent, UV light cannot pass through the flexible cured parts. By contrast, clear resin is transparent and UV light can penetrate to that. Therefore, the resolution for the flexible resin on the plane perpendicular to the build platform is better than the clear resin.

4.3.1. 3D microfluidic channel

Several molds were fabricated and pretreated for a 3D microfluidic channel using FDM and SLA printers. These models were printed directly on the build platform due to the better surface roughness of this configuration. Models contain 31 rods on a channel with a cross-section of 1000 × 100 μm^2. The diameter and the height of the rods are 200 μm and 60 μm, respectively (Figure. 4.3 (c-e)). The required printing time to print directly on the build platform is 113 min and 21 min for SLA 3D printer and FDM 3D printer, respectively. This design can be used to monitor cell culturing in the microfluidic channel. Since most of cells stick to rods due to their larger surface area, the effects of the environment such as light and temperature to cell culturing can be studied by using this design.

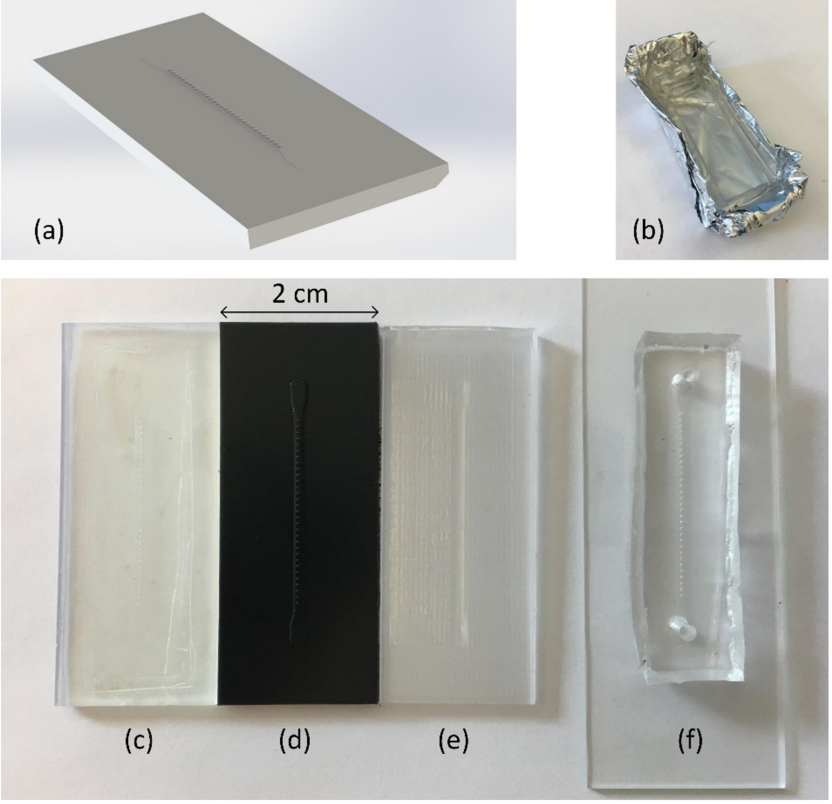

Figure 4-3 Rapid prototyping PDMS-based microfluidic device by 3D printed mold. (a) Design of a microfluidic channel (b) The reusable mold for fabrication of PDMS-based microfluidic device fabricated by clear resin. 3D printed molds by clear resin (c), flexible resin (d) and FDM filament (e). (f) Picture of the fabricated microfluidic device is depicted.

The FDM 3D printer could not construct the rods on the channel. In addition, the surface roughness and channel profile are inadequate for microfluidic devices. The result obtained from the microscope for parts printed with SLA 3D printer is illustrated in Figure 4.4. The resolution of clear resin is better than flexible resin on the plane parallel to the build platform. As it is presented in Figure 4.5 shows both types of resin have a considerable error in the depth of the channel compared to the CAD model.

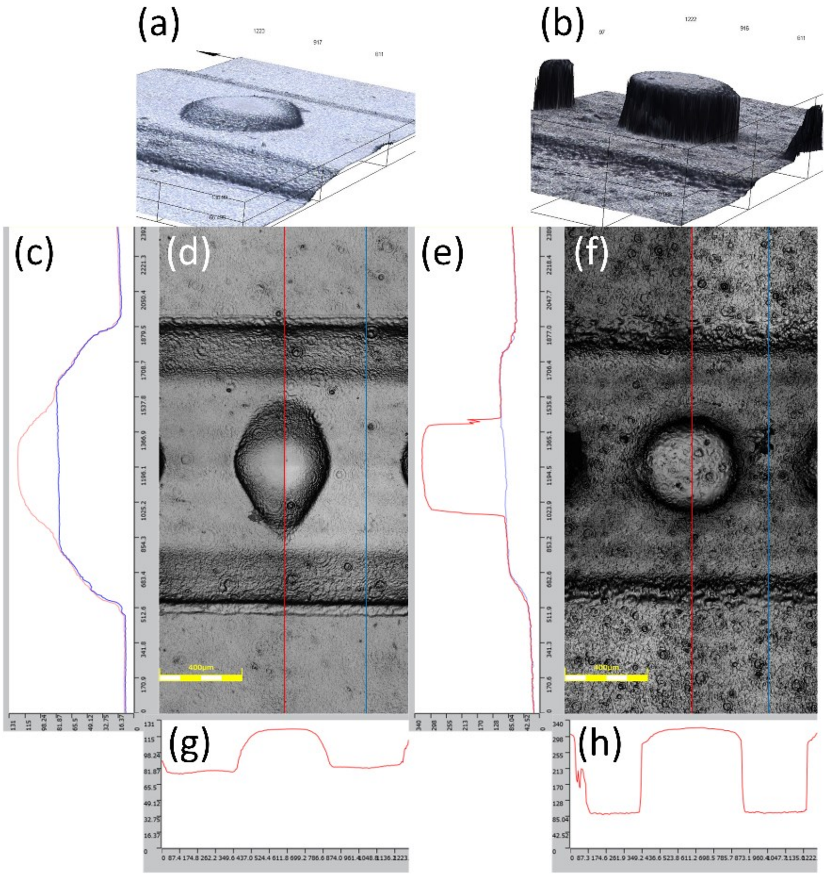

Figure 4-4 Laser scanning microscopic images of 3D printed molds in flexible resin (left) and clear resin (right) .3D scanning of the 3D printed mold by flexible resin (a) and clear resin (b). (c&e) The height profile of the channel by line scanning microscopy. The blue line shows the height of the channel in the 2D scanned image and the red line shows the height of the channel in presence of a rod in the red line in the 2D scanned image. (d) and (f) present the surface of the mold. (g) and (h) show the height and the profile of the rod.

It is apparent from this figure that rods have a circular shape compared to the flexible resin which has an elliptical shape (Figure 4.4 (g) and Figure 4.4 (h)). Furthermore, the height profile increases gradually in the flexible mold compared to the clear mold in which the height profile is comparable to the designed model. Clear molds tend to bend in presence of heat which results in a curved PDMS chip. In molds printed with flexible resin, this would not be a concern due to their flexibility.

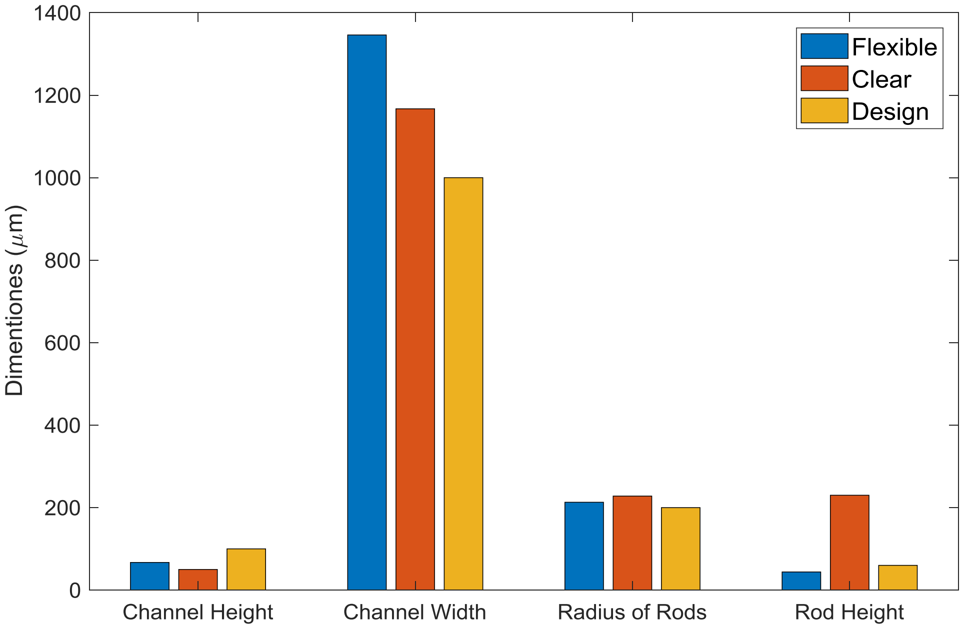

Figure 4-5 Comparison of the designed model and the printed mold with different resins. The yellow bar represents the design dimensions.

Figure 4.5 compares the dimensions measured with the confocal microscopy and the designed mold. Comparing the two results, it can be seen that the rod's radius has an acceptable error of less than 15% for both resins. However, the shape of a rod with the clear resin has a smaller deviation from the circular shape of the designed mold. As Figure 4.5 shows, there is a significant difference between the designed and the printed parts in the Z direction. A considerable error can be seen in the results obtained for the rod's height which was printed with the clear resin. Considering the XY resolution, the width of the channel is wider for both resins. It can be concluded that the printer is more accurate on the plane parallel to the platform compared to the Z direction. However, it should be considered that the accuracy of the printed parts can also be related to other factors such as alignment of the 3D printer and layer thickness.

4.3.2. Droplet generation device

Droplet microfluidics provides high potential in various fields such as drug delivery, organic synthesis, microgels generation and pharmaceutical industries [104]–[107]. Therefore, development in droplet generation devices and their application has increased in recent years, and cost-effective and fast fabrication methods have become essential for boosting these devices [108], [109]. Indeed, conventional microfabrication processes, such as soft lithography hinder fast prototyping of these chips and require cleanroom facilities as well as skilled operators. In addition, since the design of the device plays an important role in throughput of these devices, fast prototyping of droplet generation devices can accelerate the process of their development. Here, a microfluidic droplet generation device fabricated by a 3D printed mold is suggested.

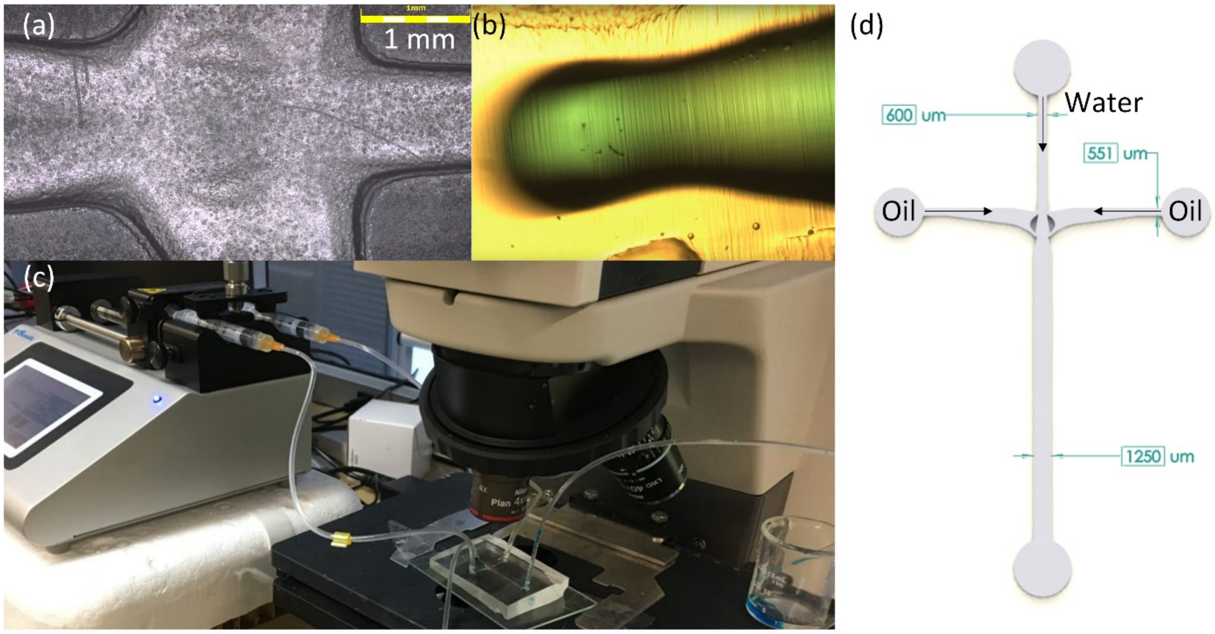

Figure 4-6 Droplet generation device. (a) laser scanning microscopic image; the 3D printer was not able to construct the bat-wing (b) generated droplet in the T junction; (c) Experiment setup consists of two syringe pumps and an optical microscope; (d) microfluidic chip design.

The design of the mold is illustrated in Figure 4.6 (d). This design contains four channels with widths of 600 μm, 1250 μm and 550 μm. The height of the channels is 600 μm. A junction with an obstacle was designed in order to generate uniform droplets during the droplet generation process within the microchannel. Using a junction with an obstacle was introduced by Li et al. to achieve highly uniform and double emulsions [110].

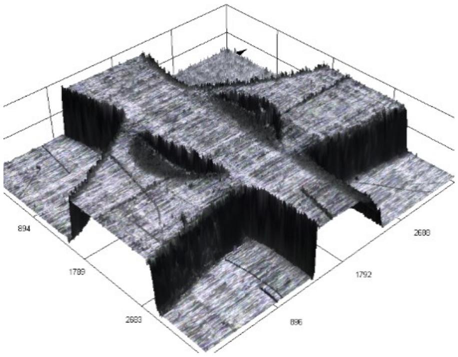

Figure 4-7 Obstacle; considerable error compared to the design.

A droplet generation mold was printed with clear resin. The demanded printing time for the first configuration is 3 hours and for the second one is 6 hours and 27 min. In order to investigate the effects of printing configuration on the accuracy of the 3D printer, two different configurations were considered. The first configuration was printing the model directly on the build platform with no support. The second one was printing the model with the support perpendicular to the build platform. A comparison between the two configurations is presented in Figure 4.8. Better resolution of the width of the channel was observed for models printed directly on the platform. However, a significant error was observed in the height of the channels compared to the models printed with support. The error is 30 percent to the designed model while the error for the model printed with support is 15 percent. When the model is printed on the build platform, the last few layers have a significant impact on the height of the channel. While the last few layers on models with supports are model's edges and don't affect the accuracy of the model in the Z direction. The printer was not able to construct the obstacle. The depth of that part was considerably lower than the one in the design. The laser microscopy image is illustrated in Figure 4.7.

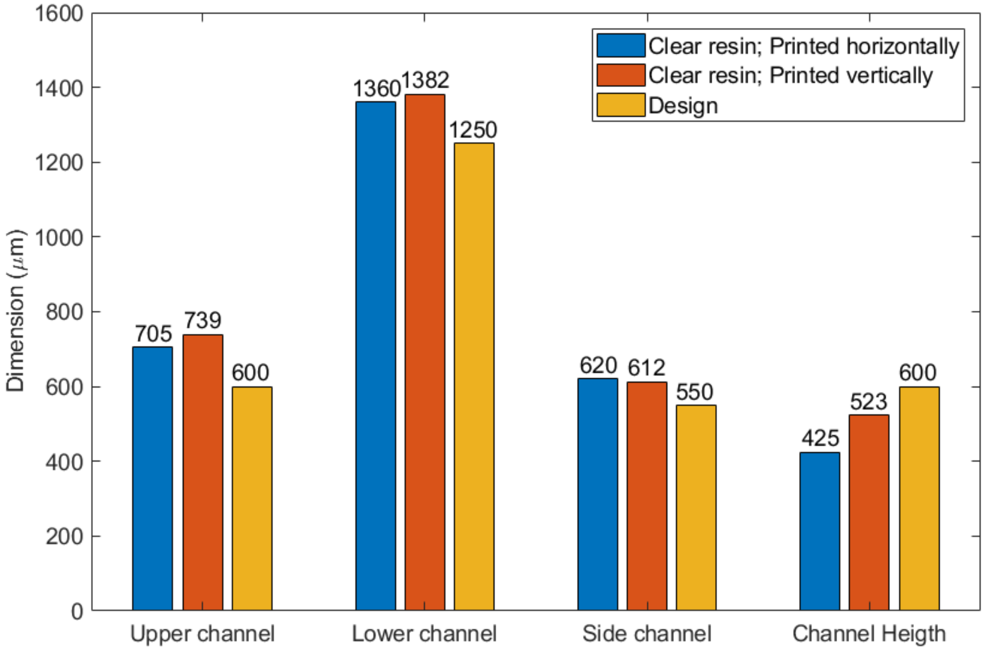

Figure 4-8 Comparison of models printed on the build platform and with supports with the design.

For the droplets generation, silicone oil was used as the continuous phase and water colored with a blue food dye was used as the dispersed phase. The water input and oil input were set to 0.14 ml/min and 0.09 ml/min. The droplet generation rate for these inputs was 0.25 droplet/s.

4.3.3. Suspended polymeric microfluidic device

Measuring fluid properties such as dynamic viscosity and density plays a critical role in many applications including physical, chemical and biological sensing [111]. Suspended polymeric microfluidics can directly measure kinematic viscosity. In such a system, the cantilever is bent due to fluid weight and shear force. However, fabrication of these devices is significantly challenging due to alignments of two layers of the device. Here, a fabrication-friendly method is suggested that can simplify fabrication of a 2D suspended polymeric microfluidic chip. In order to align two layers, 3D aligners as well as input and output holes are printed with the mold.

Positive and negative molds were designed in which the negative mold is similar to positive mold without channels. Since the accuracy of the width of the channel is more important for this particular mold, it was printed directly on the build platform with clear resin. It consists of a channel with a height of 200 μm. The channel widths inside and outside of the cantilever are 200 μm and 300 μm. In addition, in order to align two molds, a rod with a radius of 1.5 mm was designed.

In Figure 4.9 (a) a depiction of 3D microscopy image of channels in the cantilever is illustrated. It is apparent that the walls of the channel have angles of more than 90 degrees. Therefore, the cross-section of the channels has more of a trapezoidal shape than a rectangular one, with their base being wider than the upper edge as it is also illustrated in Figure 4.9 (a).

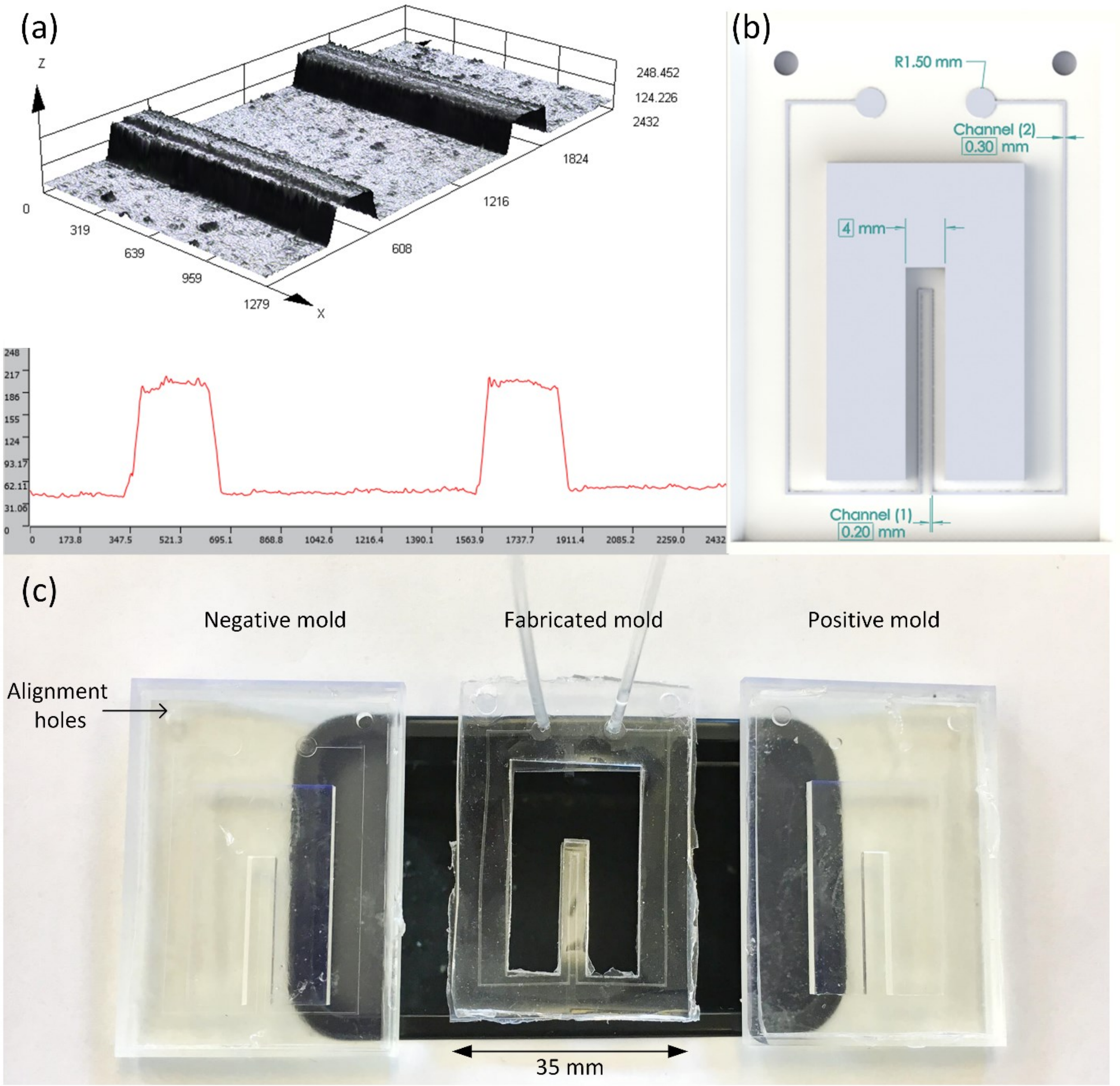

Figure 4-9 Suspended polymeric microfluidic device. (a) Laser scanning microscopic image and profile of channels; (b) microfluidic chip design; (c) molds and the fabricated device

As Figure 4.10 demonstrates, a reasonable accuracy was observed with an average error of 11%. However, as it was shown in previous models, it has a higher error of 24 % in the direction perpendicular to the printed plate.

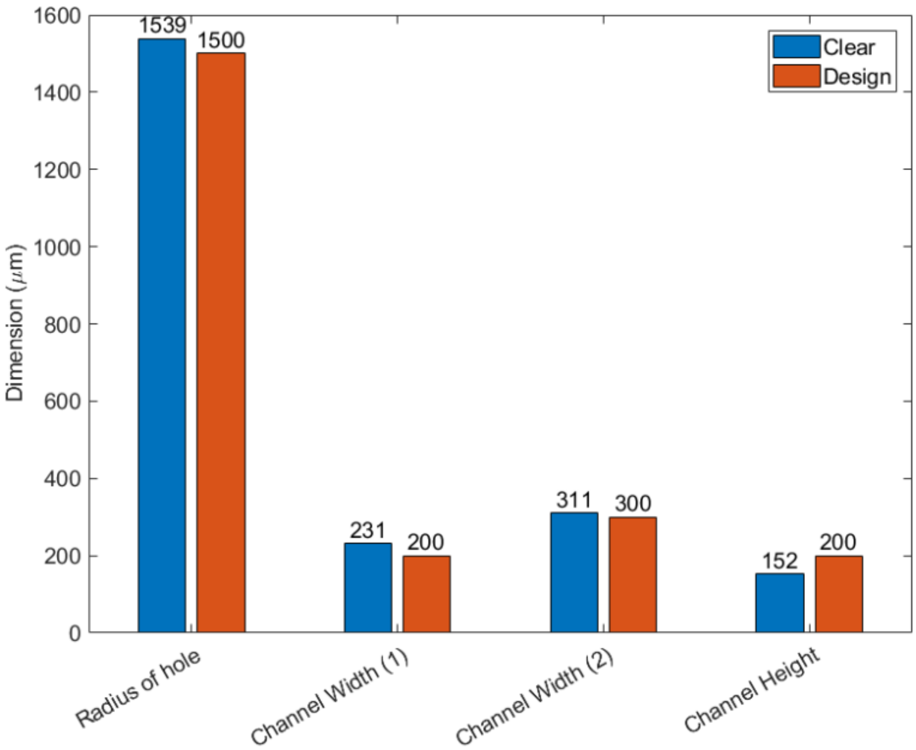

Figure 4-10 Comparison between the model and the design

4.4. Conclusions

The fabrication of PDMS-based microfluidic devices has been presented using commercially available SLA and FDM 3D printers. This study set out to determine the feasibility and simplicity of this method which does not require clean room facilities. In addition, it simplifies the fabrication of microfluidic devices with multiple thicknesses.

Reusable molds can be printed in 2 hours, at an average cost of 0.35 US$, which lead to fast prototyping and cost-effective production. FDM printing is a cost-effective method with a variety of thermoplastic filaments. Unfortunately, FDM printers are unable to print channels with features smaller than 400 μm. These factors make SLA 3D printers appealing for microfluidics. However, PDMS cannot be polymerized in contact with 3D printed molds with photoreactive resins. Therefore, post-processing is essential prior to PDMS replication.

The investigation of the printer accuracy has shown that it can construct multilevel microfluidic devices. A major limitation of this method is the low resolution and the difference between the CAD model and the printed part. Printed part by clear resin shows a more accurate result compared to other types of resin in XY direction. In addition, the height profile of the printed part is closer to the CAD model. However, a significant error has been seen in the printed parts with clear resin, particularly in the Z direction.

Besides, three platforms fabricated with two different resins were presented. The chip fabrication with conventional methods needs multiple masks or aligning which is a time-consuming method.

3D printing will almost certainly become a more common method for microfabrication in the future. There is a strong possibility that the resolution of 3D printers will be improved in the long term. A remarkable progress has been made in the fabrication of microfluidic devices with smaller features [112]. However, conventional lithography is still the most reliable and precise method, especially for mass productions. In the next chapter, a description of the experimental setup for the acoustic assisted additive manufacturing method will be presented. This method can significantly simplify and enhance fabrication of microfluidic devices.

Chapter 5

5. Experimental setup and methodology

This chapter gives a detailed description of the experimental system and procedures used in data acquisition and material characterization throughout the experiment.

5.1. Experimental setup

The overall 3D printing block diagram is represented in Figure 5.1 below.

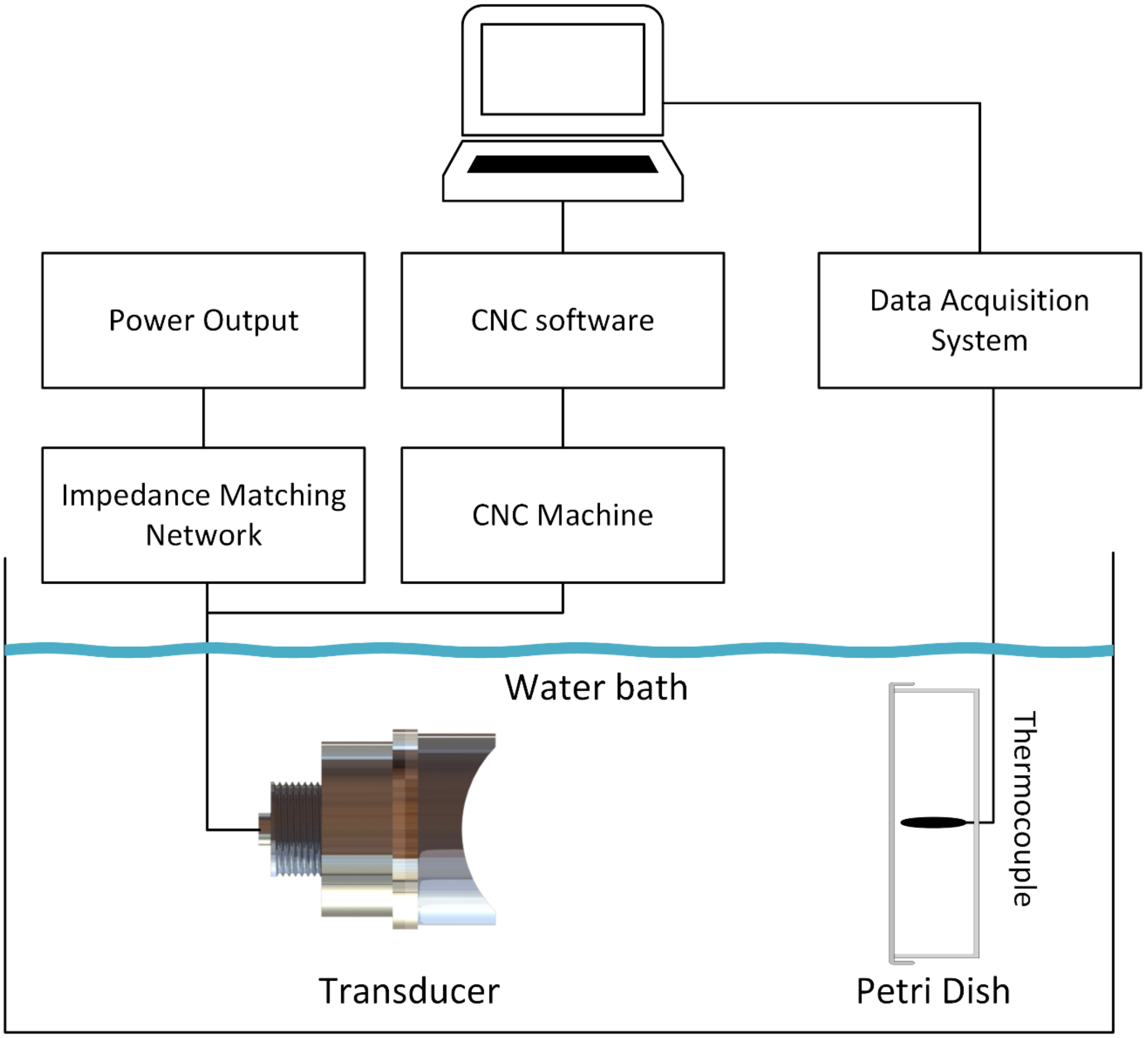

Figure 5-1 Block diagram of the experimental setup

5.1.1. HIFU system

The heart of the 3D printer is a single element transducer which converts electrical pulses to mechanical energy. The HIFU system consists of a high power focused signal-element spherically shaped transducer, spherically focused hydrophone, third harmonic impedance matching network and a signal generator. It operates at a frequency of 2.15 MHz, with an inner diameter of 22.6 mm and an outer diameter of 64 mm. The spherical radius of the curvature is 63.2 mm and it has a focal width and length of 0.76 mm and 5.72 mm respectively with a focused intensity of $46161\frac{Watts}{cm^2}$ at a frequency of 2 MHz. The transducer is specifically presented on the table below.

Table 5-1 HIFU transducer parameters

Freq	**GEOMETRY**				**PRESSURE / INTENSITY**					**FOCUS**	
MHz	ROC mm	ID mm	OD mm	Area cm^2	Pressure Focal Gain	Intensity Surface Watts/c m^2	Peak Pressure Surface kPa	Intensity Focus Watts/cm^2	Peak Pressure Focus MPa	Focal Width (dia) mm	Focal Length mm
2	63.2	22.6	64	30.50	64.35	11.15	578.26	46161	37.21	0.76	5.72

The measured efficiency and bandwidth of the transducer consists of losses in the transducer, cable and the matching network is 85%. The third harmonic impedance matching network can be used in order to operate the device in a higher frequency with smaller focus region. The third harmonic RF impedance matching allows operation to be performed in the vicinity of 3.3 times the fundamental resonance. However, the maximum power of the signal generator at the corresponding frequency of 7.35 MHz is 31 W. The efficiency at the third harmonic is about 25% lower that at the fundamental frequency. The dimension of the third harmonic impedance matching network is about 13.3 × 6.8 × 4.5 cm.

The signal generator can be operated with a maximum power of 218W at the frequency of 2.150 MHz. The signal generator is powered by AC line voltage in the range of 90-264 VAC, 48-66 Hz. The power, the frequency, period of time, the burst length and the interval can be altered by the user. The "Duty cycle" field indicates the percentage of time the output will energize. For instance, a burst length of 2 ms and an interval of 10 ms result in the output being on for 20% of the time.

PCD hydrophone is constructed to place at the center of the HIFU transducer. It is confocal to the focus of the HIFU transducer and it has a bandwidth of 10 kHz-15 MHz. The hydrophone signal was monitored using an oscilloscope (DPO 2024B, Tektronix, OR). The data obtained from the oscilloscope was recorded by Open Choice data (Tektronix, OR) for further analysis. Data attained from the hydrophone can be used to determine the frequency.

5.1.2. Positioning device

Choosing and implementing a positioning device which moves the HIFU transducer in order to effectively cure the resin at the desired point according to the CAD design is essential. The transducer is mounted in a holder connected to a computer numerical control (CNC) machine. The CNC machine was designed with a CAD software (Solidworks, Dassault Systèmes) and purchased from Stepcraft Inc. The Stepcraft 420 Desktop CNC System consists of 3 stepper motors (Nanotec®) to move the transducer in three directions. The resolution and the repeatability of the machine according to the datasheet of the device are 0.005 mm and 0.04 mm which are suitable for 3D printing. The Coordinates of the printing path can be given to the machine according to the desired part using G-code (UCCNC, Hungary). The working space of the machine is 300 × 420 × 140 mm and its weight is 15 kg [113].

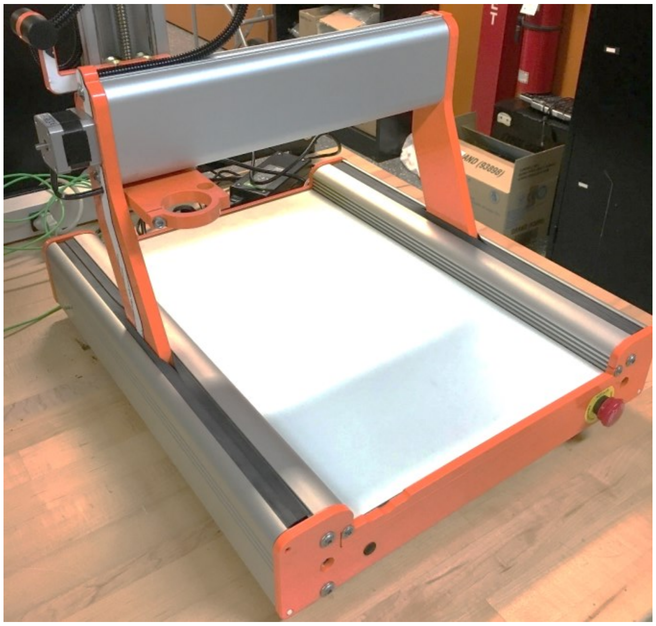

Figure 5-2 Assembled CNC machine

5.1.3. Data Acquisition System

Temperature is one of the most important parameters in our system, in order to have an effective control over the curing of the resin. A digital thermometer will be used to capture the variation of temperature with respect to time at various locations in water and the resin container and store them in the desired format for future analysis. The digital temperature monitoring system consists of an eight-channel port for the thermocouple input (National Instrument NI 9212) connected to isolation amplifier module (National Instrument NI cDAQ™-9171) which is connected to the computer via a USB cable for acquiring data through the LabVIEW software [114], [115]. T-type copper-constantan thermocouples with diameters of 0.25 mm (Omega Engineering, INC.) were opted to measure the temperature because of their repeatability, accuracy, response time and sufficient stability at the operating temperature of our experiment. The temperature error of the thermocouple is in order of 0.1 °C.

Thermocouples are calibrated before testing to ensure they have the correct reference temperature. They were submerged in boiling water (assumed 100 °C) in order to be adjusted.

5.1.4. Water container

The degassed deionized water container that hosts the HIFU transducer was made from half-inch transparent acrylic plates. The container is open to the atmosphere and it was designed according to the CNC device to maximize the working place for printing. The dimensions of the container are 49 × 30 × 16 cm.

5.1.5. Resin container

The resin is separated by a divider with an acoustic impedance close to water's to decrease the absorption of the acoustic wave through the divider. As it was discussed in Chapter 3, divider has a remarkable impact on the transmitted energy through the resin tank.

In addition, other factors such as transparency, surface roughness and melting point of the divider should be taken into account. Since the divider can experience high-temperature rise due to heat induced by the ultrasound, a divider with a higher melting point ought to be precisely chosen. In addition to these factors, in order to monitor the printing process, a transparent material is required. Moreover, rough surface roughness can lead to nonuniform reflection of sound waves through the divider. This can significantly affect the printing resolution.

The interplay between these parameters contributes to choosing polystyrene as an ideal material for the divider. In the table below, a comparison between critical parameters such as Heat Deflection Temperature (HDT), intensity at the focal and transparency for dividers is presented.

Table 5-2 Comparison between different parameters for dividers

Material	**HDT @0.46 MPa (°C)**[116]	**Intensity focus (kW/cm^2)**	**Transparency**
ABS	84	18.2	x
Polystyrene	**87.5**	18.1	✓
LDPE	45	**24.7**	x

According to Table 5.2, although LDPE has an acoustic impedance closer to water's and most of the energy is transmitted through it, transparency and higher Heat Deflection Temperature of polystyrene make it an ideal material for a divider. Therefore, a polystyrene petri dish was selected as the resin container [117].

In order to place the petri dish in the water container, a stand was designed to hold the petri dish. This leads to achieve a consistent position for the petri dish in different experiments. The setup including the CNC machine, the petri dish stand, the petri dish and the water container is illustrated in Figure 5.3.

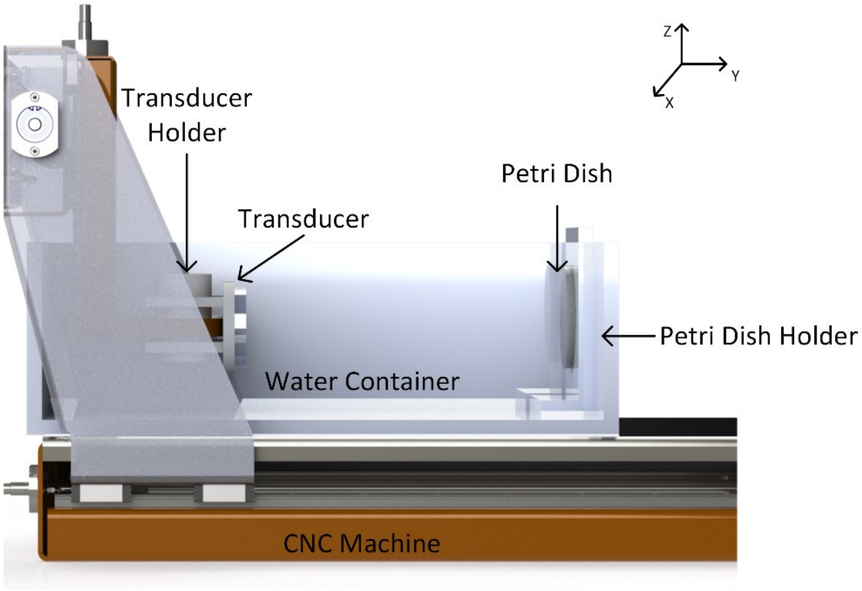

Figure 5-3 3D printing setup; the CAD model was designed using SolidWorks

5.1.6. Thermochromic liquid crystal sheet

Liquid crystals are highly temperature sensitive material that react by changing their color when exposed to temperature. These sheets are normally black and are functional for thermal mapping. Thermochromic liquid crystal sheets usually alter through a spectrum of colors within a 5 degree Celsius temperature bandwidth.

Here, a liquid crystal sheet will be used in order to indicate the position and shape of the focal region. A liquid crystal sheet with a temperature range of 40-45 °C was purchased from Edmund optics. The sheet will be placed parallel and perpendicular to the transducer's surface in order to demonstrate the shape of the focal region in both directions.

5.2. Methodology

5.2.1. CNC post processor

Ultrasound waves reaching the divider between two mediums at an angle may be subjected to refraction and reflection. Refraction will change the direction in which the passed ultrasound waves proceed to propagate in the resin tank, whereas the reflection will diminish the energy proceeded in the transmitted ultrasound beam. Therefore refraction may relocate the focus away or close to the geometrical focus and disphase the focal spot which should be taken into account. Therefore, the 3D printer has to be calibrated for each divider material and each different thicknesses. In addition, it is essential that the CNC machine is referenced to its absolute position since the G-code is written with respect to this coordinate system. Therefore, the CNC machine needs to update its coordinates each time according to the resin container.

In this regard, a post processor for the CNC machine was developed to determine the initial position for printing according to resin and the divider acoustic properties. In addition, the movement of the focal region in the direction parallel to the surface of the transducer in the resin tank is not equal to the CNC movement in the same direction due to refraction of acoustic waves as it is illustrated in Figure 5.5.

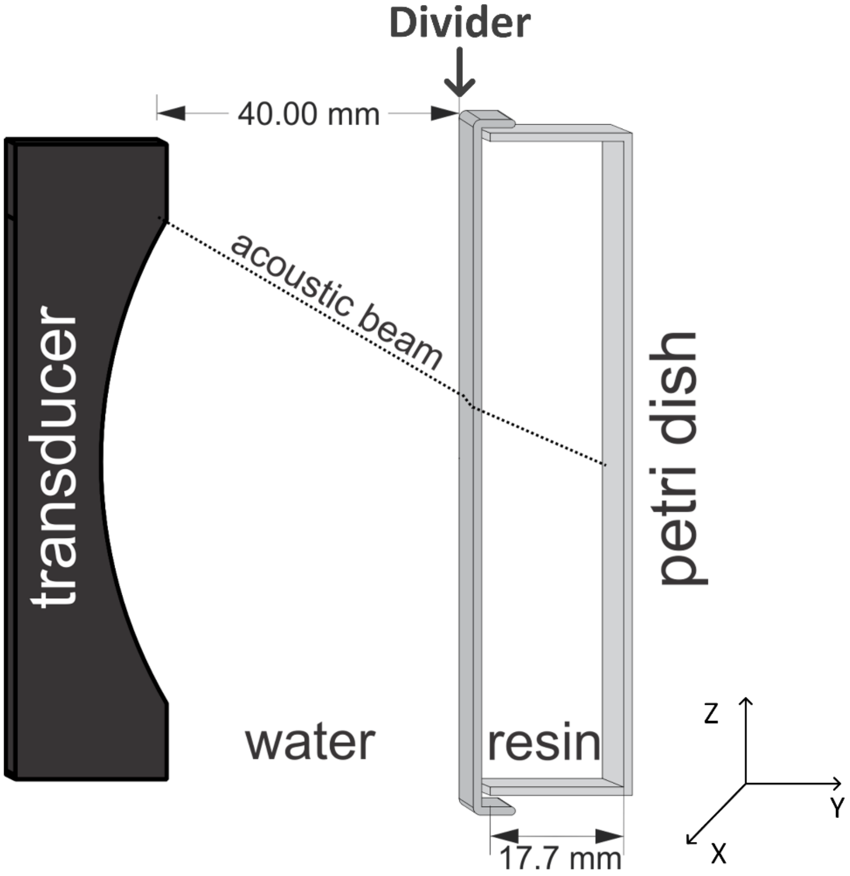

Figure 5-4 Refraction of the acoustic beam in the resin container

The coordinate system is set at the center of the petri dish lid. The G-code given by the CAM software will be altered according to the new coordinate system by Equation 1. This formula was obtained according to Snell's law with acoustic properties of water, PDMS, and polystyrene in the room temperature.

$$\begin{bmatrix} X \\ Y \\ Z \end{bmatrix} \xrightarrow{Post\ processor} \begin{bmatrix} X \\ Y^* \\ Z \end{bmatrix}; \qquad Y^* = \frac{(Y-1.12)-78}{1.5} \tag{1}$$

The post-processor can change the coordinates of the design according to the CNC coordinate system. The initial printing point corresponds with the point that the focal point is placed on the petri dish surface. The transducer is placed 40 mm away from the petri dish lid at this position. The transducer moves away from the petri dish by adding printing layers.

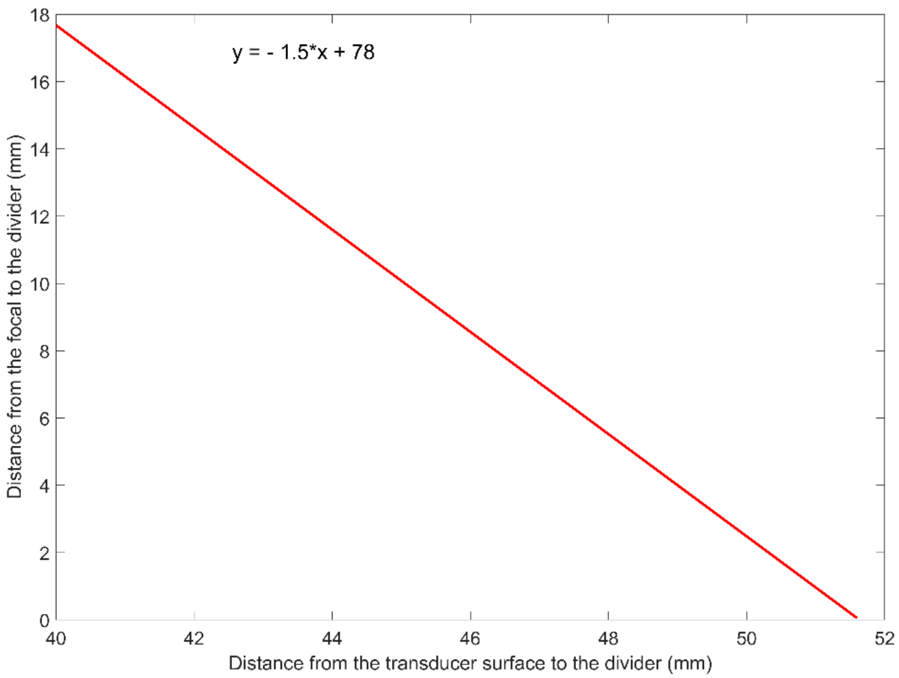

Figure 5-5 Machine's reference position

In order to set the CNC coordinates according to the resin container, the transducer moves as long as it touches the surface of the petri dish. Then this position is set as the reference coordinates for the positioner machine and the CNC moves backward for 40.00 mm. The reason behind choosing 40 mm for this purpose is the program which was written based on Snell's law and the petri dish dimensions.

Besides, the program will be used to determine the printing space in the petri dish. Since the acoustic beam is conically focused in the focal region, the movement of CNC must be in a way that all acoustic waves penetrate from the surface of the petri dish. Otherwise, partial transmission of waves would be through the petri dish edges and can change the magnitude and position of the maximum pressure.

Taking together, the post-processor will be used in three ways, including referencing the CNC machine, determining the printing space and converting the G-code obtained from the design to the one in the printing path to achieve the desired layer thickness.

5.2.2. HIFU thermal field characterization

In order to record the temperature rise in water an experiment was designed as illustrated in Figure 5.6. The HIFU beam must be focused on the thermocouple to achieve the maximum temperature rise in water. Therefore, the transducer at a power of 218 W and a frequency of 2.15 MHz was moved along the beam axis and in both orthogonal directions with a feed rate of 150 mm/min to find the exact location of the focal spot according to the maximum temperature. Then the transducer started to sonicate for 1 second and temperature rise was acquired by the Data acquisition system. This method for temperature measurement is subjected to several limitations which will be discussed in Chapter 7.

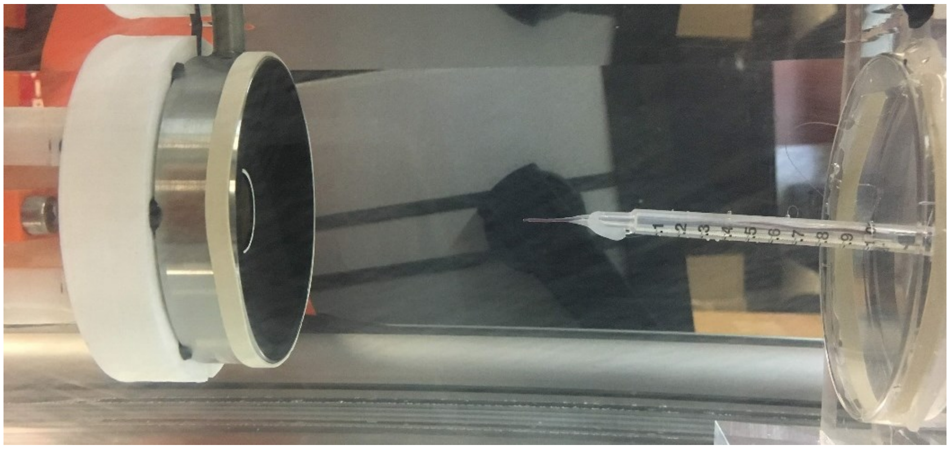

Figure 5-6 Temperature measurement setup

This chapter provided a comprehensive description of the experimental setup and procedures used in data acquisition and material characterization throughout the experiment. However, the material characterization plays an important role in the printing process which will be discussed in the next chapter.

Chapter 6

6. Material selection

In this chapter, the material selection process is reviewed and the effect of different parameters on the curing time is investigated. Selecting a proper thermoset material plays a key role in rendering a 3D printed part with high resolution and accuracy.

6.1. Thermosetting polymers

Thermoset materials are used as the resin for the device. Thermosetting polymer is a polymer that is irreversibly cured from a viscous liquid or soft solid resin. The process of curing starts with heating the mixture of the resin and its curing agent. Thermoset resins are usually liquid prior to curing and cannot be heated to reshape the cured part. These polymers usually consist of a base material and their curing agent and are usually stronger than thermoplastic materials. Since thermoset polymers have the three-dimensional network of bonds, they are stronger than thermoplastic polymers and possess hardness, good rigidity, and high thermal stability [118].

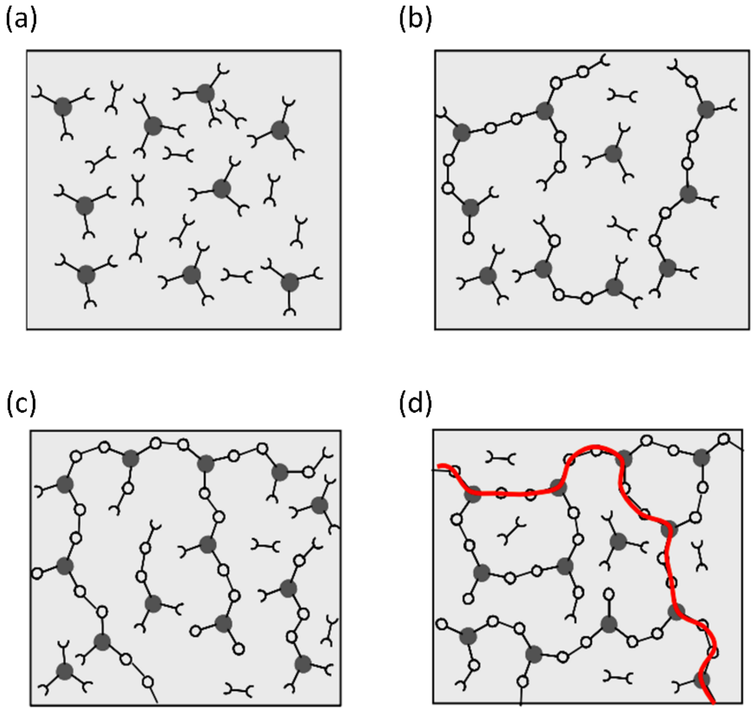

Figure 6-1 Schematic diagram of the cross-linking steps; (a) unreacted monomers; (b) linear branching and growth; (c) the gel point; (d) the cured, crosslinked polymer with some unreacted groups [119].

Curing a resin converts it into an elastomer or plastic by crosslinking of polymer chains through the formation of covalent bonds among independent chains of the polymer. The curing process initiates with a reduction in the resin viscosity upon the application of heat and the viscosity starts to increase as the chemical reactions grow the length and the degree of cross-linking between oligomers. The process resumes as far as an extended 3-dimensional network of oligomer chains is formed. This stage is known as gelation. In order to obtain vitrification in the resin, elevation in the process temperature usually is required following gelation [120].

6.2. Influence of time, temperature, and mass on the curing process

The ambient temperature highly impacts cross-linking rate. Since all thermosetting reactions are exothermic, the rate of reaction is affected by a mass effect. Polymerizing mixture of monomers can be traced by monitoring the viscosity alternation versus time at a particular temperature. As it is illustrated in Figure 6.2, the curing process begins at t_0, and a mixture viscosity of η_0. The generated heat due to the exothermic reaction causes a viscosity reduction (η_0). The increment in molecular weight of the mass leads to mixed viscosity increase. The molecular enlargement resumes gradually until it reaches the gel point (t_{gel}).

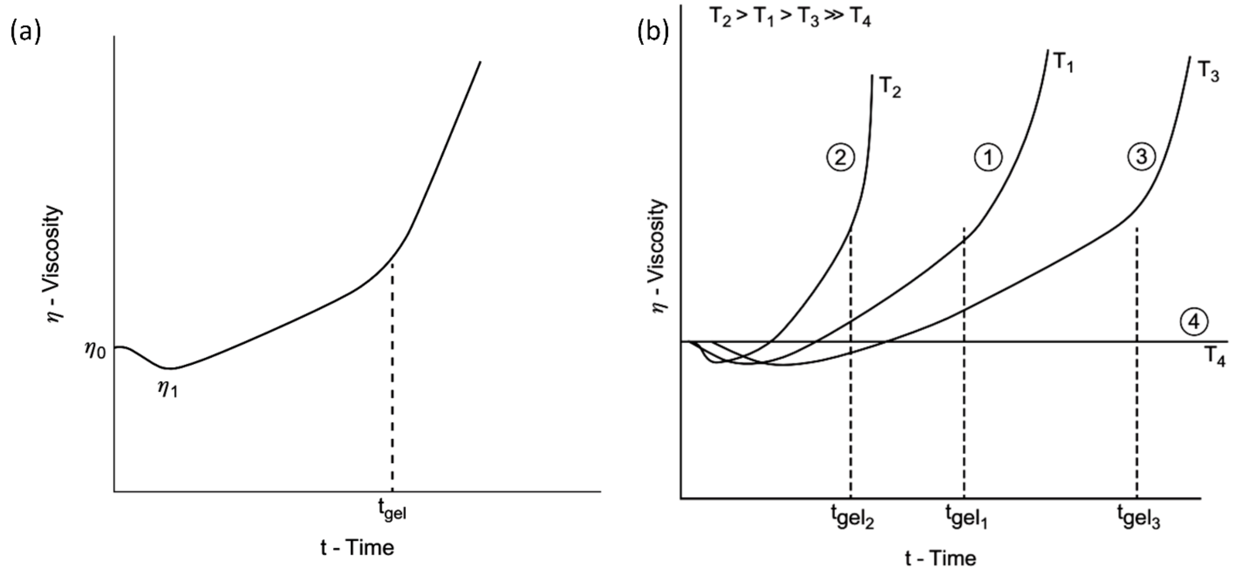

Figure 6-2 (a) Viscosity versus time at constant temperature. (b) Effect of ambient temperature on the gel time [118].

The viscosity goes to infinity from this point; more specifically, the polymeric mass turns into a macroscopic solid.

Temperature influences the cross-linking reaction. Basically, augmentation in the ambient temperature leads to an elevation in the reaction rate. In addition, since thermosetting resin is exothermic, the exothermic heat adds to the input heat. Figure 6.2 (b) shows the effect of the ambient temperature on the curing time.

In addition, gelation is a factor of mass. A cross-linking mass increment leads to a drop in the amount of heat transfer of the exothermically generated heat from the reaction site since polymers are naturally thermally insulative materials [118], [121].

6.3. High and low exothermic resins

Resin generates exothermic heat that can affect the curing time. Thermoset resins may be classified on the basis of the exothermic process to low exothermic resins and high exothermic resins. High exothermic resins are also known as chemically dominant polymers can be polymerized rapidly in the room temperature. The application of these polymers such as epoxies is mostly in structural adhesives. In contrast to high exothermic resins, low exothermic or thermally dominant resins require elevated temperature during the polymerization process. In our application, low exothermic resins are preferred since more control can be achieved during the printing process. Otherwise, chemically curing of the resin leads to low resolution and limited time for printing. In addition, exothermic resins can deflect the resin container due to the exothermic reaction.

6.4. Experiment materials

Five different thermoset polymers and their curing agent have been chosen and tested as presented in Table 6.1.

Table 6-1 Selected polymers

Base polymer	**Curing agent**	**Supplier**	**Category**
EPON™ 828	EPIKURE™ 3270	Miller-Stephenson	High exothermic
EPON™ 8021	EPIKURE™ 3271	Miller-Stephenson	High exothermic
XIA RTV-3481	XI4107138	Krayden	Low exothermic
Proxima® HPR 2100	Proxima® CT 722	Materia	High exothermic
Sylgard® 184	Catalyst 87- RC	DOW	Low exothermic

EPIKURE™ 3270 and EPIKURE™ 3271 are modified aliphatic amines. Aliphatic amines are the largest group of epoxy curing agents and known as short lives and high exotherms [122]. Therefore, EPON™ 828 and EPON™ 8021 with their curing agents are characterized as exotherm resins.

Sylgard® 184 or PDMS and XIA RTV-3481 are classified as silicone polymers. Silicones are polymers including silicone and oxygen atoms covalently bonded as linear chains. Silicone elastomers are classified as room-temperature-vulcanizing (RTV) and heat curing systems (HTV) [123]. PDMS and XIA RTV-3481 are HTV and RTV silicones, respectively. However, the polymerization process for both polymers is a low exothermic process. Therefore, these material are suitable for the application of 3D printing.

Proxima® HPR 2100 and Proxima® CT 722 consists of a two-part thermoset polymer system that provides a superior toughness performance. This thermosetting system is created with blends of dicyclopentadiene (DCPD) and other norbornene monomers which are thermally activated by the catalyst [124].

In order to investigate the effect of the exothermic process on the curing time, one kind of epoxy and PDMS were tested at room temperature. The curing time corresponding to each resin was around 24 H and 10 min for PDMS and epoxy, respectively. It is apparent from Figure 6.3, the exothermic polymerization process, distorted the resin container whereas PDMS could not deform the container.

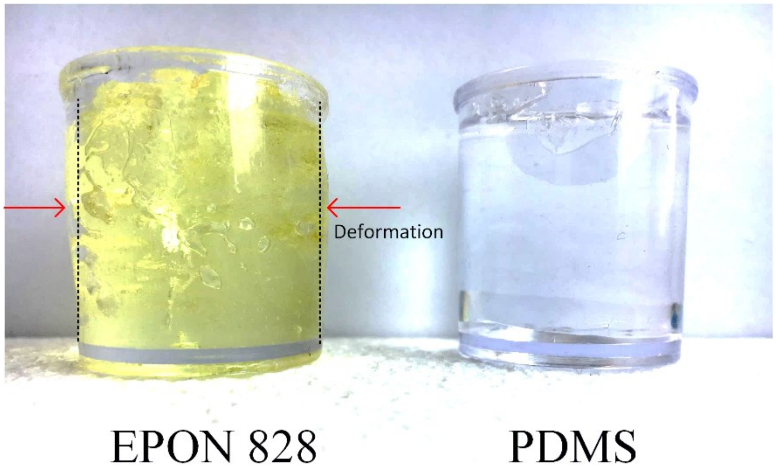

Figure 6-3 Deformation of the EPON 828 container

In addition to the discussed parameters, viscosity and density of material have a significant impact on the process. The material is ideally highly viscous and has an acoustic impedance close to water. Silicone elastomers possess higher viscosity compared to other polymers. Due to the acoustic streaming in the printing process, high viscosity can reduce the streaming and lead to a higher resolution. In contrast, for material with lower viscosity, streaming impedes the process and the whole container is heated by the heat induced by the ultrasound.

Physical properties of polymers are presented in Table 6.2 which shows higher viscosity of the silicone elastomers.

Table 6-2 Properties of thermoset polymers

Polymer	**Viscosity (CP)**	**Density at 25°C (g/cm³)**
EPON™ 828	110-150 @ 25 °C	1.16
EPON™ 8021	85-115 @ 25 °C	1.10
XIA RTV-3481 (Mixed with curing agent)	20000 @ 25 °C	1.21
Proxima HPR 2100	250 @ 30 °C	1.03
Sylgard® (Mixed with curing agent)	3500 @ 25 °C	1.03

PDMS high viscosity and low exothermic curing process make it an ideal material for the 3D printer. Also, it is used in a variety of biomedical applications including lab-on-a-chip and medical devices. In addition, it has been demonstrated as difficult to print with conventional 3D printing methods due to its low modulus of elasticity and high curing time [42]. Therefore, in the next chapter, two PDMS fluidic devices will be fabricated by the HIFU 3D printer.

Chapter 7

7. Results and discussion

The aim of this chapter is to investigate and discuss the influence of different parameters on the printing process. Also acoustic streaming a major phenomenon that affects the process will be discussed. In addition, two fluidic channels will be printed by this method which present a huge potential in the field of microfluidics. In the end, a new method of fabricating molds for circular microfluidic channels will be presented.

7.1. Acoustic Streaming

Acoustic streaming was observed during the sonication in water and resin. A transfer of energy between the propagation media and the acoustic wave was induced by wave propagation in a viscous fluid, leading to acoustic streaming. Acoustic streaming was first investigated by Eckart (1948), who developed an expression for the streaming velocity [125]. Many studies have investigated the relationship between acoustic intensity and acoustic streaming by various techniques including particle image velocimetry, Doppler ultrasound, and magnetic resonance imaging methods [125]–[131]. Acoustic streaming generated using a HIFU transducer has been reported in many studies using digital particle image velocimetry (DPIV). In our application, it is essential to characterize and observe the fluid stream to predict the acoustic streaming field.

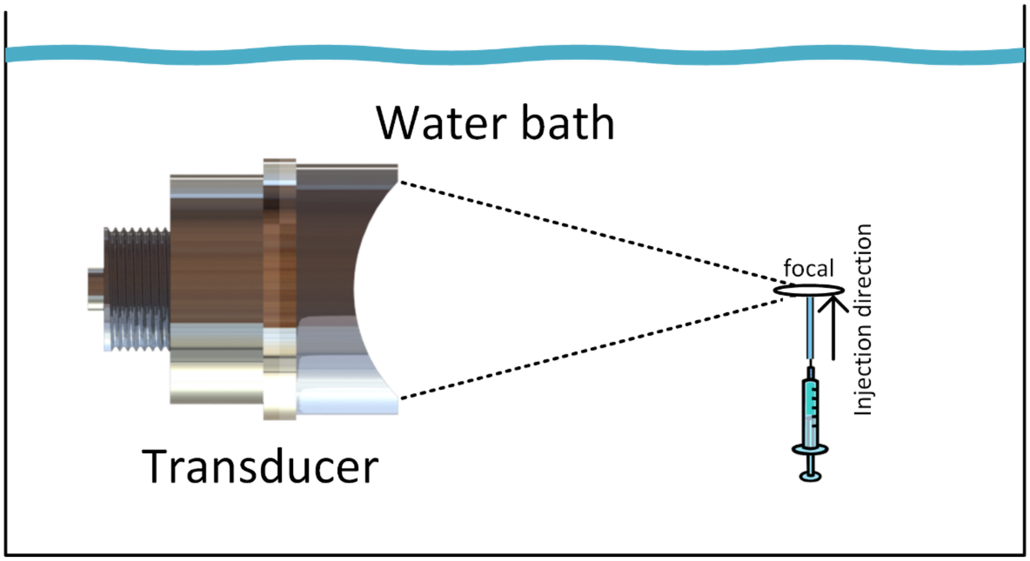

Figure 7-1 Setup for observing the acoustic streaming

In order to observe fluid streaming conducted by the high pressure in the focal region two experiments were designed. The experiments were carried out at room temperature with deionized degassed water. As shown in Figure 7.1, the outlet of the tube was placed in a parallel manner to the transducer surface in the focal region. Then deionized dyed water was injected generously in the media and the pulse generator was turned on and off repeatedly. As can be seen in Figure 7.2, when the input power was on, the dominant pressure moves the stream away from the transducer surface and it stopped when the input power was off. This experiment indicated that the effect of streaming is considerable on the printing process.

Another experiment was designed using acrylic particles to visualize the motion of the particles in presence of an acoustic field. Particles were added to the resin prior to the experiment. In addition to acoustic streaming, curing of the resin can be observed by this method, since the particles ceased in the region that resin was cured.

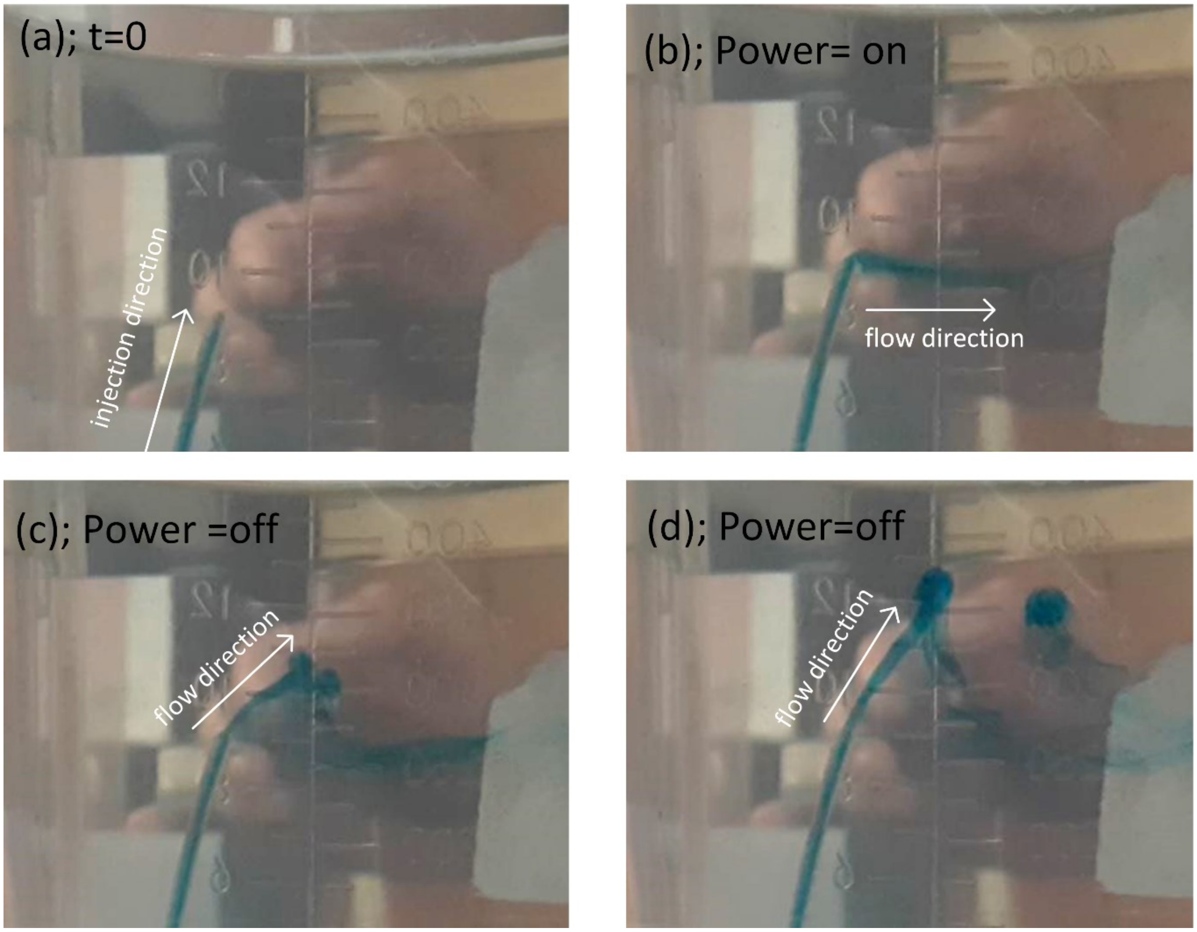

Figure 7-2 Acoustic streaming in the focal region, the transducer is placed on the left; (a) power is off and flow is not injected; (b) power is on; (c) turning off the power; (d) power is off

These experiments emphasize on the effect of streaming on the printing process. In order to overcome the acoustic streaming, printing can start from a plate, so it could have a support to prevent streaming to affect the resolution of the printing.

7.2. Simulation verification

7.2.1. Acoustic field

In order to verify the simulation results, the calculated pressure and the intensity obtained by the simulation were compared to the device data sheet. The pressure at the focus obtained by the simulation is presented in Figure 7.3.

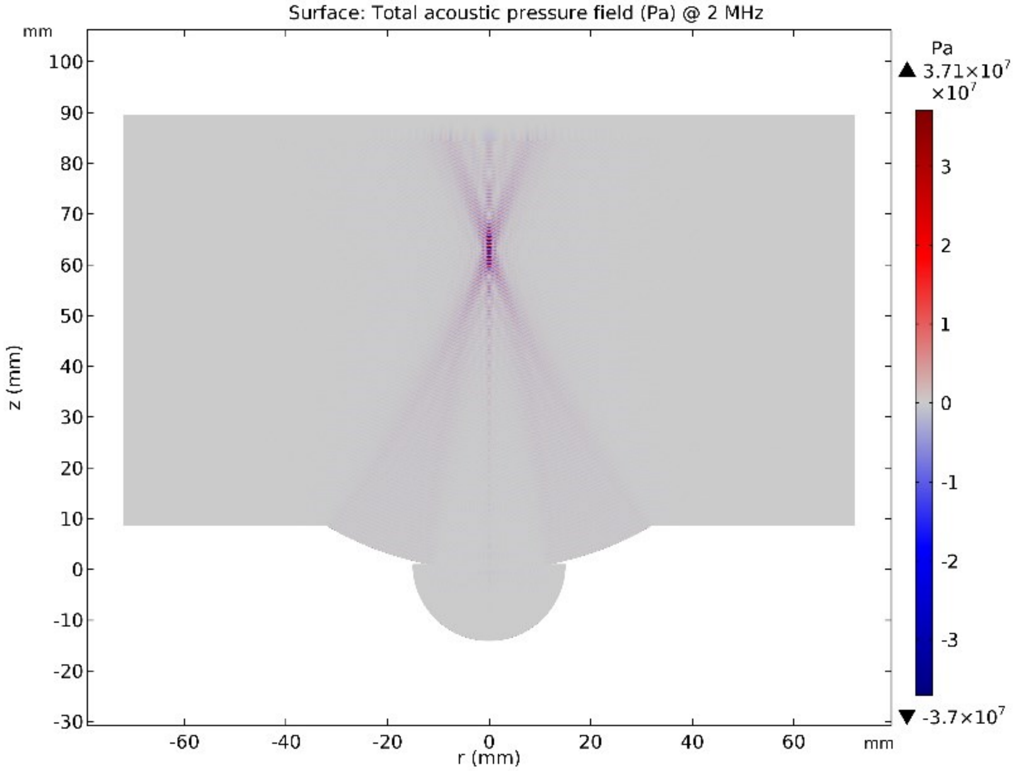

Figure 7-3 Acoustic pressure field obtained by the simulation at a power of 400W and a frequency of 2 MHz

The pressure is in good agreement with the device datasheet which is 37.21 MPa. However, there is a 6 percent error between the maximum intensity achieved by the simulation and the device datasheet. The acoustic pressure and the velocity are not in the same phase for a strongly focused beam. Therefore acoustic intensity is not proportional to the square of the pressure field. This leads to an error in the calculation of the intensity of the transducer.

7.2.2. Temperature rise

As discussed in Chapter 3, there is a temperature rise during the sonication period followed by temperature decay after sonication. Results illustrated in Figure 7.4 show the characteristic heating and cooling profiles. However, there is a significant difference between the simulation and measured curves due to thermocouple limitations for HIFU experiments which have also been reported by many researchers.

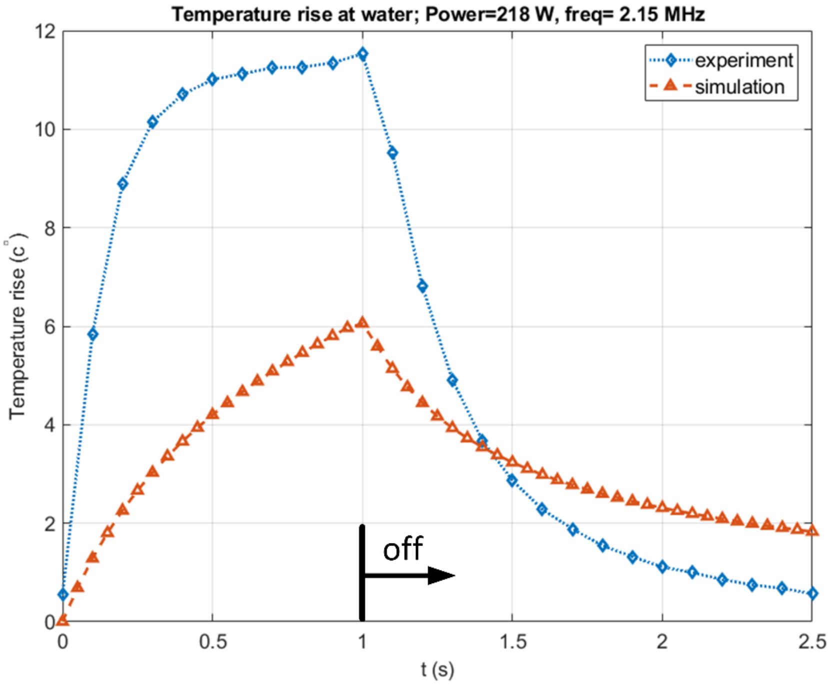

Figure 7-4 Measured temperature profile with a thermocouple and the simulated profile in water

Several research groups have revealed that temperature recorded using thermocouple can be imprecise due to the well-known “thermocouple artifact” effect. This imposes an extra temperature rise over the temperature rise in the water generated by absorption of acoustic waves [132]–[136]. Therefore, the measured temperature rise is higher than the computed temperature rise due to additional heating by artifacts. A number of studies have indicated that thermocouple artifact magnitude depends on the probe size, orientation, material and the operation power and frequency [134], [137]. However, self-heating artifact is observed even for the smallest thermocouples. In addition to aforementioned parameters, the difference between the thermal conductivity between the thermocouple and the surrounding water is reported as another source of thermocouple artifacts [138]. Thermocouples are made from metal with higher conductivity such as copper and cromega which lead to a distortion of the thermal field. In addition, there is an error in cooling curves due to the acoustic streaming which leads to faster heat dissipation in the experiment compared to the simulation . Taken together, it can be concluded that focusing of the HIFU acoustic beam causes significant error in the measured temperature rise as a result of thermocouple artifact effect. Alternative methods to characterize the thermal field such as magnetic resonance imaging (MRI) method is suggested. However, this method is expensive and not widely accessible.

7.3. Characterization of focal shape using a thermochromic liquid crystal sheet

The HIFU acoustic beam focuses energy on a small region with the size of a grain of rice. The black thermochromic sheet responses to the acoustic energy as its temperature increases. The focus is apparent as light spots on the liquid crystal sheet as it is illustrated in Figure 7.5.

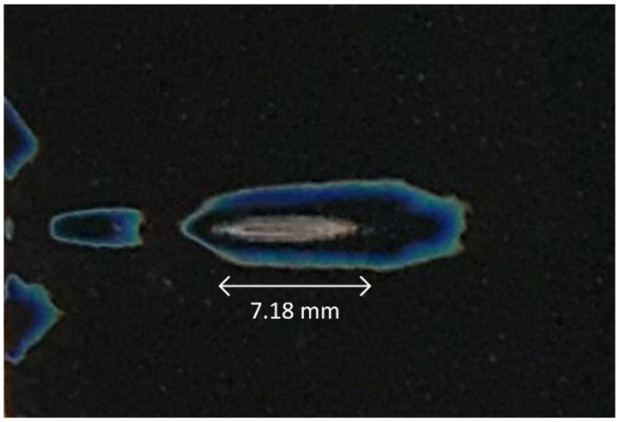

Figure 7-5 Visible light spot at the focus; Transducer is radiating from the left

The measured focal width and length on the thermochromic sheet are approximately 7.18 mm and 0.95 mm, respectively. The thermochromic sheet assists to find the exact location and shape of the physical focal.

7.4. Fabricated channels by acoustic-assisted printing

In this section, two printed models by PDMS will be presented. Since mixing ratio of 10:1 is the most common ratio in fabrication of microfluidic devices, this ratio was chosen for experiments. The second sample has a smaller feature compared to the first one. The resolution and dimensions of models will be discussed.

The first model consists of a channel with a width of 4 mm. it was fabricated at the frequency of 2.15 MHz and the input power of 170 W. The feed rate and layer thickness were set to 300 mm/min and 0.25 mm in the G-code. The G-code including printing paths was obtained by CATIA and was given to the CNC machine software. The tool size which is basically the spot size was set to 2 mm. In order to increase the depth of the channel two layers were printed. The design of the model and the printing paths are illustrated in Figure 7.6.

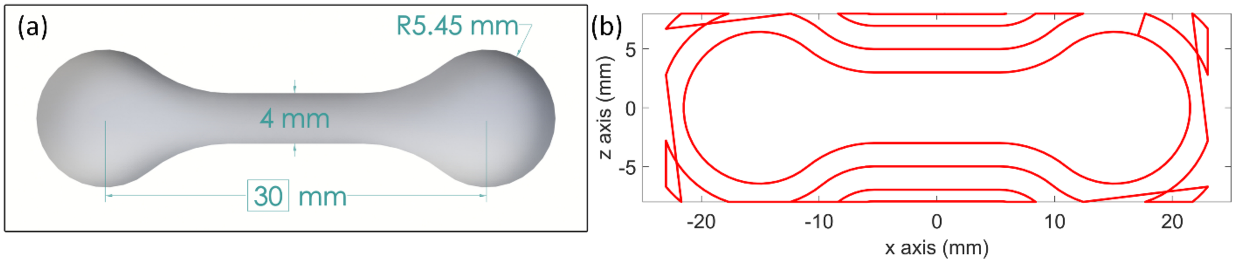

Figure 7-6 First model; (a) design of the model (b) printing paths generated by a CAM software

The printed model is shown in Figure7.7 (a). As can be seen, polymer was not polymerized in some regions, which can be a result of a minor misalignment of the resin container. However, PDMS was completely polymerized in the inner printing paths. In addition, defining a large spot size led to a gap between printing paths. The obtained spot size and channel width are 1.24 mm and 4 mm respectively. The printed model was covered and bonded with a PDMS layer for closing the channel as can be seen in Figure 7.7 (b). In order to achieve a conduit, a thin layer of PDMS was poured into a petri dish and the model was placed on top of it. This leads to obtaining a channel with a smaller aspect ratio. The input and output holes were drilled prior to bonding. No leakage was observed during the testing process with dyed water.

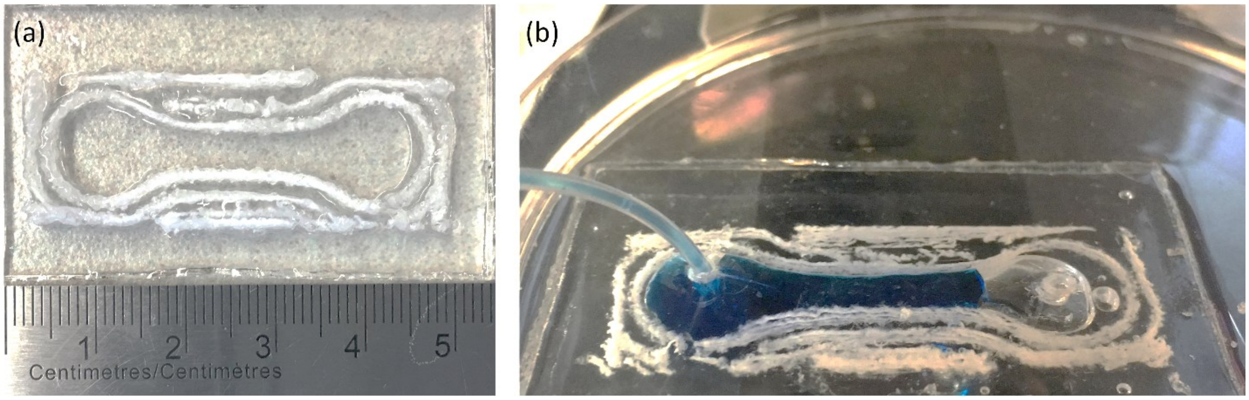

Figure 7-7 First model with a channel; (a) printed model; (b) fabricated chip covered with a layer of PDMS during testing with dyed water

The second printed channel comprises a smaller channel with a width of 2 mm. The spot size was set to 1 mm to provide a better resolution compared to the first sample. The model was fabricated with three layers at the feed rate of 300 mm/min. The input power was set to 170 W, 190 W and 218 W for the first, second and the third layer. The transducer was driven at the frequency of 2.15 MHz and the duty cycle of 100%. The designed model and printing paths are shown in Figure 7.8.

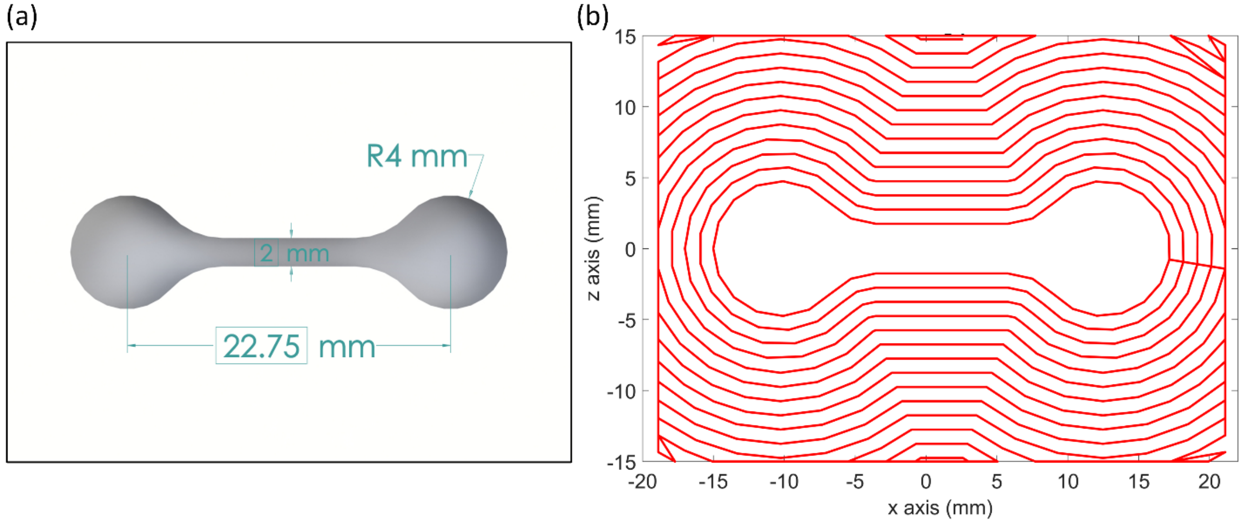

Figure 7-8 Second model; (a) design of the model; (b) printing path generated by considering a spot size of 1 mm.

The printed model is illustrated in Figure 7.9 (a). The channel width is 1.68 mm in the printed model. The resolution of this model is significantly better due to smaller spot size which was set in the G-code. However, the surface of the model is rough and nonuniform. In order to cover the channel, a glass slide was covered with a thin layer of uncured PDMS and the printed model was place on top of it. Then the part on the glass slide was placed into the oven at 40° C for 4 hours. The fabricated device is illustrated in Figure 7.9 (b). Since the surface of the model was rough, plasma bonding did not work. Then the model was tested with dyed water. These results suggest that, fabrication of microfluidic devices is feasible by using a transducer with a smaller focal width.

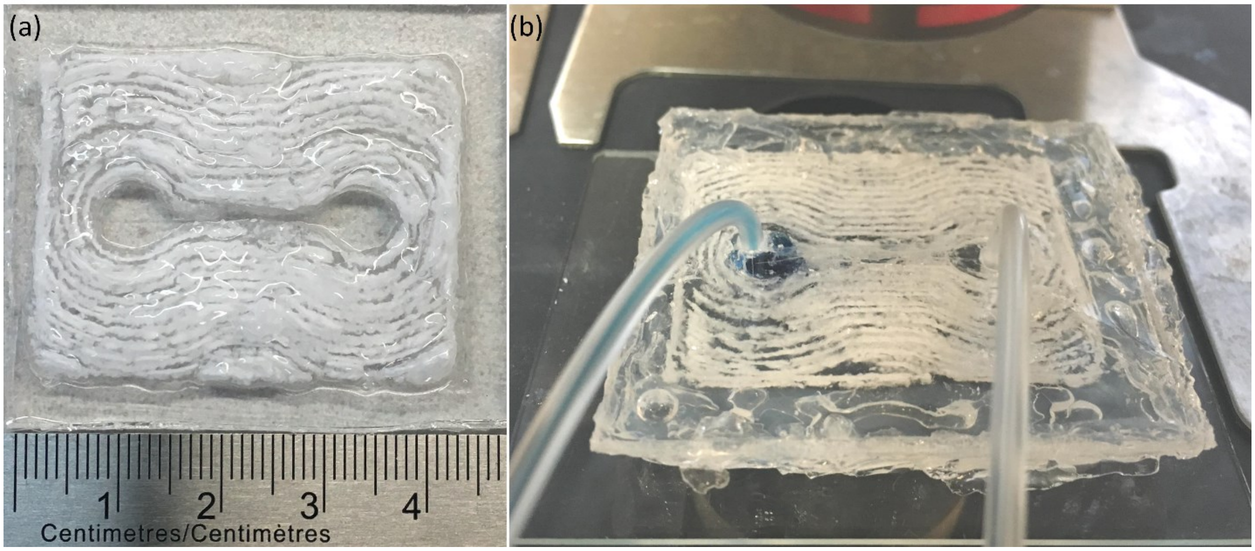

Figure 7-9 Second printed model with a smaller channel; (a) printed model; (b) fabricated chip bonded with a glass slide during testing with dyed water

7.5. Mold fabrication on acrylic plates by a high intensity focused transducer

Another method in which HIFU transducers can be used is fabrication of an acrylic mold for microfluidic applications. Despite the molds fabricated by SLA 3D printers as it is discussed in Chapter 4, acrylic molds do not require post-processing. This can significantly facilitate fabrication of PDMS-based microfluidic devices.

This method is based on focusing high-pressure amplitudes on an acrylic sheet which leads fabrication of the mold for microfluidic channels on the acrylic sheet surface. The thickness of the acrylic sheet is 2.8 mm. The main advantage of this method is achieving circular channels compared to other methods such as 3D printing or soft lithography which are limited to the construction of rectangular channels. Circular channels are of considerable attention for many biomedical applications, since they mimic biological flow systems such as vein networks. In addition, axis-symmetrical flow, and uniform shear form can be achieved by applying circular channels.

Moreover, the time and cost required for this method are remarkably lower than that in 3D printing methods. Required time for fabrication of each mold is less than a minute. In order to present the potentials of this method a Y channel was designed with a length of 3 cm. The width and height of the mold depend on the focal width, input power and the distance between the transducer and the acrylic sheet. The designed Y Channel and fabricated molds are illustrated in

Figure 7.10. As it can be seen in the figure, high power and low feed rate can lead to cavitation in the acrylic part and decrease the smoothness of the mold. The three models on the right have better surface roughnesses. These models were fabricated at DC of 60 %, feed rates of 100 mm/min, 80 mm/min and 90 mm/min, frequency of 2.15 MHz and input power of 218 W. The experiment was performed at different feed rates and duty cycles. In addition, the distance from the transducer and the acrylic plate have a significant impact on the channel width and height. The best channel size achieved by fabricating 35 molds had a 1.05 mm width and a 47 μm height.

Figure 7-10 Mold fabrication by a HIFU transducer. (a) designed model (b) Fabricated acrylic molds at a duty cycle of 60 % and with various feed rates; the second model from the left was chosen for mold fabrication.

The cross-section of a channel fabricated by this method is presented in Figure 7.11. As shown in Figure 7.11 (b), the width of the channels is considerably large compared to their height. This is due to the beam diameter which is approximately 0.8 mm.

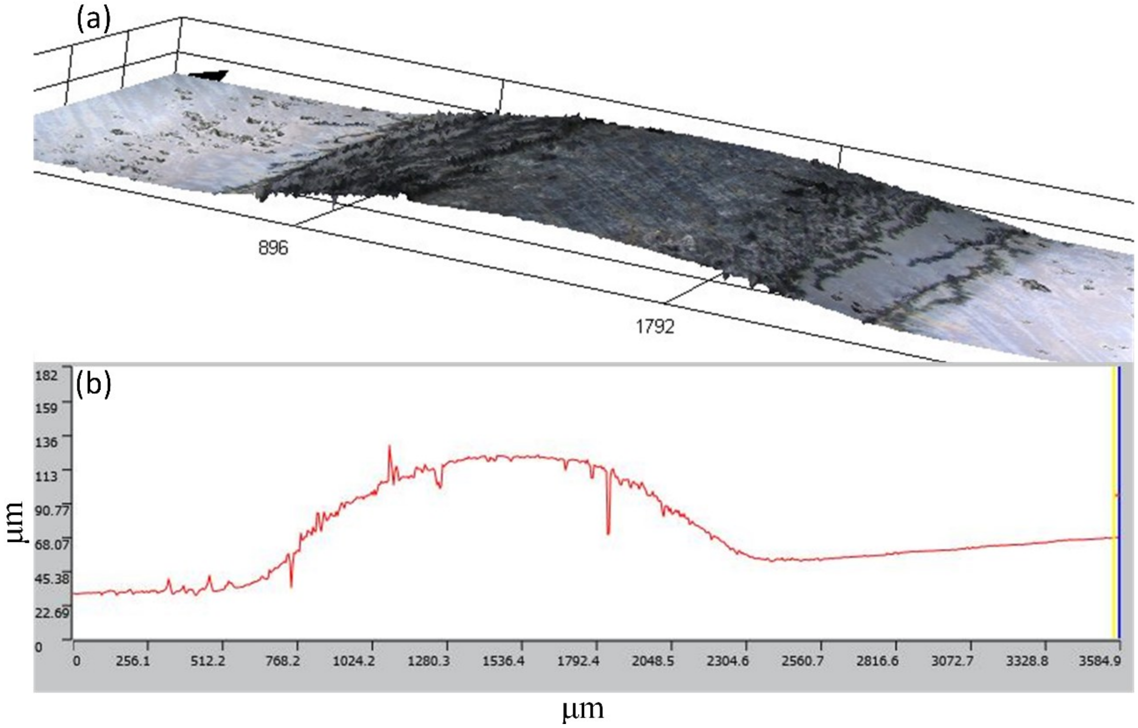

Figure 7-11 Surface topography of the sample fabricated at DC of 60 % and feed rate of 150 mm/min obtained by confocal microscopy.

The fabricated mold with a duty cycle of 60 % and a feed rate of 80 mm/min was used as a master mold for the Y channel. The surface of the acrylic part was washed with IPA and PDMS at a mixing ratio of 10:1 was poured onto the mold and cured at 40 °C within 12 hours. Then, the cured PDMS Y-channel was peeled off from the acrylic sheet. The PDMS chip was bonded to a glass substrate with oxygen plasma treating. The PDMS chip and the fabricated chip are illustrated in Figure 7.12.

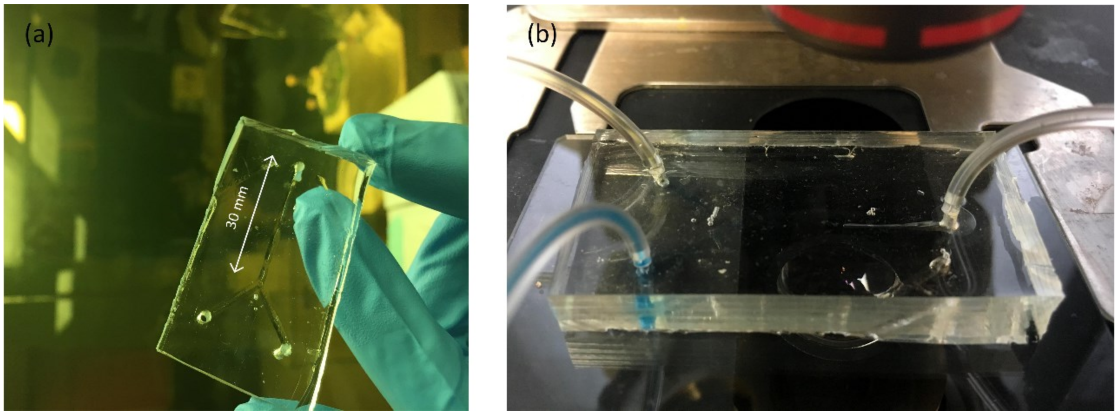

Figure 7-12 fabrication of a microfluidic device by an acrylic mold. (a) the PDMS chip; holes were punched to connect tubes; (b) the fabricated chip was tested with dyed water.

Overall, these results indicate that this method can simplify fabrication of circular channels. In addition, despite most fabrication methods, the surface of the mold does not require post-treating and can be used directly as a master mold. Smaller channels can be obtained by using a transducer with a higher frequency and a smaller focal size.

7.6. Conclusions

In this chapter, two polymer-based fluidic devices were fabricated by the acoustic-assisted method which contain channels with widths of 4 mm and 1.68 mm. Time and cost required for fabricating a part by this method is considerably low and no additional post processing is required to turn the printed part to a functional part. In addition, a method for fabrication of acrylic molds by a HIFU was suggested. This method can simplify fabrication of circular channels. Furthermore, molds do not require post-processing and can directly be used as a mold.

Chapter 8

8. Conclusions and future work

8.1. Summary and conclusion

An additive manufacturing method is presented for fabrication of polymer-based microfluidic devices. An acoustic-assisted 3D printer was designed, fabricated and developed using a HIFU transducer in order to selectively solidify polymer by heat induced by focused ultrasound. This fully automated rapid process can guide microfluidics towards the development of low-cost commercially devices. In short, the key features of the different steps toward the design and fabrication of the device are listed below:

- The acoustic pressure and heat transfer in the domain were simulated to study the impacts of various parameters on the printing process. The results obtained by the simulation were in good agreement with the device data sheet. The sensitivity of the system to acoustic impedance, frequency, power and acoustic absorption were investigated, and was found that these factors had a considerable effect on the temperature rise. These models provided a valuable understanding of the phenomena prior to the experiment, especially in selecting a proper transducer and material for the resin tank.
- Fabrication of microfluidic devices with a commercial 3D printer was carried out in order to investigate the limitation of using 3D printed molds for fabrication of PDMS-based devices. Three microfluidic chips were fabricated and the roughness and accuracy of the 3D printer in each model and configuration were analyzed. This method significantly reduced the fabrication time and cost. However, the resolution of the process is limited and the molding process is fully manual.
- A postprocessor was developed for the CNC machine that was used in three ways, including referencing the CNC machine, determining the printing space and converting the G-code obtained from the design to one in the printing path to achieve the desired layer thickness. In addition, polystyrene was chosen as the

material for the resin tank due to its transparency and higher deflection temperature compared to ABS and LDPE.

- Five different thermoset materials were tested and PDMS high viscosity, low exothermic curing process and, biocompatibility made it an ideal material for the 3D printer.
- Acoustic streaming; a major phenomenon that affects the process was discussed and an experiment was designed to observe the streaming induced by the HIFU. In addition, temperature rise obtained with the simulation were compared to the experiment which showed a significant error due to the well-known "thermocouple-artifact" effect. Focal shape was identified by a thermochromic liquid crystal sheet. The focal length had a length of 7.18 mm.
- The 3D printer was fabricated and two polymer-based fluidic devices were fabricated by the acoustic-assisted method which contain channels with widths of 4 mm and 1.68 mm. PDMS was used as resin for these models. The printing spot size was 1.24 mm for printed models. Dyed water was injected into the fabricated devices and no leakage was observed.
- A method for fabrication of acrylic molds by a HIFU was proposed. This method can simplify fabrication of circular channels. In addition, molds do not require post-processing and can directly be used as a mold. The smallest channel obtained by this method had a 1.05 mm width and a 47 μm height.

8.2. Future works

The objective of this thesis is to develop an additive manufacturing method to rapidly fabricate 3D printed structures by a biocompatible material. Several steps have been performed toward printing a polymer-based fluidic device. However, there are still a number of considerations that can be implemented for the further improvement of the presented method. Such improvements are suggested below:

- Testing other biocompatible materials and investigating the effect of material properties on the printing process

- Developing a software for acoustic-assisted 3D printing method that can generate path lines according to the model, the input power and duty cycle and the layer thickness
- Conducting more experiments in order to determine the effects of various parameters on the process
- Performing image processing on images obtained by the SEM to characterize number of bubbles and their size distribution
- Using a transducer with smaller focal size and higher frequency to improve the 3D printer resolution

References

[1] N. Bhattacharjee, A. Urrios, S. Kang, and A. Folch, “The upcoming 3D-printing revolution in microfluidics,” *Lab Chip*, vol. 16, no. 10, pp. 1720–1742, 2016.

[2] T. J. Hinton, A. Hudson, K. Pusch, A. Lee, and A. W. Feinberg, “3D printing PDMS elastomer in a hydrophilic support bath via freeform reversible embedding,” *ACS Biomater. Sci. Eng.*, vol. 2, no. 10, pp. 1781–1786, 2016.

[3] S. C. Terry, J. H. Jerman, and J. B. Angell, “A gas chromatographic air analyzer fabricated on a silicon wafer,” *IEEE Trans. Electron Devices*, vol. 26, no. 12, pp. 1880–1886, 1979.

[4] D. J. Harrison, A. Manz, Z. Fan, H. Luedi, and H. M. Widmer, “Capillary electrophoresis and sample injection systems integrated on a planar glass chip,” *Anal. Chem.*, vol. 64, no. 17, pp. 1926–1932, 1992.

[5] D. C. Duffy, J. C. McDonald, O. J. A. Schueller, and G. M. Whitesides, “Rapid prototyping of microfluidic systems in poly (dimethylsiloxane),” *Anal. Chem.*, vol. 70, no. 23, pp. 4974–4984, 1998.

[6] A. Ahmadian, Y. Adam, P. William, and W. Tammy, “3D printing : an emerging tool for novel microfluidics and lab ‑ on ‑ a ‑ chip applications,” *Microfluid. Nanofluidics*, 2016.

[7] B. Ziaie, A. Baldi, M. Lei, Y. Gu, and R. A. Siegel, “Hard and soft micromachining for BioMEMS: review of techniques and examples of applications in microfluidics and drug delivery,” *Adv. Drug Deliv. Rev.*, vol. 56, no. 2, pp. 145–172, 2004.

[8] J. Fang, W. Wang, and S. Zhao, “Fabrication of 3D microfluidic structures,” in *Encyclopedia of Microfluidics and Nanofluidics*, Springer, 2015, pp. 1069–1082.

[9] G. Lin, K. S. J. Pister, and K. P. Roos, “Heart Cell Force Transducer,” *J. Microelectromechanical Syst.*, vol. 9, no. 1, pp. 9–17, 2000.

[10] P. C. Galambos *et al.*, “Surface-micromachined microfluidic devices.” Google Patents, 25-Mar-2003.

[11] M. Okandan, P. Galambos, S. S. Mani, and J. F. Jakubczak, “Development of surface micromachining technologies for microfluidics and BioMEMS,” in *Microfluidics and BioMEMS*, 2001, vol. 4560, pp. 133–140.

[12] I. Saxena, K. Ehmann, and J. Cao, “Laser-induced plasma in aqueous media: numerical simulation and experimental validation of spatial and temporal profiles,” *Appl. Opt.*, vol. 53, no. 35, pp. 8283–8294, 2014.

[13] Albert Folch i Folch, *Introduction to BioMEMS*. CRC Press, 2012.

[14] Y. Saotome and H. Iwazaki, “Superplastic backward microextrusion of microparts for micro-electro-mechanical systems,” *J. Mater. Process. Technol.*, vol. 119, no. 1–3, pp. 307–311, 2001.

[15] A. Bertsch, H. Lorenz, and P. Renaud, “Combining microstereolithography and thick resist UV lithography for 3D microfabrication,” in *Micro Electro Mechanical Systems, 1998. MEMS 98. Proceedings., The Eleventh Annual International Workshop on*, 1998, pp. 18–23.

[16] C. Beuret, G.-A. Racine, J. Gobet, R. Luthier, and N. F. De Rooij, “Microfabrication of 3D multidirectional inclined structures by UV lithography and electroplating,” in *Micro Electro*

Mechanical Systems, 1994, MEMS'94, Proceedings, IEEE Workshop on, 1994, pp. 81–85.

[17] D. J. Guckenberger, T. E. de Groot, A. M. D. Wan, D. J. Beebe, and E. W. K. Young, "Micromilling: a method for ultra-rapid prototyping of plastic microfluidic devices," *Lab Chip*, vol. 15, no. 11, pp. 2364–2378, 2015.

[18] M. M. D. T. V. Dani and A. M. W. M. N. Syed, "Application of CAD/CAE & Rapid Prototyping Technology in Medical Field," vol. 4, no. May, pp. 1674–1678, 2013.

[19] T. Wohlers and T. Gornet, "History of additive manufacturing Introduction of non-SL systems Introduction of low-cost 3D printers," *Wohlers Rep. 2012*, pp. 1–23, 2012.

[20] D. Thomas and S. Gilbert, "Costs and Cost Effectiveness of Additive Manufacturing - A Literature Review and Discussion," *NIST Spec. Publ.*, vol. 1176, pp. 1–77, 2014.

[21] B. Redwood, "The Advantages of 3D Printing." [Online]. Available: https://www.3dhubs.com/knowledge-base/advantages-3d-printing.

[22] M. K. Hod Lipson, *Fabricated The New World of 3D Printing*, no. 1. John Wiley & Sons, 2013.

[23] S. H. Huang, P. Liu, A. Mokasdar, and L. Hou, "Additive manufacturing and its societal impact: a literature review," *Int. J. Adv. Manuf. Technol.*, vol. 67, no. 5–8, pp. 1191–1203, 2013.

[24] C. M. B. Ho, S. H. Ng, K. H. H. Li, and Y.-J. Yoon, "3D printed microfluidics for biological applications," *Lab Chip*, vol. 15, no. 18, pp. 3627–3637, 2015.

[25] R. Amin *et al.*, "3D-printed microfluidic devices," *Biofabrication*, vol. 8, no. 2, p. 22001, 2016.

[26] S. Waheed *et al.*, "3D printed microfluidic devices: enablers and barriers," *Lab Chip*, vol. 16, no. 11, pp. 1993–2013, 2016.

[27] A. K. Au, W. Huynh, L. F. Horowitz, and A. Folch, "3D- printed microfluidics," *Angew. Chemie Int. Ed.*, vol. 55, no. 12, pp. 3862–3881, 2016.

[28] C. Chen, B. T. Mehl, A. S. Munshi, A. D. Townsend, D. M. Spence, and R. S. Martin, "3D-printed microfluidic devices: fabrication, advantages and limitations—a mini review," *Anal. Methods*, vol. 8, no. 31, pp. 6005–6012, 2016.

[29] K. G. Lee *et al.*, "3D printed modules for integrated microfluidic devices," *Rsc Adv.*, vol. 4, no. 62, pp. 32876–32880, 2014.

[30] C. Chen, Y. Wang, S. Y. Lockwood, and D. M. Spence, "3D-printed fluidic devices enable quantitative evaluation of blood components in modified storage solutions for use in transfusion medicine," *Analyst*, vol. 139, no. 13, pp. 3219–3226, 2014.

[31] Y. Ma, J. Dong, S. Bhattacharjee, S. Wijeratne, M. L. Bruening, and G. L. Baker, "Increased protein sorption in poly (acrylic acid)-containing films through incorporation of comb-like polymers and film adsorption at low pH and high ionic strength," *Langmuir*, vol. 29, no. 9, pp. 2946–2954, 2013.

[32] B. C. Gross, K. B. Anderson, J. E. Meisel, M. I. McNitt, and D. M. Spence, "Polymer coatings in 3D-printed fluidic device channels for improved cellular adherence prior to electrical lysis," *Anal. Chem.*, vol. 87, no. 12, pp. 6335–6341, 2015.

[33] N. S. Allen, "Photoinitiators for UV and visible curing of coatings: Mechanisms and properties," *J. Photochem. Photobiol. A Chem.*, vol. 100, no. 1–3, pp. 101–107, 1996.

[34] F. Hua *et al.*, “Polymer imprint lithography with molecular-scale resolution,” *Nano Lett.*, vol. 4, no. 12, pp. 2467–2471, 2004.

[35] S. G. Charati and S. A. Stern, “Diffusion of gases in silicone polymers: molecular dynamics simulations,” *Macromolecules*, vol. 31, no. 16, pp. 5529–5535, 1998.

[36] M. Bélanger and Y. Marois, “Hemocompatibility, biocompatibility, inflammatory and in vivo studies of primary reference materials low- density polyethylene and polydimethylsiloxane: A review,” *J. Biomed. Mater. Res. Part A*, vol. 58, no. 5, pp. 467–477, 2001.

[37] D. Fuard, T. Tzvetkova-Chevolleau, S. Decossas, P. Tracqui, and P. Schiavone, “Optimization of poly-di-methyl-siloxane (PDMS) substrates for studying cellular adhesion and motility,” *Microelectron. Eng.*, vol. 85, no. 5–6, pp. 1289–1293, 2008.

[38] B. D. Ratner, A. S. Hoffman, F. J. Schoen, and J. E. Lemons, *Biomaterials science: an introduction to materials in medicine*. Elsevier, 2004.

[39] Y. Sun, Q. Jallerat, J. M. Szymanski, and A. W. Feinberg, “Conformal nanopatterning of extracellular matrix proteins onto topographically complex surfaces,” *Nat. Methods*, vol. 12, no. 2, p. 134, 2015.

[40] R. N. Palchesko, L. Zhang, Y. Sun, and A. W. Feinberg, “Development of polydimethylsiloxane substrates with tunable elastic modulus to study cell mechanobiology in muscle and nerve,” *PLoS One*, vol. 7, no. 12, p. e51499, 2012.

[41] G. Comina, A. Suska, and D. Filippini, “PDMS lab-on-a-chip fabrication using 3D printed templates,” *Lab Chip*, vol. 14, no. 2, pp. 424–430, 2014.

[42] T. J. Hinton, A. Hudson, K. Pusch, A. Lee, and A. W. Feinberg, “3D Printing PDMS Elastomer in a Hydrophilic Support Bath via Freeform Reversible Embedding,” *ACS Biomater. Sci. Eng.*, vol. 2, no. 10, pp. 1781–1786, 2016.

[43] T. Femmer, A. J. C. Kuehne, and M. Wessling, “Print your own membrane: direct rapid prototyping of polydimethylsiloxane,” *Lab Chip*, vol. 14, no. 15, pp. 2610–2613, 2014.

[44] V. Ozbolat, M. Dey, B. Ayan, A. Povilianskas, M. C. Demirel, and I. T. Ozbolat, “3D Printing of PDMS Improves Its Mechanical and Cell Adhesion Properties,” *ACS Biomater. Sci. Eng.*, vol. 4, no. 2, pp. 682–693, 2018.

[45] N. Bhattacharjee, C. Parra-Cabrera, Y. T. Kim, A. P. Kuo, and A. Folch, “Desktop-Stereolithography 3D-Printing of a Poly(dimethylsiloxane)-Based Material with Sylgard-184 Properties,” *Adv. Mater.*, vol. 30, no. 22, pp. 1–7, 2018.

[46] B. Mulloy, “‘Ultrasound Physics and Technology, How, Why and When?,’” *Radiography*, 2010.

[47] J. P. Lawrence, “Physics and instrumentation of ultrasound,” *Critical Care Medicine*. 2007.

[48] J. Woo, “A short history of the development of ultrasound in obstetrics and gynecology,” pp. 1–19, 2008.

[49] C. H. Sherman and J. L. Butler, *Transducers and arrays for underwater sound*. 2007.

[50] N. M. Tole, “Basic Physics of Ultrasonographic Imaging,” pp. 1–5, 2005.

[51] W. J. Fry and F. Dunn, “Ultrasonic irradiation of the central nervous system at high sound levels,” *J. Acoust. Soc. Am.*, vol. 28, no. 1, pp. 129–131, 1956.

[52] M. R. Bailey, V. A. Khokhlova, O. A. Sapozhnikov, S. G. Kargl, and L. A. Crum, “Physical mechanisms of the therapeutic effect of ultrasound (a review),” *Acoust. Phys.*, 2003.

[53] F. A. Jolesz, “MRI-Guided Focused Ultrasound Surgery,” *Annu. Rev. Med.*, 2009.

[54] ASTM International, *F2792-12a - Standard Terminology for Additive Manufacturing Technologies*. 2013.

[55] F. R.Ishengoma and A. B. Mtaho, “3D Printing: Developing Countries Perspectives,” *Int. J. Comput. Appl.*, vol. 104, no. 11, pp. 30–34, 2014.

[56] K. V. Wong and A. Hernandez, “A Review of Additive Manufacturing,” *ISRN Mech. Eng.*, 2012.

[57] C. W. Hull, “Apparatus for production of three-dimensional objects by stereolithography,” *US Pat. 4,575,330*, 1986.

[58] F. P. W. Melchels, J. Feijen, and D. W. Grijpma, “A review on stereolithography and its applications in biomedical engineering,” *Biomaterials*, vol. 31, no. 24, pp. 6121–6130, 2010.

[59] S. M. Hampson, W. Rowe, S. D. R. Christie, and M. Platt, “3D printed microfluidic device with integrated optical sensing for particle analysis,” *Sensors Actuators, B Chem.*, vol. 256, pp. 1030–1037, 2018.

[60] L. J. Y. Ong, A. Islam, R. Dasgupta, N. G. Iyer, H. L. Leo, and Y. C. Toh, “A 3D printed microfluidic perfusion device for multicellular spheroid cultures,” *Biofabrication*, vol. 9, no. 4, 2017.

[61] S. Waheed *et al.*, “3D printed microfluidic devices: Enablers and barriers,” *Lab on a Chip*. 2016.

[62] S. S. Crump, “Apparatus and Method for Creating Three-Dimensional Objects,” *US Pat. 5,121,329*, 1992.

[63] B. C. Gross, J. L. Erkal, S. Y. Lockwood, C. Chen, and D. M. Spence, “Evaluation of 3D printing and its potential impact on biotechnology and the chemical sciences,” *Anal. Chem.*, 2014.

[64] M. K. Gelber and R. Bhargava, “Monolithic multilayer microfluidics via sacrificial molding of 3D-printed isomalt,” *Lab Chip*, 2015.

[65] M. D. Symes *et al.*, “Integrated 3D-printed reactionware for chemical synthesis and analysis,” *Nat. Chem.*, 2012.

[66] H. Gothait, “Apparatus and method for three dimensional model printing,” 2001.

[67] A. Causier, G. Carret, C. Boutin, T. Berthelot, and P. Berthault, “3D-printed system optimizing dissolution of hyperpolarized gaseous species for micro-sized NMR,” *Lab Chip*, 2015.

[68] J. L. Erkal *et al.*, “3D printed microfluidic devices with integrated versatile and reusable electrodes,” *Lab a Chip - Miniaturisation Chem. Biol.*, 2014.

[69] H. Yang *et al.*, “Performance evaluation of ProJet multi-material jetting 3D printer,” *Virtual Phys. Prototyp.*, 2017.

[70] P. Calvert, “Inkjet printing for materials and devices,” *Chemistry of Materials*. 2001.

[71] Y. Bai and C. B. Williams, “An exploration of binder jetting of copper,” *Rapid Prototyp. J.*, 2015.

[72] E. M. Sachs, S. Haggerty, J. Michael, and P. A. Williams, “Three-Dimensional Printing Techniques,” 1993.

[73] C. Y. Yap *et al.*, "Review of selective laser melting: Materials and applications," *Applied Physics Reviews*. 2015.

[74] C. R. . Deckard, J. J. . Beaman, and J. F. Darrah, "Method and Apparatus for Producing Parts by Selective Sintering," *U.S. Pat. 4,863,538*, 1992.

[75] C. I. Rogers, K. Qaderi, A. T. Woolley, and G. P. Nordin, "3D printed microfluidic devices with integrated valves," *Biomicrofluidics*, 2015.

[76] H. N. Chan, Y. Chen, Y. Shu, Y. Chen, Q. Tian, and H. Wu, "Direct, one-step molding of 3D-printed structures for convenient fabrication of truly 3D PDMS microfluidic chips," *Microfluid. Nanofluidics*, 2015.

[77] W. Lee *et al.*, "3D-Printed micro fluidic device for the detection of pathogenic bacteria using size-based separation in helical channel with trapezoid cross-section," *Sci. Rep.*, 2015.

[78] A. Bonyár, H. Sántha, M. Varga, B. Ring, A. Vitéz, and G. Harsányi, "Characterization of rapid PDMS casting technique utilizing molding forms fabricated by 3D rapid prototyping technology (RPT)," *Int. J. Mater. Form.*, vol. 7, no. 2, pp. 189–196, 2014.

[79] Y. Hwang, O. H. Paydar, and R. N. Candler, "3D printed molds for non-planar PDMS microfluidic channels," *Sensors Actuators, A Phys.*, vol. 226, pp. 137–142, 2015.

[80] K. Kamei, Y. Mashimo, and Y. Chen, "3D printing of soft lithography mold for rapid production of polydimethylsiloxane-based microfluidic devices for cell stimulation with concentration gradients," 2015.

[81] A. O. Olanrewaju, A. Robillard, M. Dagher, and D. Juncker, "Autonomous microfluidic capillaric circuits replicated from 3D-printed molds," *Lab Chip*, vol. 16, no. 19, pp. 3804–3814, 2016.

[82] K. Kang, S. Oh, H. Yi, S. Han, and Y. Hwang, "Fabrication of truly 3D microfluidic channel using 3D-printed soluble mold," *Biomicrofluidics*, vol. 12, no. 1, p. 014105, 2018.

[83] M. Villegas, Z. Cetinic, A. Shakeri, and T. F. Didar, "Fabricating smooth PDMS microfluidic channels from low-resolution 3D printed molds using an omniphobic lubricant-infused coating," *Anal. Chim. Acta*, vol. 1000, pp. 248–255, 2018.

[84] M. J. Beauchamp, G. P. Nordin, and A. T. Woolley, "Moving from millifluidic to truly microfluidic sub-100-μm cross-section 3D printed devices," *Anal. Bioanal. Chem.*, vol. 409, no. 18, pp. 4311–4319, 2017.

[85] N. P. Macdonald, J. M. Cabot, P. Smejkal, R. M. Guijt, B. Paull, and M. C. Breadmore, "Comparing Microfluidic Performance of Three-Dimensional (3D) Printing Platforms," *Anal. Chem.*, vol. 89, no. 7, pp. 3858–3866, 2017.

[86] H. Gong, B. P. Bickham, A. T. Woolley, and G. P. Nordin, "Custom 3D printer and resin for 18 μm × 20 μm microfluidic flow channels," *Lab Chip*, vol. 17, no. 17, pp. 2899–2909, 2017.

[87] H. Gong, A. T. Woolley, and G. P. Nordin, "3D printed high density, reversible, chip-to-chip microfluidic interconnects," *Lab Chip*, vol. 18, no. 4, pp. 639–647, 2018.

[88] COMSOL, "Focused Ultrasound Induced Heating in Tissue Phantom," *COMSOL Multiphysics 5.2 Guid.*, pp. 1–38.

[89] N. IOlympus, "Ultrasonic transducers technical notes," *Tech. Broch. Olympus NDT, Waltham, MA*, pp. 39–49, 2006.

[90] L. Schmerr and J.-S. Song, *Ultrasonic nondestructive evaluation systems*. Springer, 2007.

[91] L. W. Schmerr, “An ultrasonic system,” in *Fundamentals of Ultrasonic Nondestructive Evaluation*, Springer, 2016, pp. 1–13.

[92] R. S. C. Cobbold, *Foundations of biomedical ultrasound*. Oxford University Press, 2006.

[93] Gail ter Haar and C. Coussios, “High intensity focused ultrasound: physical principles and devices,” *Int. J. Hyperth.*, vol. 23, no. 2, pp. 89–104, 2007.

[94] A. R. Selfridge, “Approximate Material Properties in Isotropic Materials,” *IEEE Trans. Sonics Ultrason.*, vol. 32, no. 3, pp. 381–394, 1985.

[95] J. Krautkrämer and H. Krautkrämer, *Ultrasonic testing of materials*. Springer Science & Business Media, 2013.

[96] R. E. Francois and G. R. Garrison, “Sound absorption based on ocean measurements: Part I: Pure water and magnesium sulfate contributions,” *J. Acoust. Soc. Am.*, vol. 72, no. 3, pp. 896–907, 1982.

[97] M. A. Ainslie and J. G. McColm, “A simplified formula for viscous and chemical absorption in sea water,” *J. Acoust. Soc. Am.*, vol. 103, no. 3, pp. 1671–1672, 1998.

[98] F. Lionetto and A. Maffezzoli, “Monitoring the cure state of thermosetting resins by ultrasound,” *Materials (Basel).*, vol. 6, no. 9, pp. 3783–3804, 2013.

[99] U. C. Of, I. N. V. Properties, O. F. Epoxy, and D. Cure, “Ultrasonic Characterization of Changes I N Viscoelastic Properties of Epoxy During Cure,” pp. 866–869, 1983.

[100] A. Cafarelli, A. Verbeni, A. Poliziani, P. Dario, A. Menciassi, and L. Ricotti, “Tuning acoustic and mechanical properties of materials for ultrasound phantoms and smart substrates for cell cultures,” *Acta Biomater.*, vol. 49, pp. 368–378, 2017.

[101] H. J. Sutherland, “Acoustical determination of the shear relaxation functions for polymethyl methacrylate and Epon 828-Z,” *J. Appl. Phys.*, vol. 49, no. 7, pp. 3941–3945, 1978.

[102] B. C. Gross, J. L. Erkal, S. Y. Lockwood, C. Chen, and D. M. Spence, “Evaluation of 3D printing and its potential impact on biotechnology and the chemical sciences,” *Anal. Chem.*, vol. 86, no. 7, pp. 3240–3253, 2014.

[103] H. N. Chan, Y. Chen, Y. Shu, Y. Chen, Q. Tian, and H. Wu, “Direct, one-step molding of 3D-printed structures for convenient fabrication of truly 3D PDMS microfluidic chips,” *Microfluid. Nanofluidics*, vol. 19, no. 1, pp. 9–18, 2015.

[104] D. Vasiljevic, J. Parojcic, M. Primorac, and G. Vuleta, “An investigation into the characteristics and drug release properties of multiple W/O/W emulsion systems containing low concentration of lipophilic polymeric emulsifier,” *Int. J. Pharm.*, vol. 309, no. 1–2, pp. 171–177, 2006.

[105] D. Sivakumaran, E. Mueller, and T. Hoare, “Microfluidic production of degradable thermoresponsive poly (N-isopropylacrylamide)-based microgels,” *Soft Matter*, vol. 13, no. 47, pp. 9060–9070, 2017.

[106] P. M. Valencia *et al.*, “Single-step assembly of homogenous lipid− polymeric and lipid− quantum dot nanoparticles enabled by microfluidic rapid mixing,” *ACS Nano*, vol. 4, no. 3, pp. 1671–1679, 2010.

[107] Q. Xu *et al.*, “Preparation of monodisperse biodegradable polymer microparticles using a

microfluidic flow-focusing device for controlled drug delivery," *Small*, vol. 5, no. 13, pp. 1575–1581, 2009.

[108] N.-N. Deng *et al.*, "Simple and cheap microfluidic devices for the preparation of monodisperse emulsions," *Lab Chip*, vol. 11, no. 23, pp. 3963–3969, 2011.

[109] E. Q. Li, J. M. Zhang, and S. T. Thoroddsen, "Simple and inexpensive microfluidic devices for the generation of monodisperse multiple emulsions," *J. Micromechanics Microengineering*, vol. 24, no. 1, p. 15019, 2013.

[110] J. Li and D. A. Barrow, "A new droplet-forming fluidic junction for the generation of highly compartmentalised capsules," *Lab Chip*, vol. 17, no. 16, pp. 2873–2881, 2017.

[111] M. Marzban, M. Packirisamy, and J. Dargahi, "3D Suspended Polymeric Microfluidics (SPMF3) with Flow Orthogonal to Bending (FOB) for Fluid Analysis through Kinematic Viscosity," *Appl. Sci.*, vol. 7, no. 10, p. 1048, 2017.

[112] H. Gong, B. P. Bickham, A. T. Woolley, and G. P. Nordin, "Custom 3D printer and resin for 18 μm × 20 μm microfluidic flow channels," *Lab Chip*, vol. 17, no. 17, pp. 2899–2909, 2017.

[113] Stepcraft, "Original Operating Instructions," 2012. [Online]. Available: https://www.stepcraft-systems.com/images/SC-Service/Anleitungen-EN/EN-Operating-Instructions-SC2-v4.pdf.

[114] National instruments, "NI cDAQ ^{TM} -9171 Datasheet." [Online]. Available: http://www.ni.com/pdf/manuals/374037b.pdf.

[115] National instruments, "NI 9212 Datasheet." [Online]. Available: http://www.ni.com/pdf/manuals/374358b_02.pdf.

[116] "HDT @0.46 Mpa (67 psi) Values of Several Plastics." [Online]. Available: https://omnexus.specialchem.com/polymer-properties/properties/hdt-0-46-mpa-67-psi.

[117] T. Scientific, "Thermo Scientific BioLite Cell Culture Product Datasheets," *Culture*. [Online]. Available: http://www.tslabor.hu/depo/NUNC_Plastic/2014-BioLite Cell Culture products.pdf.

[118] H. Dodiuk and S. H. Goodman, *Handbook of Thermoset Plastics, Second Edition*. 2000.

[119] A. J. Franck, "Understanding Rheology of Thermosets," *TA Instruments*, vol. AAN015, p. 14, 2004.

[120] G. T. Carroll, N. J. Turro, and J. T. Koberstein, "Patterning dewetting in thin polymer films by spatially directed photocrosslinking," *J. Colloid Interface Sci.*, vol. 351, no. 2, pp. 556–560, 2010.

[121] L. H. Sperling, *Introduction to physical polymer science*. John Wiley & Sons, 2005.

[122] P. O. Nielsen, *PROPERTIES OF EPOXY-RESINS, HARDENERS, AND MODIFIERS*, vol. 25, no. 4. INTERTEC PUBL CORP 6151 POWERS FERRY RD, NW, ATLANTA, GA 30339, 1982.

[123] W. Noll, *Chemistry and technology of silicones*. Elsevier, 2012.

[124] Materia, "Proxima® HPR 2029." [Online]. Available: https://www.tri-iso.com/documents/Materia_Proxima_HPR_2029_TDS.pdf.

[125] C. Eckart, "Vortices and streams caused by sound waves," *Phys. Rev.*, vol. 73, no. 1, p. 68, 1948.

[126] G. Madelin, D. Grucker, J.-M. Franconi, and E. Thiaudiere, "Magnetic resonance imaging of acoustic streaming: Absorption coefficient and acoustic field shape estimation," *Ultrasonics*, vol. 44, no. 3, pp. 272–278, 2006.

[127] A. Nowicki, T. Kowalewski, W. Secomski, and J. Wójcik, “Estimation of acoustical streaming: theoretical model, Doppler measurements and optical visualisation,” *Eur. J. Ultrasound*, vol. 7, no. 1, pp. 73–81, 1998.

[128] R. Ben Haj Slama, B. Gilles, M. Ben Chiekh, and J. C. Béra, “PIV for the characterization of focused field induced acoustic streaming: seeding particle choice evaluation,” *Ultrasonics*, vol. 76, pp. 217–226, 2017.

[129] M. Nabavi, M. H. Kamran Siddiqui, and J. Dargahi, “Simultaneous measurement of acoustic and streaming velocities using synchronized PIV technique,” *Meas. Sci. Technol.*, vol. 18, no. 7, pp. 1811–1817, 2007.

[130] P. Hariharan, M. R. Myers, R. A. Robinson, S. H. Maruvada, J. Sliwa, and R. K. Banerjee, “Characterization of high intensity focused ultrasound transducers using acoustic streaming,” *J. Acoust. Soc. Am.*, vol. 123, no. 3, pp. 1706–1719, 2008.

[131] M. J. Choi *et al.*, “Acoustic streaming in lithotripsy fields: preliminary observation using a particle image velocimetry method,” *Ultrasonics*, vol. 44, no. 2, pp. 133–145, 2006.

[132] W. J. Fry and R. B. Fry, “Determination of absolute sound levels and acoustic absorption coefficients by thermocouple probes—Theory,” *J. Acoust. Soc. Am.*, vol. 26, no. 3, pp. 294–310, 1954.

[133] W. J. Fry and R. B. Fry, “Determination of absolute sound levels and acoustic absorption coefficients by thermocouple probes—experiment,” *J. Acoust. Soc. Am.*, vol. 26, no. 3, pp. 311–317, 1954.

[134] K. Hynynen and D. K. Edwards, “Temperature measurements during ultrasound hyperthermia,” *Med. Phys.*, vol. 16, no. 4, pp. 618–626, 1989.

[135] J. Huang, R. G. Holt, R. O. Cleveland, and R. A. Roy, “Experimental validation of a tractable numerical model for focused ultrasound heating in flow-through tissue phantoms,” *J. Acoust. Soc. Am.*, vol. 116, no. 4, pp. 2451–2458, 2004.

[136] R. K. Banerjee and S. Dasgupta, “Characterization methods of high-intensity focused ultrasound-induced thermal field,” in *Advances in Heat Transfer*, vol. 42, Elsevier, 2010, pp. 137–177.

[137] H. Morris, I. Rivens, A. Shaw, and G. ter Haar, “Investigation of the viscous heating artefact arising from the use of thermocouples in a focused ultrasound field,” *Phys. Med. Biol.*, vol. 53, no. 17, p. 4759, 2008.

[138] D. M. Nell and M. R. Myers, “Thermal effects generated by high-intensity focused ultrasound beams at normal incidence to a bone surface,” *J. Acoust. Soc. Am.*, vol. 127, no. 1, pp. 549–559, 2010.